DEPARTMENT OF URBAN INNOVATION
SPECIALIZATION IN COASTAL ENGINEERING
YOKOHAMA NATIONAL UNIVERSITY

Interaction of Cross-Shore Sediment Mixing and Sediment Properties for Beach Topography Change in the Nearshore Region

By

Thamali Menaka Gunaratna

A dissertation submitted in partial fulfillment of the requirements for the degree of
Doctor of Philosophy in Engineering

Academic Advisor: Assoc. Prof. Takayuki SUZUKI
September, 2018

ABSTRACT

As the waves approach the coastline, the waves undergo several hydrodynamic challenges ranging from shoaling, diffraction, refraction, wave breaking and etc. Due to the influence made with hydrodynamic changes and reducing of water level heights, the sea bed experience the wave and current forces which initiate the movement of bed sediments. Sediment transport studies have been recently advancing with the vast amount of research studies that are being done by many researchers worldwide. The understanding of mechanisms of sediment transport and the relationships to bed morphology is however still not grasped well in order to estimate the accurate amount of quantities of net sediment movement and topography difference with time and space. There are several stages of sediment transport starting from sediment mixing, bed load movement, suspended transport and beach erosion/accumulation which occur between time/depth scales. The initiation of sediment bed load movement has a great impact on changing the bed topography that leads to formation of sand bars, beach slopes, sand ripples and etc. eventually causing accretive or erosive bed profiles with time. Sediment mixing is an initiation of bed load movement which occurs underneath the mobile bed layer by the vertical movement of sediment layers due to wave and current conditions.

Several experimental researches have been conducted in different parts of the world with different wave climates and beach types to estimate probable relationships to the initiation of bed load movement with respect to sediment mixing depths. The researches have figured out that the wave breaking height has a significant linear correlation with respect to the mixing vertical depth in the surf zone. The ratio between the mixing depth and significant wave breaking height varied between authors ranging from 0.027 to 0.35 depending on experiment environment. Some authors suggested a linear correlation of mixing depths with wave breaking height and bed slope together. The authors suggested many other parameters should be directly correlated such as grain size, surf similarity parameter, surf scaling parameter and etc. Sediment properties are another possible influence in governing the mixing and movement of bed profile. However the cross-shore sediment properties have a significant variation from one location to another based on the change of wave hydrodynamics from offshore to onshore direction. Thus the understanding of sediment properties for bed sediment mixing and movement is another area to be expertise. This research is mainly focusing on these research aspects of sediment mixing and sediment properties in the cross-shore.

Based on the history of research concerning the sediment mixing and sediment properties, two main objectives were establishes; To evaluate the temporal and spatial sediment mixing with wave hydrodynamics and to assess the sediment properties in the field for sediment mixing and bed morphology. The study has taken into a consideration of sediment mixing from the beginning of swash zone to the end of surf zone covering a wider range approach in a 2D flume test environment with two tracer study experiments conducted on a mobile and a partially mobile bed. The mixing depths were investigated using a fluorescent tracer by collecting sand core samples covering the area at different time intervals. The initial test was to investigate the sediment mixing under accretive and erosive wave conditions and the latter for the analysis of sediment mixing under different wave breaking conditions. It was observed the mixing has a dynamic pattern from the entire region starting from swash to end of surf zone where maximum intrusion location lying at the wave breaking area and shifting towards offshore or onshore depending on the wave influenced beach conditions. The sediments were also observed to mix while moving to on-offshore direction based on accretive or erosive conditions accordingly. Extensive amount of calibrations were done using XBeach model for numerical simulation of the mentioned wave hydrodynamics under accretive wave conditions, but was unable to proceed with. However the calibration parameters of facua, dryslp, wetslp were significantly affecting the model results of erosive wave conditions which has been shown in this paper. For the analysis of mixing depths under different wave breaking conditions, a similar tracer study was decided, but with several changes in flume setup. Four waves were generated with two wave breaking styles which the fluid velocities were numerically calculated using a Large Eddy Simulation model. The wave breaking induced eddies of each wave condition were calculated and compared with the mixing depth trend along the bed profile. There was a significant similarity which suggested a direct correlation of sediment mixing from the wave breaking style and bottom plane/vertical plane eddies by the experiment and numerical results. Furthermore, the past records of wave heights and mixing depths alongside with the mentioned experiment results suggested to have higher mixing depths for bed slopes of $\geq 1/10$ and the wave height does not necessarily correlate with the spatial mixing depth trend.

In addition to sediment mixing, sediment properties along the cross-shore was analyzed for temporal bed evolution. Four experiments were conducted at a dissipative beach; Hasaki, Japan in 2014, 2015 in winter and 2016, 2017 in summer periods. Sediment cores of ~1 m were collected from the swash zone to the end of surf zone for all experiment days and the sediment properties of median grain size, sorting and

skewness were calculated. It was observed that the sediment size, sorting and skewness values get larger as reached down through elevation suggesting a bed erosion limitations during high waves. Two significant characteristics of sediments were observed; Fine, well sorted and coarser, poorly sorted, both coarser in skewness. Near to the shoreline, the latter properties were observed, as well as in the deeper elevations of the profile thereafter where former properties of sand collected in the wave height transition zone. The finer, well-sorted sand was transported to the offshore according to the intensity of the waves, which resulted in the reappearance of deep-seated materials of poorly sorted sediment over time. The offshore area profile of the Surf Zone was observed with limited erosion depths due to the existence of the poorly sorted coarse materials which was later justified using weekly bed profile measurements. Sediment properties were observed to have a direct influence on the change in bed profile and thus important to be considered in sediment mixing and moving studies. The parameters of sorting coefficient and mixing depth/sediment diameter was observed to make an inversely correlated relationship ($y = 7.853x^{-4.165}$, $R^2 = 0.77$) which shows that smaller, well-sorted sediment samples having higher mixing compared to coarser, poorly sorted sand. This could be a beginning of a new research area in order to explore the sediment characteristics with sediment mixing which was not quantitatively observed in past. In addition to the experimental work, Wet and Dry Princeton Ocean model was suggested to change allowing the inclusion of bed sediment size variation along the coast. A new methodology of application of bed sediments with different particle sizes for sediment flux calculations was introduced to the sand transport module of WD-POM.

The research findings are hoped to build a strong foundation of future research work carried out by future researchers in sediment mixing and transport studies. The sediment mixing studies would help in the areas of oil spill, sediment pollution, microbiological, eco-system and beach nourishment studies while the sediment properties research work will benefit in future sediment properties and morphological studies. Further investigations are recommended on the erosional profile limitations for Hasaki coast and the areas of sediment properties and mixing.

ACKNOLEDGEMENTS

I am honored and thankful to finish my PhD studies on time, without any inconvenience with the help of number of people whom I have and have not mentioned below. It is a great pleasure to provide my knowledge gathered during the past 3 years in Japan concluded in one source for the future use of graduate students and researchers around the globe.

First of all, I want to give heartiest acknowledgements to my main supervisor/advisor, Dr. Takayuki Suzuki, whom have always been my role model and my motivator, always being available to discuss research matters faced during the PhD years. I am equally grateful to Dr. Ken-ichi Uzaki for assisting me with POM while visiting YNU numerous times in order to accomplish better research results. I would also like to acknowledge Prof. Yoshiyuki Nakamura and Dr. Hiroto Higa for their valuable comments, questions and support during the research period, especially in weekly lab seminars. I convey my gratitude to all the remaining committee members; Dr. Hiroshi Katsuchi and Dr. Kimitoshi Hayano for their time, effort, constructive criticism, comments and questions raised in order to improve this research. Further thanks go to the laboratory secretary, Miss. Akiko Nakao for helping me with the paperwork related to laboratory expenses, local/international trips and etc.

I would also like to give my appreciations to the international lab members; Mr. Joemel Sumbing, Mr. Muhammed Ali Hafeez, Dr. Edwin Muchabave, Mr. Kulachart Kullakok for making a peaceful work environment and the Japanese students, for all the cooperation. I want to give my special thanks to Miss. Saki Akimoto, Mr. Yu Inami, Mr. Sakihama, Mr. Kurosaki for their exceptional support during the experiments and Mr. Kenji Narita, Mr. Seiko Kikuyama, Miss. Asumi Kawagoe also in daily activities which made my life in Japan much more convenient.

Further acknowledgements go to Mr. Yanagishima for conducting the sieve analysis for Hasaki field experiments and Dr. Katsuchi again, for lending me the CCD camera for the PIV analysis from the YNU Structural laboratory. In addition, I would like to thank Prof. Daniel Cox from Oregon State University for the journal paper reviews and constructive comments to improve the paper furthermore. I am also grateful for the previous YNU students, Dr. Chamila Niroshinie, Dr. Mangala and Dr. Anil from Tokyo Tech Institute for their guidance and assisting me with international visa and financial issues.

Furthermore, I am grateful to my father, who passed away during my PhD studies, my loving mother and brother whom initiated my path to the PhD, gave me strength, mental support, taking care of me during the hardships faced, always being there for me with their invaluable kindness. In addition to my family members, my close friends; Miss. Samantha Walia, Miss. Ashane Sulakshi, Miss. Alicia Kato and Miss. Nofunale Amakali for their lovely companionship. Especially the Sri Lankan community members in Yokohama; Dr. Chamila Rankoth, Mrs. Dayani Sanjeewani, Mr. Eashan Nandasiri, and Mr. Dinesh Kodithuwakku are being appreciated with their kindness and support.

Last, but not least, I am beholden to the Government of Japan and Yokohama National University for providing me financial assistance through Monbukagakusho (MEXT) scholarship which made my dreams come true to achieve outstanding research work and publications during the Ph.D period. Everyone who helped me in order to receive the scholarship and paperwork are being remembered and highly appreciated. In addition to the scholarship, the experiment work carried out were funded partially by the JSPS Grant-in-aid for Young Scientists (A), No. 26709034 which I am beholden for.

I hope my research would benefit the future generations of researchers and may the blessings of their success be with my loving father who passed away on 3rd January, 2017.

TABLE OF CONTENTS

LIST OF TABLES

LIST OF FIGURES

LIST OF SYMBOLS

H_{bs}	Significant wave breaking height
Z_m	Maximum mixing depth
H_b	Wave breaking height
DoD	Depth of disturbance
SAM	Sediment activity meter
Tz	Wave period
Hs	Significant wave height
tanβ	Beach slope
ISO	International Organization for Standardization
ASTM	American Society for Testing and Materials
φ	Phi scale
D	Diameter size in mm scale
D0	Reference diameter equals to 1mm
D10	Cumulative 10% point of diameter
D25	Cumulative 25% point of diameter
D30	Cumulative 30% point of diameter
D50	Cumulative 50% point of diameter
D60	Cumulative 60% point of diameter
D75	Cumulative 75% point of diameter
D90	Cumulative 90% point of diameter
S0	Sorting coefficient
Q1	25th percentile on the cumulative sieve analysis curve
Q3	75th percentile on the cumulative sieve analysis curve
Sk	Skewness parameter
q	Sediment transport rate
Ɛb	Bed Load efficiency
Ɛs	Suspended load efficiency
ϕ	Particle friction angle
ub	Near bed free stream velocity
ω	Fall velocity
w	Work done by bed shear stress
cf	Bottom friction coefficient
GLM	Generalized lagrangian mean
E	Wave energy

σ	Intrinsic wave frequency
θ	Refraction due to bottom and currents
D	Energy dissipation due to wave breaking
E_{roller}	Roller energy
E_{waves}	Short wave energy
E	Eularian
L	Lagrangian
F_x	Short wave force
F_y	Roller wave force
υ_h	Horizontal viscosity coefficient
S_x	Sediment transport rate in x-direction
S_y	Sediment transport in y-direction
D_s	Sediment diffusion coefficient
C	Sediment concentration
T_s	Sediment concentration adaptation time scale
C_{eq}	Equilibrium sediment concentration
A_{ss} and A_{sb}	Suspended and bed load coefficients
f_{mor}	Morphological acceleration factor
p	Porosity
u_{cr}	Crtitical transport velocity
LES	Large eddy simulation
$\overline{u_i}$	Spatially averaged velocity over the grid size
τ_{ij}	Sub grid scale stress
SGS	Sub grid scale
u_i'	Velocity due to small scale turbulence
V_e	Viscosity coefficient
$\overline{D_{ij}}$	Strain rate
C_s	Smagorinsky coefficient
$\Delta x_1, \Delta x_2, \Delta x_3$	Grid spacing lengths
DTE	Enternal mode calculation time step
DTI	Internal mode calculation time step
WD-POM	Wet and dry - Princeton ocean model
∂q_x	Sediment transport rate in x-direction
∂q_y	Sediment transport rate in y-direction
∂ z	Bed elevation difference

∂ t	Time interval
∂ x	X-grid spacing
∂ y	Y-grid spacing
k	Number of sediment classes
μ_k	Volume content ratio
B_h	Sediment exchange layer thickness
q_t^k	Total net transport rates in x, y directions

1 INTRODUCTION

1.1 Background and Motivation

The world coastlines expand to thousands of kilometers reaching to top countries with the longest coastlines from Canada, Indonesia, Greenland and etc. Japan coastline stands in the 6th position of the longest coastlines having a coastline length of 29,751 km. Most of these coastline areas have become intensively utilized due to the population increase around the world. The impact of climate change on the other hand has increased its effect on most of the coastlines causing problems to the ecosystems, humanity, infrastructures and etc. The understanding of the coastal processes as the sea approaches the land thus has been vital for the scientists and researchers to overcome these issues.

The coastline experiences the waves, currents and tidal effects which causes the bed profile to vary in time and space. The waves which reach the coast will go under shoaling, diffraction, refraction and wave breaking, while the currents will shift the bed surface sediments as the tide goes up and down. The sediments on the surface and in depth of the sea surface near the coastline will be affected by the above mentioned hydrodynamic processes which causes eventually to change the shape of the coastline. Not only the sediment movements, but also weathering of sedimentary materials occurs due to the large energy dissipations, turbulences, eddies and shear stress exerted on the sediments of different sizes. The study of sediment movement and particle mixing process would thus reveal the history of energy levels of the area, bed profile evolution, sediment pollution and the effects on nearshore ecosystems.

1.2 Sediment Transport and Mixing Depth

The area of coastal sediment transport has a wide range covering two main topics of longshore and cross-shore transport which depends on a time scale of years to seconds. The longshore transport is mainly due to the long term longshore current and the littoral drift created by the lateral currents. However the cross-shore transport is a seasonal movement of sediments on and off the shore by wave and cross-shore current actions. Due to both of cross-shore and longshore sediment movements, there will be permanent and temporary/ seasonal erosive and accretive beach conditions. Beach erosion is currently observed in many parts of the world, affecting natural habitats as well as human beings (Feagin et al., 2005). This type of erosion is due to man-made structures, beach

mining (Cooper and Pethick, 2005), and severe weather conditions (Douglass, 1994). Eighty percent of the world's population lives within a radius of 1 km from the coastline (Blinovskaya, 2012). In the United States alone, it is estimated that 80–90% of the beaches may undergo erosion, which can directly affect the economy (Leatherman, 2001). Japan is another country which is prone to erosion. Losing land will directly impact the coast with severe sea conditions it has to face (Isobe, 1998). Beach accretion affects coral growth and nearshore ecosystems, thus significantly influencing the structure, biomass, and metabolism of seabed habitats (Airoldi et al., 1996). This research is based on the bed surface sediment movement and mixing in the cross-shore direction which would be evaluated by the cross-shore transportation mechanisms.

Sediment mixing is a phenomena affected by the wave and current action on the bed surface sediments during a tidal cycle or within several days (Anfuso, 2015). The layer thickness of sediments on the surf zone bed profile which is disturbed as mentioned, is given the names of mixing depth, depth of disturbance, active layer depth and etc. Number of experimental work has been conducted to discover the relationship with respect to wave height (Kraus et al., 1982, Kraus and Tanaka, 1986, Jackson and Malvares, 2002, Brook and Lemckert, 2011), bed slope (Ferreira et al., 2000, Bellido et al, 2011) and sediment size (Saini et al., 2009). The vital understanding of the bed surface sediment mixing process would escalate the knowledge on proper construction of structures, beach nourishment studies (Fucella and Dolan, 1996), eco system studies (Botton et al., 1988) and sediment pollution studies. Nearshore-sediment mixing is analyzed via the mixing depths obtained by several methods in the past. Use of rods and washers (Brian, G. and Peter, B., 1980), tracer experiments and inserting colored sand particles (Williams, 1971; Brook and Lemckert, 2011) are some of the common methods. Out of the mentioned methods, tracer experiment studies are the most commonly used approaches, where some of the tracers used were color-coated sediment particles, radionuclides, and mineral soil (Feagin et al., 2005).

1.3 Numerical Simulation of Sediment Transport

Until now, many empirical equations have been developed to quantify the sediment movement in cross-shore and longshore direction. Currently, several numerical models are being implemented to obtain precise and reasonable results using the empirical and theoretical approaches. Owing to the extensive amount of field data required for

calibration and validation purposes, using numerical models in morphological studies is quite challenging (Vousdoukas et al., 2012). Also calculating the nearshore sediment transport has become another challenge due to the complex behaviors of interactions between the currents, waves and tide which further complicated by the turbulence and undertow by wave breaking effect, topographical influence and many more (Camenen and Larroudé, 2003).

However, several formulae are being derived by the researches through an energetics (Bagnold, 1963) and probabilistic (Einstein, 1971) approaches which are being used in extending the hydrodynamic models for simulation purposes. With the community help of scientists, researchers, engineers and students the improvements of extending hydrodynamic simulation model extending could be done with well-tested and state-of-the-art algorithms. There exists number proven methodologies accounted in models such as ECOMSed, COHERENS, Delft3D, XBeach, MIKE 21 and etc. Nevertheless, there exists a need of developing sediment transport models which could be freely available that are widely tested, accepted and applicable for a wide range of applications (Warner, 2008).

1.4 Objectives of the study

The main goal of this research is to understand the mixing depth trend from the swash zone to the end of surf zone and to observe the accuracy of previously established relationships. The influence by the hydrodynamic forces, sediment properties, long term wave conditions, wave breaking will be also given attention in approaching the objectives. For these purposes, three main objectives were initiated during the research period as follows;

(1) The temporal and spatial sediment mixing on a 2D flume environment under accretive and erosive wave conditions

(2) The temporal and spatial sediment mixing trend in a 2D flume environment under different wave breaking styles

(3) The temporal and spatial sediment mixing trend according to the spatial variation of sediment properties

1.5 Research Methodology

In order to achieve the previously mentioned research scopes and objectives, the following methodologies were adopted as shown by the flow chart below;

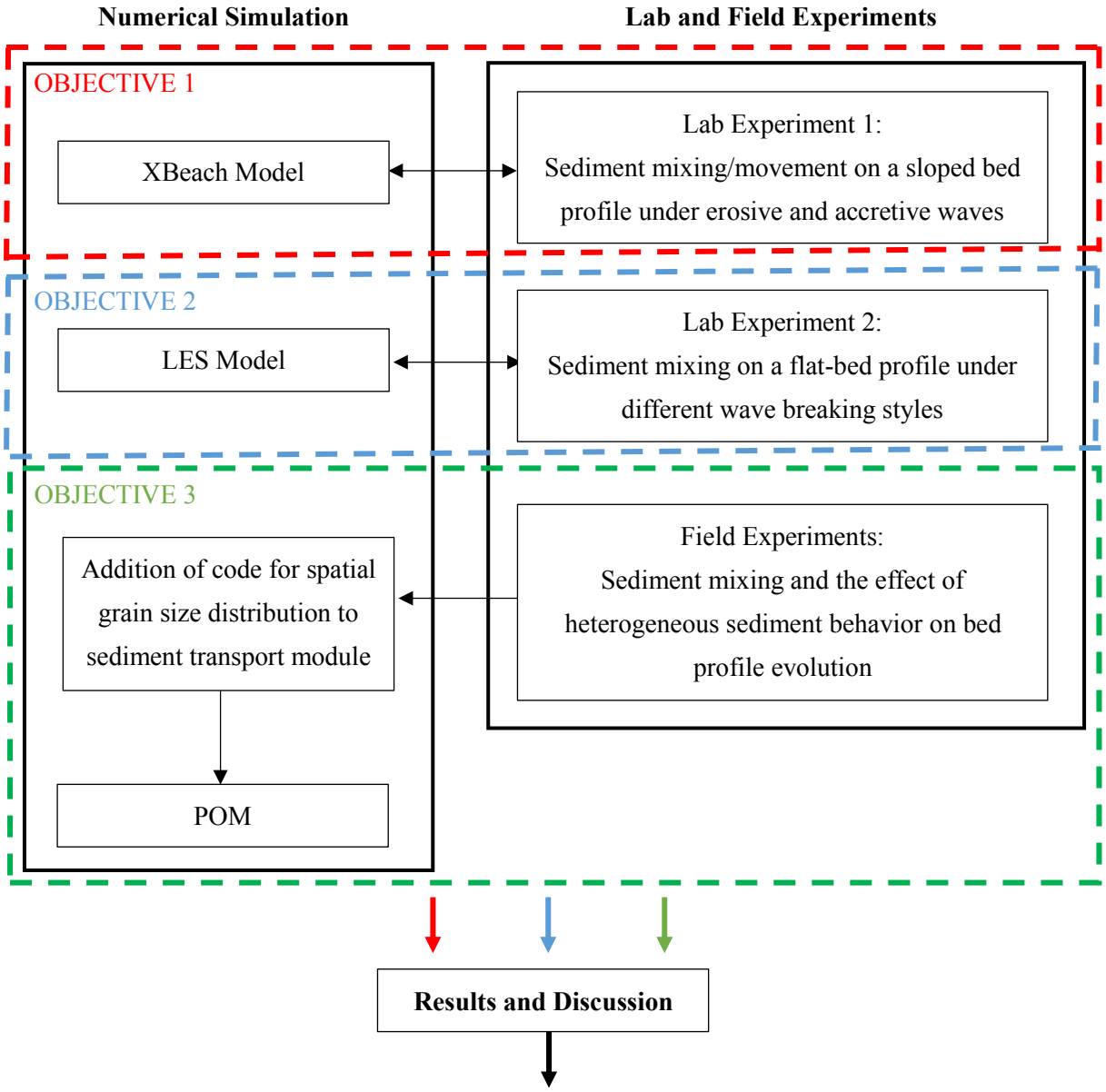

Final Outcome :

Ecosystem Studies

Sediment Pollution Studies

Beach Nourishment Studies

Sediment Transport Simulation and Experimental work

1.6 Outline of the Thesis

The thesis consist of the experimental and numerical work carried out for the objectives mentioned in previous sections. In the following chapter, the literature reviews of previous work and definitions of mixing depth and sedimentological parameters and the numerical model descriptions are given. In Chapters 3, 4 and 5, the results, discussion and conclusions of each 3 objectives mentioned above have been given. Each section includes the work of both experimental and numeral work carried out. The conclusions of all the research results and future recommendation and potential research topics are given at last along with the referenced journal, conference and other utilized resources.

2 LITERATURE REVIEW

2.1 General

Accurate characterization of wave and current interaction is able to refine the understanding the nearshore wave propagation, sediment flux and sediment transport direction. Number of research work of experimental and numerical work have been carried out in the near past to aggravate the understanding these complex processes. Due to extensive amount of wave-current interaction and the turbulence during wave breaking exerted on bed surface sediments of different grain sizes and bed arrangements creates a dynamic behaviors which has to be explored carefully by each scenario. The current study was mainly focused on surf zone sediment mixing and grain size patterns and their relations to the hydrodynamics. Thus, in this chapter, the previous literature related to the above topics of sediment mixing, grain size and bed profile arrangements and the related field/laboratory experiments and successful research results are being summarized. Apart from the experimental research work, descriptions of numerical models used in simulations of the current research work are also briefed with their governing equations and theories.

2.2 Sediment Mixing Depth

The coastal area from inland to the far offshore is divided into several zones depending on their energy levels and hydrodynamic differences. The surf zone is the area covered by where the wave begin to feel the bed bottom and starts shoaling to the wav breaking zone where the energy is dissipated creating a wave run up in the swash zone (Fig. 2.1). Many studies have been conducted regarding the sediment mixing in the wave breaking zone as for breaking waves are one of the powerful agents of sediment mixing, sediment suspension (Lin and Liu, 1998) and eventually result in bed load movement.

As mentioned above, sediment mixing in the surf zone is a result of wave breaking and also nearshore currents, wind (Airlodi et al., 1996). For better prediction of the mass balance of sediments, the estimation of the thickness of active layer which is disturbed by the mentioned scenarios is important. Moreover, comprehensive understanding of the mixing depth would benefit in further under sediment pollution, ecosystem studies, beach nourishment studies and to access the sediment movement around newly constructed coastal structures (Jackson and Malvarez, 2002).

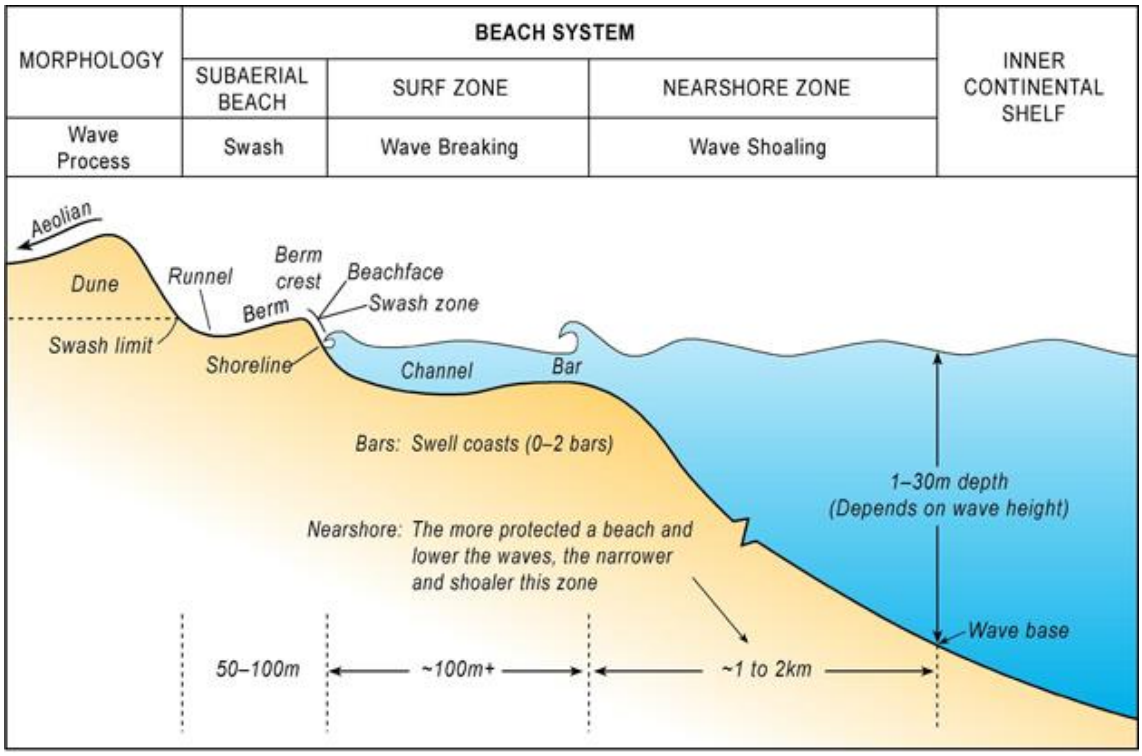

Fig. 2.1 An idealized cross-section of a beach profile defining each zones of swash, surf and nearshore (Short, 2012)

This thin layer of sediments exposed to the wave-current action is given many names of definitions as sediment mixing depth, depth of disturbance (DoD), the active layer thickness and etc. The grains of different sizes tend to mix between the immobile layer underneath and the mobile layer above due the sediment movement by wave-current action. This vertical depth of grain size movement is given the names as given before. Tracer studies using core sampling methods (eg.- Katoh and Tanaka, 1986), use of rods and washers (eg.- Greenwood and Hale, 1980) and inserting color coated particles into the bed profile (eg.- Williams, 1971) are some of the widely used approaches in acquiring the mixing depths in the surf zone. Recently Jackson and Malvares (2002) were able to introduce an instrument to measure DoD using a mechanical profiler called Sediment Activity Meter (SAM). The instrument has failed to investigate the true DoD which is only able to give the surface disturbance that could lead to wrong results. The studies were established on beaches of different morphology and hydrodynamic conditions. The tracer studies are the widely used approach among the rest, where tracers of coloured particles, radionuclides and mineral soils (Feagin et al., 2005) were used in order to track

their path.

In order to quantify the mixing depth, several approaches have been used in past according to the experiment conditions. The simplest definition would be the maximum depth of the sample which tracer has intruded. The tracers were usually placed during the low tide and collected back after one tidal cycle. There have been many modifications to this simplest definition as of the past researches;

1. The depth of where 80% of the tracer to be found (Sunamura and Krau, 1985, Ciavola et al., 1997, Katoh and Tanaka, 1986 and etc.)
2. Defining a cut-off value of particle amounts per depth interval (Kraus et al., 1982 and etc.)
3. Neglecting the depth where less than a certain number of tracer was found (Anfuso, 2005 and etc.)
4. Concentration based weighted average methods (Gaughan, 1978 and etc.)

Taking into consideration of the above mixing depth definitions, several relationships between the mixing depths and certain parameters have been established. The first relationship was made in 1985 by Kraus where he discovered a linear relationship between the significant wave breaking height (H_{bs}) to the measured mixing depths (eq. 2.1) during a tidal cycle. Since then, many wave height related relationships were made in different parts of the world covering a wide range of beach conditions.

$$Z_m = 0.027\ H_b \quad \text{.....2.1}$$

However, there is a significant difference in the relationships made by authors such as Ciavola et al.,(1997) (eq. 2.2) compared to the results of Kraus and similar authors.

$$Z_m = 0.27\ H_b \quad \text{.....2.2}$$

Both of the above equations were established by a similar experiment method, definitions, but at different beach locations and wave conditions. Thus it has been clear that there are more factors to be considered.

There have been number of field experiments regarding the mixing depth relationships to wave characteristics and beach slope in the past starting from Williams

(1971) who discovered there is a possible correlation between the beach slope and wave height to the mixing depths. Since the beginning of linear relationship discovered by Kraus (1985), many studies were established around the world in Japan (Kraus, 2985, Sunamura and Kraus, 1985), USA (Nordstrom and Jackson, 1990, Greenwood and Hale, 1980 and etc.), Mexico (Gaughan, 1978), Australia (Wright, 1981) and many more.

Table 2.1 Summary of previously obtained relationships of mixing depths

Authors	Relationship Observed	Hs (m)	Tz (sec)	Beach Slope (tanβ)
Greenwood and Hale (1980)	Zm = 0.35 Hb	2.00	6.5	
Sunamura and Kraus (1985)	Zm = 0.027 Hb	0.60 - 1.11	4.9 - 10.2	0.60 - 5.70
Katoh and Tanaka (1987)	Zm = 0.05 Hb	0.38 - 0.80	5.1 - 7.0	
Sherman et al. (1994)	Zm = 0.22 Hb	1.22		
Ciavola et al. (1997)	Zm = 0.27 Hb	0.34 - 0.80	5.1 - 7.0	5.70 - 7.90
Ferreira et al. (2000)	Zm = 0.23 Hb Zm = 1.86 Hbs tanβ	0.92	8.0	0.08
Belliod et al. (2011)	Zm = 0.029 Hbs tanβ	0.16 - 0.20	7.0 - 9.0	0.08
Brook (2011)	Zm = 0.14 Hb	0.70 - 0.80		1.34
Jackson and Malvarez (2002)	Zm = 0.24 Hb	2.00 - 3.00	8.5	
Saini et al. (2009)	Zm = 0.22 Hb	0.40		9.00

The table above shows some of the relationships observed by the previous researchers during their field experiments. The above researches were mainly conducted within a tidal cycle inside the surf zone. The most common relationship observed was the linearity between H_b and the maximum mixing depth, where some have included the effect of beach slope as well. The order of magnitude of the above equations are probably due to the different beach conditions and the tidal range.

In addition to the wave breaking heights, Anfuso (2005) observed good relationships between the mixing depth and surf scaling parameter and surf similarity index using the

previous research work data which would be useful in dissipative and reflective beach conditions. It could confirm the conclusion that the relationship between wave height and mixing depth is different for beaches with lesser slope of dissipative beaches to steeper slopes of reflective beaches from their studies. Still there are more to be discovered about the area of mixing depth and its correlation to the beach conditions which is the one of the objectives of this current study.

2.3 Sediment Diameter Variation for Bed Profile Change

A beach bed surface is a composition of fluvial waste, dead shells and different grain sizes with carbonic, minerals, heavy metals and sedimentary materials (Jiang et al., 2015). These different sized materials are shifted from one place to another by hydrodynamic forces of waves, currents, wind, etc. (Edwards, 2001). The sediment structure in the bed profile will therefore give us a story of bed morphology and sediment transport. The grain size or the sediment diameter can change from onshore to the offshore or in the direction of littoral drift depending on the beach conditions. Some studies have been carried out in different parts of the world (Edwards, 2001; De Falco et al., 2003; Buscombe, 2008; Jiang et al., 2015) to see the correlation of sediment behavior with textural parameters. The following sub topics will be discussion about the sedimentology in the coastal areas, the heterogeneous pattern of sediments and their characteristics and the importance of inclusion of the scenario in the simulation models.

2.3.1 Sediment Parameters

Sediment Diameter Size

The size of sediment could represent the distance from the original source, but it can correlate with the energy of the environment as well. In the coast, the sediments of different sizes could be found gathered from the river depositions, stormy events and currents occurrences. The grain size segregation to be more dominant in the cross-shore direction (Moutzouris, 1989) and the size distribution will occur depending on the distance from the shoreline, sediment source type and location, transport mechanism (Abuodha, 2003) and so on. Sieve analysis of sand samples, X-ray CT scanning and settling velocity methods are some of the techniques used to determine the grain size which is usually given as a diameter size in mm or phi scale (eq. 2.3). The common

method of sieve analysis gives the amount of particles which will be retaining or passing a certain mesh grid of a known grid size. These percentage measurements of diameter sizes then would be categorized according to their phi/mm scale under the Wentworth scale (Krumbein, 1937), ISO standards or ASTM standards.

$$\varphi \text{ (Krumbein Phi Scale)} = -log_2^{D/D_0} \quad \text{.....2.3}$$

where the D resembles the grain size in mm, D_0 the reference diameter equals to 1 mm. The size of coastal sand can vary from clay particles of 0.002 mm to large boulders of more than 630 mm in size. The most commonly used diameter sizes for further analysis of sedimentological parameters are D_{10}, D_{25}, D_{30}, D_{50}, D_{60}, D_{75} and D_{90} which is cumulative 10, 25, 30, 50, 60, 75 and 90 percent point of diameter in the sieve analysis curve.

Sorting and Sorting Coefficient

Sorting of a sand sample can give us information about the energy rate and duration of deposition. The layering of sediment samples can be understood by the sorting of a particular sample. In Fig. 2.2, the visual representation of sorting could be understood. In order to measure the level of sorting, the sorting coefficient (S_0) was introduced first by Trask (1932) as of eq. 2.4. If the sample is very well sorted, the finer and coarser particles are found at certain locations separated into different areas according to the energy dissipations levels while poorly sorted environments will be a mix of both finer and coarser materials together in the area due to high turbulence.

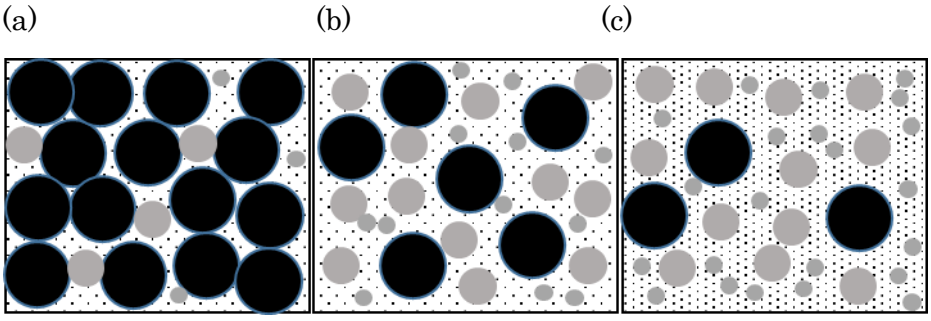

Fig. 2.2 A visual representation of (a) Well sorted, (b) Moderately sorted and (c) Poorly sorted sediment samples

Also well sorted sand has higher porosities while the less sorted will be left with poor porosities blocking the way of water to penetrate. Beach sediment movement has both vertical and horizontal sorting and segregation differences due to the seasonal effect of erosion and deposition (Kakinoki et al., 2011).

$$S_0\ (Sorting\ Coefficient\ by\ Trask, 1932) = \sqrt{Q_3/Q_1} \quad \ldots\ldots\ldots\ldots\ldots\ldots\ldots\ldots\ldots\ldots\ldots\ldots 2.4$$

Where Q_1 the 25th percentile and Q_3 the 75th percentile on the cumulative sieve analysis curve ($Q_3 > Q_1$ with mm scale and $Q_1 > Q_3$ with the phi scale). In this paper, all the values measured and calculated would be in mm scale which makes the sorting coefficient value ranges from 1.0-1.4 as well sorted, 1.4-2.0 as moderately sorted and above 2 to be poorly sorted (Trask, 1932). These limitations vary from one definition to another (Schneiderhöhn, 1953; Folk, 1954; Fuechtbauer, 1959 and etc.) depending on the equations considered. Researchers have distinguished the characteristics of each equation and limitations defined suggesting each methodology according to the environmental significance (Friedman, 1962).

Skewness and Skewness Parameter

The skewness parameter (eq. 2.5) can be used to understand the departure of the sample mean to the median diameter. This describes the symmetricity of the particle size distribution showing whether the sample has more tendency of having finer/coarser sediments accordingly.

$$S_k\ (Skewness\ by\ Trask, 1932) = \ (Q_1 \times Q_3)/{D_{50}}^2 \quad \ldots\ldots\ldots\ldots\ldots\ldots\ldots\ldots\ldots\ldots\ldots\ldots 2.5$$

Skewness parameter values coincide with unity is symmetrical, where the mode is equal to the median diameter, D_{50} which also can be recognized to have an equal amount of fine and course sediments in range. If the value is less than unity, the sample is finer skewed and higher will be coarser skewed. The finer skewed sediments samples would have a mode which is higher than its' median describing a higher amount of sediments which is less than D_{50} and otherwise in case of coarser skewed.

Other than the above mentioned definitions of skewness and sorting equations, there are several methodologies introduced to calculate. Despite to sorting and skewness, grain shape, roundness, roughness and etc. also affect the movement of a sediment (Jiang et al., 2015).

These are some of the important parameters to decide on bed profile permeability, groundwater table, filtrations, swash limits, berm formation, offshore bar formation (Buscombe and Masselink, 2006) and etc. There are number of conceptual studies conducted in order to explain the effect of sediment properties on different coastal formations.

It has been noticed that the larger particles usually gather in the high energy dissipation areas while the rest concentrate otherwise (Kakinoki et al., 2011; Jiang et al., 2015; Gallagher et al., 2016). The coarser material seem to gather on bar trough and breaker zone while the finer reaches the bar crests or carried away to the offshore (Stauble, 2005; Jiang et al., 2015). The vertical profile will be thus arranged with layers of course and fine sediments with time due to the shifting of tide level and seasonal variations. The previous researches have also noticed that the permeability levels near the swash area, which is a key factor governed by the grain size and sorting, would result in the equilibrium beachface slope. In cases of coarser poorly mixed swash areas, the infiltration levels would be high, reducing the backwash effect which would create a non-destructive beachface slope (Bagnold, 1940 and Quick, 1991).

Another study done in the Mexican sand beaches by Edwards (2011) suggests that the diminishment of grain size decrease from the offshore to onshore direction represent the reduction of wave energy in the same direction where the sorting gets less well-sorted in the inshore subzones due to the variance in wave induced currents. The author has also come up with relationships between the sorting and average grain size at each inshore, foreshore and backshore subzones of the coast. New techniques of measuring grain size and the morphological changes for each grain size and sorting condition (Kakinoki et al., 2011) are done in laboratory conditions which has to be further researched. The cross-shore variation of grain size also is sensitive for the longshore currents and transport rates as seen by Moutzouris (1989). Nonetheless the sediment characteristics of coastal zones and their effect on sediment transport rates yet to be expanded which is one of the major objectives of this research.

2.4 Numerical Assessment of Sediment Transport

Coastal sediment transport is divided into longshore and cross-shore directions which are exerted by different coastal processes. The longshore sediment transport occurred

from the longshore currents and angled waves lead to long term beach profile variations (Frihy and Komar, 1993). Effect of wave breaking and turbulence will be manifested in cross-shore transport in a time scale of several seconds to months which seasonally impact the nearshore bed profile (Dean and Dalrymple, 2004). Among all other coastal processes, sediment transport is one of the complicated natural phenomena which holds a vast research base to be improved up until now. From the past many empirical equations were invented in order to estimate the sediment movement nearshore, and today these empirical and theoretical formulae have been introduced into hydrodynamic models extending into sediment transport models to calculate the sediment transport rates and bed profile change predictions.

2.4.1 Sediment Transport Formulae and Numerical Models

Formulation of sediment transport rates run back to several years back. The calculation of these rates is quite complicated due to its complex behaviors and different mechanisms of bed load, suspended and sheet flow (Camenen and Larroudé, 2003). The main formulae are based on the energy balance or a probabilistic approach. However the foundation of these formulae was the work of du Boys (1879), Einstein (1950) and Vanoni (1975).

Bijker (1968) and Van Rijin (1984) discussed the mechanisms of both bed load and suspended load where the bed load was a method adapted on river studies and suspended load calculated by integrating the sediment concentration along water depths. An energetic approach of sediment transport was introduced in 1981 by Bailard considering the wave action which is an extended version of Bagnold (1966) formulae of transport. Dibajnia and Watanabe (1992) was able to formulate the effect of instantaneous velocity due to wave and current interaction on net sediment transport while recently, Ribberink (1998) made a bed formula which is a qausi-steady model of sediment transport which uses the instantaneous shear stress.

However in this paper, the sediment transport formulae (eq. 2.9) of Bailard (1981) model would be used for the modification purposes in WD-Princeton Ocean Model which is one of the objectives of the research. As mentioned before, Bailard model is an extended version of the Bagnold model which takes into account the gravitation effect by the bed slope. The Bagnold model is a combination of both suspended and bed load transport. The bed load is assumed to be transported by grain to grain interaction and the

suspended load due to the fluid flow through turbulence diffusion (eq. 2.6).

$$q \;=\; \left[\frac{\varepsilon_b}{tan\phi - tan\beta} + \frac{\varepsilon_s(1-\varepsilon_b)}{\left(\frac{\omega}{u_b}\right) - tan\beta}\right] w \quad \ldots\ldots\ldots\ldots\ldots\ldots\ldots\ldots\ldots\ldots 2.6$$

$$\mathrm{w} = \underset{\tau_b}{\rightarrow} . \underset{u_b}{\rightarrow} \quad \ldots\ldots\ldots\ldots\ldots\ldots\ldots\ldots\ldots\ldots\ldots\ldots 2.7$$

$$\tau_b \;=\; \rho c_f \underset{|u_b|}{\longrightarrow} \underset{u_b}{\rightarrow} \quad \ldots\ldots\ldots\ldots\ldots\ldots\ldots\ldots\ldots\ldots\ldots\ldots 2.8$$

where q gives the sediment transport rate; Ɛb and Ɛs are bed load and suspended load efficiencies; φ is the particle friction angle; ub is the nearbed free stream velocity; ω is the fall velocity; w is the work done and cf is the bottom friction coefficient.

$$q \;=\; \rho c_f \frac{\varepsilon_b}{tan\phi}\left[{u_b}^3 - \frac{tan\beta}{tan\phi}{u_b}^3\right] + \rho c_f \frac{\varepsilon_s(1-\varepsilon_b)}{\omega}\left[{u_b}^3 - \frac{\varepsilon_s(1-\varepsilon_b)}{\omega} tan\beta {u_b}^5\right] \ldots\ldots\ldots\ldots 2.9$$

where the effect of bed slope was included with the second and final terms of the equation.

2.4.1.1 XBeach Model

XBeach is a nearshore numerical model which was introduced by Roelvink et al. (2009) for the calculations of responses due to extreme wave conditions of storms, hurricanes, dune erosion and overwash for a wide range of field conditions. It is a 2DH, depth averaged model which solves coupled short wave energy, infra-gravity wave propagation, sediment transport and morphological changes. It is an open source model which made it popular among users of coastal researches which has been validated from a range of 1D flumes to different 2DH field scales (McCall et al., 2010).

A simple schematic representation of how the model works is given in figure 2.3. The model solves the directional spreading of infragravity waves and time-varying currents using the short wave action balance (eq. 2.10) on the scale of wave groups. A roller energy balance (eq. 2.11) is used for the calculation of energy dissipations in the wave breaking process in shallow waters. The short wave induced mass flux and return flows are calculated using the Generalized Lagrangian Mean (GLM) approach (eq. 2.12) which is

then used to obtain Eularian velocities.

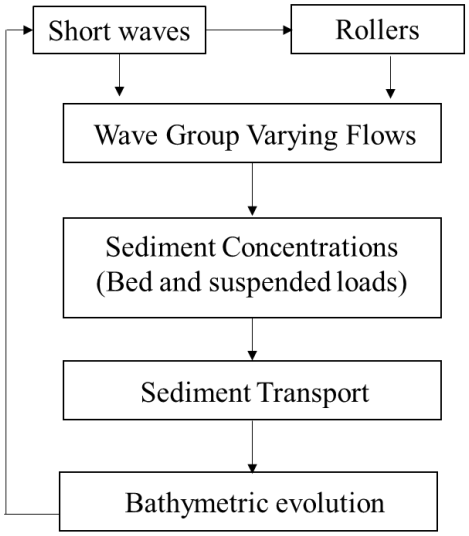

Fig. 2.3 A schematic diagram of XBeach calculation process

$$\frac{\partial A}{\partial t}+\frac{\partial c_{gx}A}{\partial x}+\frac{\partial c_{gy}A}{\partial y}+\frac{\partial c_{\theta}A}{\partial \theta}=-\frac{D_{waves}}{\sigma} \quad \text{.....2.10}$$

where $A = E/\sigma$, the wave energy by E and intrinsic wave frequency by σ; are wave group velocities in both x and y directions respectively; θ as the refraction due to bottom and currents and energy dissipation due to wave breaking as D.

$$\frac{\partial E_{roller}}{\partial t}+\frac{\partial c_x E_{roller}}{\partial x}+\frac{\partial c_y E_{roller}}{\partial y}+\frac{\partial c_{\theta} E_{roller}}{\partial \theta}=-D_{rooler}+D_{waves} \quad \text{.....2.11}$$

where the roller energy (E_{roller}) balance is included with dissipation energy from the short waves (E_{waves}). The GLM velocity equation are as follows;

$$\frac{\partial u^L}{\partial t}+u^L\frac{\partial u^L}{\partial x}+v^L\frac{\partial u^L}{\partial y}-v_h\left(\frac{\partial^2 u^L}{\partial x^2}+\frac{\partial^2 u^L}{\partial y^2}\right)=-g\frac{\partial \eta}{\partial x}-\frac{c_f u^E\sqrt{(1.16u_{rms})^2+(u^E)^2+(v^E)^2}}{h}+\frac{F_x}{\rho h}$$

.....2.12

$$\frac{\partial v^L}{\partial t}+v^L\frac{\partial v^L}{\partial y}+u^L\frac{\partial v^L}{\partial x}-v_h\left(\frac{\partial^2 v^L}{\partial y^2}+\frac{\partial^2 v^L}{\partial x^2}\right)=-g\frac{\partial \eta}{\partial y}-\frac{c_f v^{\mathrm{E}}\sqrt{(1.16u_{rms})^2+(u^{\mathrm{E}})^2+(v^{\mathrm{E}})^2}}{h}+\frac{F_y}{\rho h} \quad \text{.....2.13}$$

$$\frac{\partial \eta}{\partial t}+\frac{\partial u^L h}{\partial x}+\frac{\partial v^L h}{\partial y}=0 \quad \text{.....2.14}$$

where L represent the GLM velocities and E for Eularian velocities in x (u) and y (v) directions; the wave and roller forcing terms as F_x and F_y respectively; the water depth with h; υ_h by the horizontal viscosity coefficient; c_f the friction factor.

The sediment transport rates are calculated in the x (S_x) and y (S_y) direction by the eq. 2.15 and 2.16 respectively. The sediment concentration in a water column acts as a term for the advection-diffusion equation for sediments which is obtained by computing hydrodynamics as in eq. 2.17.

$$\left.\begin{aligned} S_x &= hCu^{\mathrm{E}}-D_s h\frac{\partial C}{\partial x} \\ S_y &= hCv^{\mathrm{E}}-D_s h\frac{\partial C}{\partial y} \end{aligned}\right\} \quad \text{.....2.15}$$

$$\text{.....2.16}$$

$$\frac{\partial hC}{\partial t}+\frac{\partial hCu^{\mathrm{E}}}{\partial x}+\frac{\partial hCv^{\mathrm{E}}}{\partial y}+\frac{\partial}{\partial x}(D_s h\frac{\partial C}{\partial x})+\frac{\partial}{\partial y}(D_s h\frac{\partial C}{\partial y})=\frac{hC_{eq}-hC}{T_s} \quad \text{.....2.17}$$

where C denotes the depth average sediment concentrations; D_s as the sediment diffusion coefficient; T_s as the sediment concentration adaptation time scales. The equilibrium sediment concentration, C_{eq} (eq. 2.18) is calculated using the Soulsby Van Rijn formulation (Soulsby, 1997). In the equation, critical transport velocity is given by u_{cr} (eq. 2.19) based on Shields.

$$C_{eq}=\frac{A_{sb}+A_{ss}}{h}(\sqrt{u^2_{stirring}}-u_{cr})^{2.4} \quad \text{.....2.18}$$

$$u_{stirring}=\sqrt{(u^{\mathrm{E}})^2+(v^{\mathrm{E}})^2}-0.018\frac{u_{rms}}{C_d} \quad \text{.....2.19}$$

where C_d is the short wave related drag coefficient and A_{ss} and A_{sb} are the suspended and bed load sediment transport coefficients respectively. The bed load and suspended load transport rates are calculated by the formulae introduced by van Rijn (2007). Based on the gradients in the sediment transport the bed level change (eq. 2.20) will be calculated including a morphological acceleration factor f_{mor} which varies between 0-10. Use of values within the limit would accelerate the morphological time with respect to the hydrodynamic scale which could be used to save simulation time of the model.

$$\frac{\partial z_b}{\partial t} + \frac{f_{mor}}{(1-p)}\left(\frac{\partial q_x}{\partial x} + \frac{\partial q_y}{\partial y}\right) = 0 \quad \text{.....2.20}$$

2.4.1.2 Large Eddy Simulation Model

The LES model was developed by Wijayarathna (2000) and sediment pick up and advection model was added later on by Suzuki (2004). In the current study, only the flow model will be used in simulation results. Thus the flow model descriptions and governing equations are given in the paper. For further clarification of the model, Niroshinie (2014) could be referred. The LES approach is used for the accurate prediction of fluid particle velocities, turbulence and eddies generated at wave breaking locations which is important for proper estimation of wave hydrodynamics near high turbulence regions hydrodynamics. The LES approach is used for higher Reynolds turbulence flows which separates the small and large scale eddies. The Reynolds averaged Navier Stokes equation (eq. 2.21), continuity equation (eq. 2.22) are used to resolve large eddies created while the small eddies are solved using a turbulence model by a sub-grid scale (SGS) approach.

$$\frac{\partial \overline{u_i}}{\partial t} + \overline{u_j}\frac{\partial \overline{u_i}}{\partial x_j} = -\frac{1}{\rho}\frac{\partial \overline{p}}{\partial x_i} + v\frac{\partial^2 \overline{u_i}}{\partial {x_j}^2} - \frac{\partial}{\partial x_j}\left(\tau_{ij}\right) + g_i \quad \text{.....2.21}$$

$$\frac{\partial \overline{u_i}}{\partial x_i} = 0 \quad \text{.....2.22}$$

where $\overline{u_i}$ is the spatially averaged velocity over the grid size, t the time, x_i (i = 1, 2 and 3) each coordinate components, ρ the density of fluid, p the pressure, v the molecular

viscosity, g the gravitational acceleration, and τ_{ij} the sub-grid scale (SGS) stress which is expressed in the form of Reynold's stress (eq. 2.23).

$$\tau_{ij} = \rho\overline{u_i' u_j'} = \rho\left(\overline{u_i u_j} - \overline{u_i}\,\overline{u_j}\right) \quad \text{2.23}$$

$$u_i = \overline{u_\iota} + u_i' \quad \text{2.24}$$

where u_i' is the velocity due to small scale turbulence with a representative length smaller than the grid size as per the equation 1d. The SGS stress, τ_{ij} (eq. 2.25) is estimated by the Smagorinsky (1963) model (eq. 2.27).

$$\tau_{ij} = \rho\overline{u'_\iota u'_J} = \left(\overline{u'_\iota u'_J} - \overline{u'}_i \overline{u'}_j\right) \quad \text{2.25}$$

$$u_i = \overline{u_\iota} + u'_i \quad \text{2.26}$$

$$\tau_{ij} = -2V_e\overline{D_{\iota J}} \quad \text{2.27}$$

where V_e could be given as in eq. 2.28 which represent the viscosity coefficient and $\overline{D_{\iota J}}$ (eq. 2.29) is the strain rate.

$$V_e = (C_s\Delta)^2\sqrt{2\overline{D_{\iota J}D_{\iota J}}} \quad \text{2.28}$$

$$\overline{D_{\iota J}} = \frac{1}{2}\left(\frac{\partial\overline{u_\iota}}{\partial x_j} + \frac{\partial\overline{u_J}}{\partial x_i}\right) \quad \text{2.29}$$

where C_s is the Smagorinsky coefficient and Δ (eq. 2.30) is the spatial length scale as given below;

$$\Delta = (\Delta x_1 \Delta x_2 \Delta x_3)^{\frac{1}{3}} \quad \text{2.30}$$

In eq. 2.30, the values of $\Delta x_1, \Delta x_2, \Delta x_3$ are as the grid spacing lengths adopted by the user in which for this study, it is 1 cm in each direction. The SGS dissipation term which is given in eq. 2.21 is a complicated term to resolve (eq. 2.31) at the boundary conditions in 3-dimensional models which was further approximated to eq. 2.32.

$$-\frac{\partial}{\partial x_j}\left(\tau_{ij}\right) = -\frac{\partial}{\partial x_j}\left[-2(C_s\Delta)^2\sqrt{\frac{1}{2}\left(\frac{\partial \overline{u_i}}{\partial x_j}+\frac{\partial \overline{u_j}}{\partial x_i}\right)^2}\right]\frac{1}{2}\left(\frac{\partial \overline{u_i}}{\partial x_j}+\frac{\partial \overline{u_j}}{\partial x_i}\right) \quad \text{.....2.31}$$

$$-\frac{\partial}{\partial x_j}\left(\tau_{ij}\right) = -\left[-2(C_s\Delta)^2\sqrt{\frac{1}{2}\left(\frac{\partial \overline{u_i}}{\partial x_j}+\frac{\partial \overline{u_j}}{\partial x_i}\right)^2}\right]\frac{\partial}{\partial x_j}\left[\frac{1}{2}\left(\frac{\partial \overline{u_i}}{\partial x_j}+\frac{\partial \overline{u_j}}{\partial x_i}\right)\right] \quad \text{.....2.32}$$

The equation is further simplified by using the continuity equation (eq. 2.33). By replacing x_1, x_2, x_3 with x, y, z and u_1, u_2, u_3 with u, v, w, the simplified equation for velocities of each directions could be obtained as given in eq. 2.34, 2.35 and 2.36 respectively.

$$-\frac{\partial}{\partial x_j}\left(\tau_{ij}\right) = (C_s\Delta)^2\sqrt{\frac{1}{2}\left(\frac{\partial \overline{u_i}}{\partial x_j}+\frac{\partial \overline{u_j}}{\partial x_i}\right)^2}\frac{\partial^2 \overline{u_i}}{\partial {x^2}_j} \quad \text{.....2.33}$$

$$\frac{\partial \bar{u}}{\partial t}+\bar{u}\frac{\partial \bar{u}}{\partial x}+\bar{v}\frac{\partial \bar{u}}{\partial y}+\bar{w}\frac{\partial \bar{u}}{\partial z} = -\frac{1}{\rho}\frac{\partial \bar{p}}{\partial x}+v\left(\frac{\partial^2 \bar{u}}{\partial x^2}+\frac{\partial^2 \bar{u}}{\partial y^2}+\frac{\partial^2 \bar{u}}{\partial z^2}\right)$$
$$+(C_s\Delta)^2\sqrt{\frac{1}{2}}\left|\left(2\frac{\partial \bar{u}}{\partial x}+\frac{\partial \bar{u}}{\partial y}+\frac{\partial \bar{v}}{\partial x}+\frac{\partial \bar{u}}{\partial z}+\frac{\partial \bar{w}}{\partial z}\right)\right|\left(\frac{\partial^2 \bar{u}}{\partial x^2}+\frac{\partial^2 \bar{u}}{\partial y^2}+\frac{\partial^2 \bar{u}}{\partial z^2}\right)-g\sin\theta$$
.....2.34

$$\frac{\partial \bar{v}}{\partial t}+\bar{u}\frac{\partial \bar{v}}{\partial x}+\bar{v}\frac{\partial \bar{v}}{\partial y}+\bar{w}\frac{\partial \bar{v}}{\partial z} = -\frac{1}{\rho}\frac{\partial \bar{p}}{\partial y}+v\left(\frac{\partial^2 \bar{v}}{\partial x^2}+\frac{\partial^2 \bar{v}}{\partial y^2}+\frac{\partial^2 \bar{v}}{\partial z^2}\right)$$
$$+(C_s\Delta)^2\sqrt{\frac{1}{2}}\left|\left(\frac{\partial \bar{v}}{\partial x}+\frac{\partial \bar{u}}{\partial y}+2\frac{\partial \bar{v}}{\partial y}+\frac{\partial \bar{v}}{\partial z}+\frac{\partial \bar{w}}{\partial y}\right)\right|\left(\frac{\partial^2 \bar{v}}{\partial x^2}+\frac{\partial^2 \bar{v}}{\partial y^2}+\frac{\partial^2 \bar{v}}{\partial z^2}\right) \quad \text{.....2.35}$$

$$\frac{\partial \bar{w}}{\partial t}+\bar{u}\frac{\partial \bar{w}}{\partial x}+\bar{v}\frac{\partial \bar{w}}{\partial y}+\bar{w}\frac{\partial \bar{w}}{\partial z} = -\frac{1}{\rho}\frac{\partial \bar{p}}{\partial z}+v\left(\frac{\partial^2 \bar{w}}{\partial x^2}+\frac{\partial^2 \bar{w}}{\partial y^2}+\frac{\partial^2 \bar{w}}{\partial z^2}\right)$$
$$+(C_s\Delta)^2\sqrt{\frac{1}{2}}\left|\left(\frac{\partial \bar{w}}{\partial x}+\frac{\partial \bar{u}}{\partial z}+\frac{\partial \bar{w}}{\partial y}+\frac{\partial \bar{v}}{\partial z}+2\frac{\partial \bar{w}}{\partial z}\right)\right|\left(\frac{\partial^2 \bar{w}}{\partial x^2}+\frac{\partial^2 \bar{w}}{\partial y^2}+\frac{\partial^2 \bar{w}}{\partial z^2}\right)-g\cos\theta \quad \text{.....2.36}$$

where θ is the inclined angle between the horizon and x-axis and $\Delta = (\Delta x \Delta y \Delta z)^{1/3}$.

2.4.1.3 WD - Princeton Ocean Model

The model was initially introduced by Mellor in 1977 which has been improved up until the present by various users due to the availability of the full code written in FORTRAN 77 to the public users. In this section a brief introduction to the flow model is given where more information is available in the user manual by Mellor (1998). The model contains an embedded second momentum turbulence closure sub-model which provides with vertical mixing coefficients. It uses a sigma coordinate system in vertical and a curvilinear orthogonal coordinate in horizontal with an "Arakawa C" differencing scheme (Fig. 2.6). The horizontal time difference is explicit whereas the vertical is implicit. It has a free surface and a split time step where the external mode (vertically average) is two-dimensional with a shorter time step and the internal mode (vertical structure) is three-dimensional with a longer time step (Fig. 2.4). The advantage of using two modes in calculation process is to reduce the computational time by solving velocity transport separately from 3D calculation of velocity and thermodynamics (Chau, 2001). In the model, the complete thermodynamics have been implemented and the version of the model which was revised with the inclusion of sediment transport and bed profile evolution model was used in the results of this research.

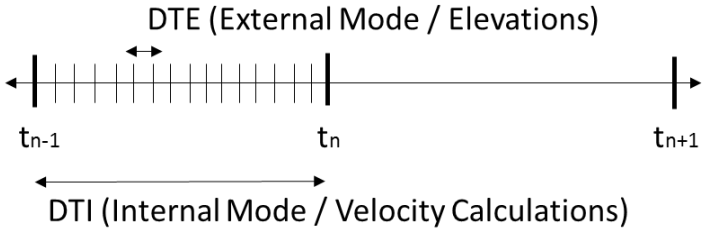

Fig. 2.4 External and Internal Time Step of POM

A general schematic representation of the entire model calculation process is given in Fig. 2.5. The figure shows the addition of silt/mud transport and sand transport to the internal mode calculations. The users are given the opportunity to include the surface and lateral boundary conditions according to their interest. The bottom is arranged to a sigma coordinate system (eq. 2.37) where *x, y, z* represent the Cartesian coordinates.

$$x^* = x, y^* = y, \sigma = \frac{z-\eta}{H+\eta}, t^* = t \quad \text{.....2.37}$$

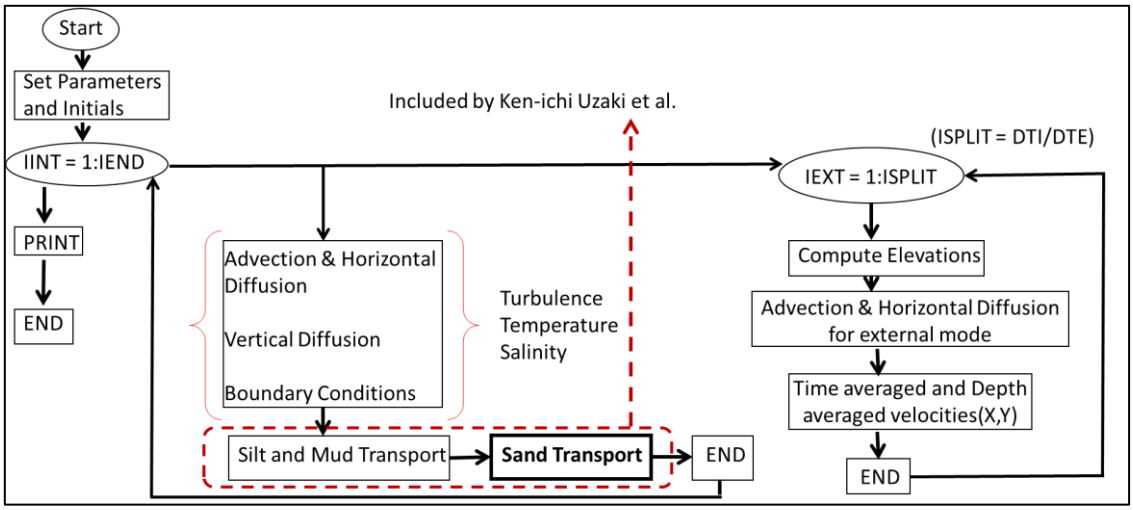

Fig. 2.5 A schematic representation of POM calculation procedure

The basic equations include the continuity equation (eq. 2.38), momentum equation (eq. 2.39 and eq. 2.40), temperature (2.41) and salinity equations (eq. 2.42) which will not be used for this research purpose.

$$\frac{\partial DU}{\partial t}+\frac{\partial DV}{\partial y}+\frac{\partial \omega}{\partial \sigma}+\frac{\partial \eta}{\partial t}=0 \quad \text{.....2.38}$$

$$\frac{\partial UD}{\partial t}+\frac{\partial U^2D}{\partial x}+\frac{\partial UVD}{\partial y}+\frac{\partial U\omega}{\partial \sigma}-fVD+\frac{gD(\partial \eta)}{\partial x}+\frac{gD^2}{\rho_o}\int_\sigma^o\left[\frac{\partial \rho'}{\partial x}-\frac{\sigma'}{D}\frac{\partial D}{\partial x}\frac{\partial \rho'}{\partial \sigma'}\right]d\sigma'=$$

$$\frac{\partial}{\partial \sigma}\left[\frac{K_M}{D}\frac{\partial U}{\partial \sigma}\right]+F_x \quad \text{.....2.39}$$

$$\frac{\partial VD}{\partial t}+\frac{\partial UVD}{\partial x}+\frac{\partial V^2D}{\partial y}+\frac{\partial V\omega}{\partial \sigma}+fUD+\frac{gD(\partial \eta)}{\partial y}+\frac{gD^2}{\rho_o}\int_\sigma^o\left[\frac{\partial \rho'}{\partial y}-\frac{\sigma'}{D}\frac{\partial D}{\partial y}\frac{\partial \rho'}{\partial \sigma'}\right]d\sigma'=$$

$$\frac{\partial}{\partial \sigma}\left[\frac{K_M}{D}\frac{\partial V}{\partial \sigma}\right]+F_y \quad \text{.....2.40}$$

$$\frac{\partial TD}{\partial t}+\frac{\partial TUD}{\partial x}+\frac{\partial TVD}{\partial y}+\frac{\partial T\omega}{\partial \sigma}=\frac{\partial}{\partial \sigma}\left[\frac{K_H}{D}\frac{\partial T}{\partial \sigma}\right]+F_T-\frac{\partial R}{\partial z} \quad \text{.....2.41}$$

$$\frac{\partial SD}{\partial t}+\frac{\partial SUD}{\partial x}+\frac{\partial SVD}{\partial y}+\frac{\partial S\omega}{\partial \sigma}=\frac{\partial}{\partial \sigma}\left[\frac{k_H}{D}\frac{\partial S}{\partial \sigma}\right]+F_S \quad \text{.....2.42}$$

$$\frac{\partial q^2 D}{\partial t}+\frac{\partial U q^2 D}{\partial x}+\frac{\partial V q^2 D}{\partial x}+\frac{\partial \omega q^2}{\partial \sigma}=\frac{\partial}{\partial \sigma}\left[\frac{K_q}{D}\frac{\partial q^2}{\partial \sigma}\right]+\frac{2K_M}{D}\left[\left(\frac{\partial U}{\partial \sigma}\right)^2+\left(\frac{\partial V}{\partial \sigma}\right)^2\right]+\frac{2g}{\rho_o}K_H\frac{\partial \overline{\rho}}{\partial \sigma}-\frac{2Dq^3}{B_1 l}+$$
$$F_q \quad \text{.....2.43}$$

$$\frac{\partial q^2 lD}{\partial t}+\frac{\partial U q^2 lD}{\partial x}+\frac{\partial V q^2 lD}{\partial y}+\frac{\partial \omega q^2 l}{\partial \sigma}=\frac{\partial}{\partial s}\left[\frac{K_q}{D}\frac{\partial q^2 l}{\partial \sigma}\right]+E_1 l\left(\frac{K_M}{D}\left[\left(\frac{\partial U^2}{\partial \sigma}\right)^2+\left(\frac{\partial V}{\partial \sigma}\right)^2\right]+\right.$$
$$\left.E_3\frac{g}{\rho_o}K_H\frac{\partial \overline{\rho}}{\partial \sigma}\right)\overline{W}-\frac{Dq^3}{B_1}+F_l \quad \text{.....2.44}$$

where U and V represent the horizontal velocities and ω, the sigma coordinate vertical velocity which is transformed by the Cartesian velocity W (eq. 2.45). Turbulence energy equation (eq. 2.43 and 2.44) and horizontal viscosity and diffusion terms are defined in eq. 2.46, 2.47 and 2.49.

$$W=\omega+U\left(\sigma\frac{\partial D}{\partial x}+\frac{\partial \eta}{\partial x}\right)+V\left(\sigma\frac{\partial D}{\partial y}+\frac{\partial \eta}{\partial y}\right)+\sigma\frac{\partial D}{\partial t}+\frac{\partial \eta}{\partial t} \quad \text{.....2.45}$$

$$F_x=\frac{\partial}{\partial x}\left(H\tau_{xx}\right)+\frac{\partial}{\partial y}\left(H\tau_{xy}\right) \quad \text{.....2.46}$$

$$F_y=\frac{\partial}{\partial x}\left(H\tau_{xy}\right)+\frac{\partial}{\partial y}\left(H\tau_{yy}\right) \quad \text{.....2.47}$$

where

$$\tau_{xx}=2A_M\frac{\partial U}{\partial x},\tau_{xy}=\tau_{yx}=A_M\left(\frac{\partial U}{\partial y}+\frac{\partial V}{\partial x}\right),\tau_{yy}=2A_M\frac{\partial V}{\partial y} \quad \text{.....2.48}$$

Also,

$$F_\phi=\frac{\partial}{\partial x}(Hq_x)+\frac{\partial}{\partial y}\left(Hq_y\right) \quad \text{.....2.49}$$

where ϕ represent the terms of *T, S,* q^2, q^2l which are the potential temperature, salinity, twice the turbulence kinetic energy and q^2 $\times$ turbulence length scale respectively. The arakawa C grid system which represent the horizontal grids system is shown in Fig. 2.6 below;

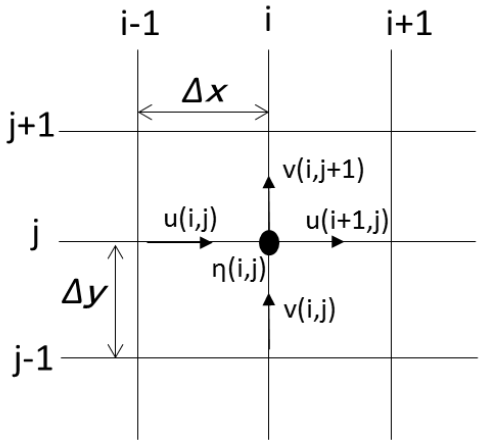

Fig. 2.6 Arakawa C Grids

2.4.2 Heterogeneous Behavior of Sediments in Numerical Simulation

Most of the simulations for sediment transport use a domain of homogeneous and well sorted sand in both cross-shore and longshore directions (Gallagher et al., 2011) even though it is quite deviating from the reality. Many literature has mentioned the importance of considering the heterogeneous behavior of sediments in the surf zone for better analysis of coastal morphology (Inman and Chamberlain, 1955; Moustzouris, 1989; Jiang et al., 2015; Holland & Elmore, 2008; Gallagher et al., 2011).

3 SEDIMENT MIXING AND EROSIVE/ACCRETIVE WAVE CONDITIONS

This chapter includes the investigations related to the sediment mixing experiments conducted in the 2D Flume environment under long term wave conditions. The sediment mixing studies were widely conducted in the field within a tidal cycle where the experiment area of interest is limited to within the wave breaking zone of the surf zone. In this study, the research scope has been extended from the ordinary research interests to investigate the sediment mixing variation along the surf zone at different time scales under two wave conditions. The experiments were conducted using tracer experiments in a small scale two-dimensional flumes at Yokohama National University.

The objective of this study was to investigate the spatial and temporal variations in the cross-shore sediment movement and mixing in the nearshore, from the swash zone to the offshore side of the surf zone under erosional and accretive wave conditions. The bed-profile variation with respect to time, quantitative values of the fluorescent particles in the cross-shore profile and depth, and temporal and spatial variations in the mixing depths are obtained from laboratory experiments. Moreover, the sediment-mixing depths along the cross shore are discussed.

3.1 Experimental Setup and Results

The laboratory experiments were conducted in a glass-walled flume at Yokohama National University. The experimental work was conducted by Takeshi Kurosaki. The length, width, and height of the flume are 18, 0.50, and 0.50 m, respectively. Fine sand was filled for an impermeable 1/20 bed slope of the flume with d_{50} = 0.2 mm, up to a thickness of 5.0 cm. Figure 3.1 shows the experimental setup of the bed profile and installation of wave gauges. Two wave gauges were installed to record the water-surface motions along the offshore and edge of the slope. In the experiments, the origin of the cross-shore distance was set at the edge of the slope. The x and z axes represented the onshore and upward directions, respectively. Fluorescent-sand tracers of blue, yellow, and red colors were horizontally placed on top of the bed layer with a mass of 6 g at each fixed cross-shore location, x = 2.05 m, 3.15 m, and 3.7 m, respectively (Fig. 3.1 and 3.2). The offshore water depth was set as 26.0 cm. Two regular wave conditions were used in this study: accretive and erosional-wave conditions.

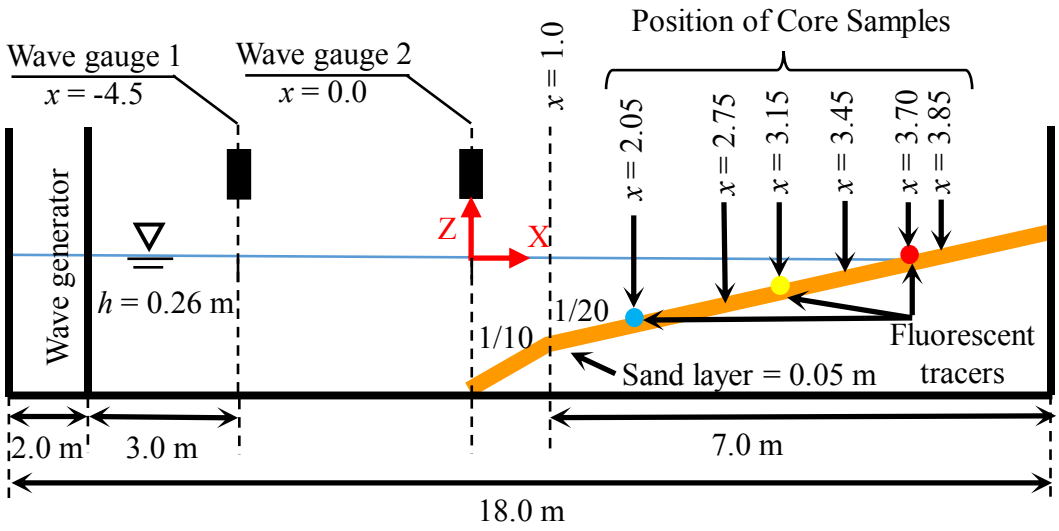

Fig. 3.1 The sloped-bed experimental setup

In the experiments, the initial sand-bed condition was set as flat with a slope of 1/20. The accretion case of waves, a wave height of 1.8 cm, and a wave period of 2.0 s were generated for 30 min. In this case, a berm was formed in the swash zone. After the accretion scenario, the erosional case of waves, a wave height of 2.8 cm, and a wave period of 8.0 s were generated for 20 min. The berm was completely eroded by the erosional waves. The two wave conditions were determined via a trial-and-error method such that the berm shape is formed and is eroded under each wave condition.

(a) Blue tracer (b) Yellow tracer (c) Red tracer

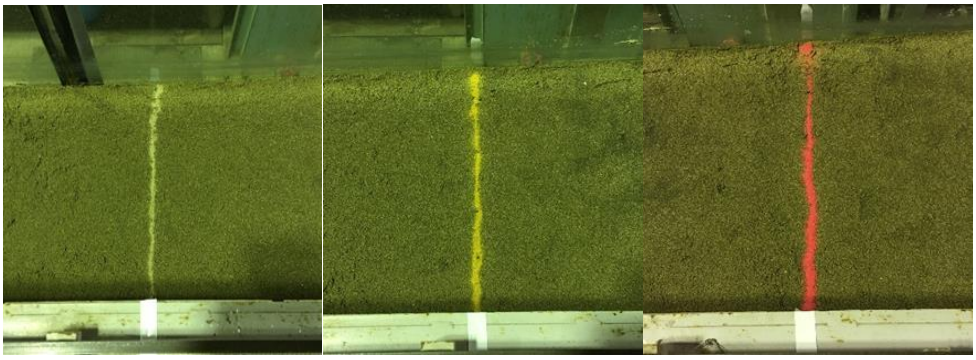

Fig. 3.2 Fluorescent-sand tracer strips placed across the flume width; (a) x = 2.05 m for blue, (b) x = 3.15 m for yellow, and (c) x = 3.70 m for red.

During the experiments, the bed-profile survey and sand-core samplings were conducted every 10 min. At each 10-min interval during the accretive and erosional-wave conditions, the wave generator was stopped and the water level was lowered until approximately h = 16 cm to remove the core samples and conduct the bed-profile survey. After removing the core samples and conducting the profile survey, the water was refilled until h = 26 cm for the next experiment. The longshore direction of the investigated area was divided into five sections, each with a width of 10 cm. To avoid unexpected sediment mixing due to core sampling, each time step of the core sampling was conducted in different sections. At each core sampling, six cores were placed at fixed cross-shore locations; i.e., x = 2.05, 2.75, 3.15, 3.45, 3.7, and 3.85 m (Fig. 3.1). The core-sampling positions were determined from the trial runs wherein the bed profile changed significantly from the initial profile. A PVC tube with a length of 12.0 cm and a diameter of 3.0 cm was used for the core sampling (Fig. 3.3a).

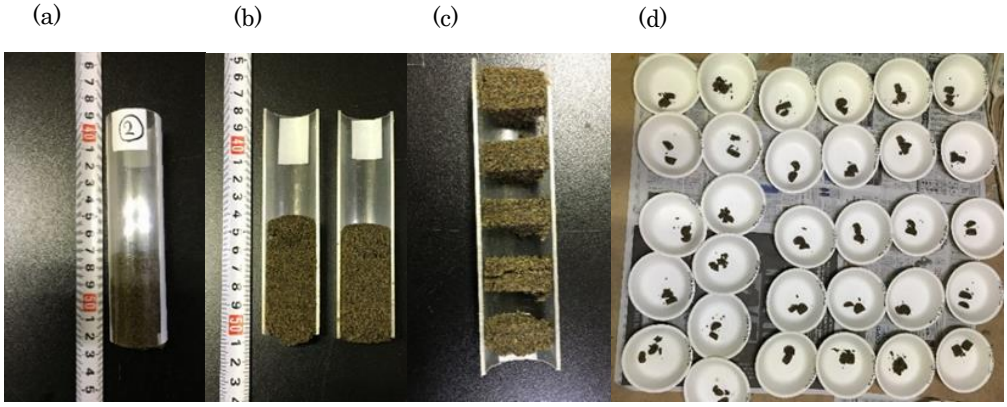

Fig. 3.3 Dividing procedure of each core; (a) sampled core, (b) split into half, (c) dividing the sample, and (d) air dried.

After collecting the cores, the tubes were split into half and divided into 1-cm sand-layer samples (Fig. 3.3b and c). Each sand-layer sample was air dried (Fig. 3.3d), and subsequently, transferred into a dark room to count the number of fluorescent-sand tracers of each color using a UV light source.

Several definitions are proposed for the mixing depths: Katoh and Tanaka (1986) suggested a core depth of 80% of a tracer has reached, and the centroids or the weighted average depths where a tracer has reached (Kraus et al., 1982). In the preliminary core-sampling test, fewer than 10 particles were found in the middle layer of a divided sample,

though the tracers were spread only on the bed surface. Thus, in this experiment, the mixing depth was defined as the depth where more than 10 tracers were found except in the top-surface layer, wherein the sampling errors were considered minimum.

Figures 3.4 show the bed-profile changes during the experiments conducted under the accretional and erosional condition. The time t is the total time from the start time of the accretion case. Under both the wave conditions, the bed profile significantly changes from the initial condition. The bed profiles where the yellow and red tracers were installed, i.e., x = 3.15 m and x = 3.70 m, respectively, fluctuated under the accretional and erosional conditions. However, the position at which the blue tracer was installed, i.e., x = 2.05 m, remained largely constant with respect to time.

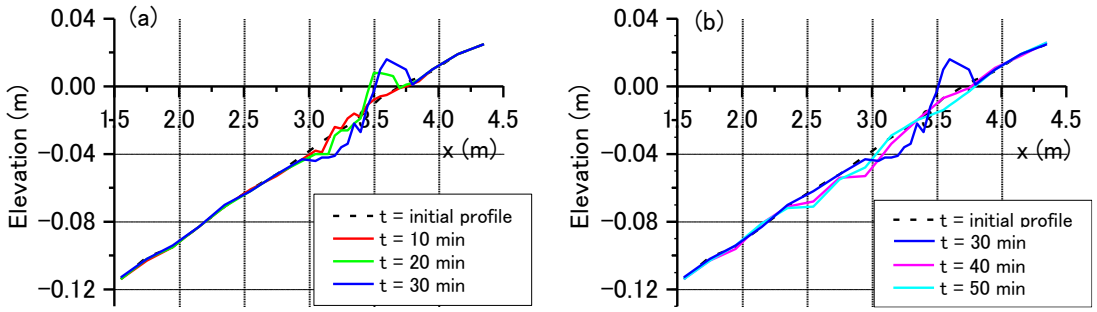

Fig. 3.4 Variation in bed profile; (a) Accretion case, and (b) Erosion case.

In the accretion case, the variation in the bed profile indicates that the berm shape was created with a height of 2 cm near the shoreline at x = 3.7 m (Fig. 3.4a). In this case, the breaking point of the wave was at approximately x = 3.25 m. The figure shows that the height of the berm increases and shifts toward the onshore side with the passage of time. In contrast, the area from x = 2.9 m to 3.4 m of the bed profile eroded during the berm formation.

After the berm was formed, the erosional waves were generated (from t = 30 min to 50 min). As the wave period was long in this case, the distance between the wave run-up and run-down points was considerable. The wave started to break at approximately x = 3.3 m. The berm started to disappear within the first 2 min of the experiment. After generating the erosional waves for 10 min, i.e., t = 40 min, the berm was completely eroded, and the bed profile largely returned to the initial profile levels (Fig. 3.4b). After generating the erosional waves for 20 min, i.e., t = 50 min, the eroded profile was

observed at the offshore side of the breaking point. In the erosion case, the wider area of the bed profile, from approximately x = 2.25 m to x = 4.0 m, was disturbed by the waves.

Figures 3.5 to 3.9 show the cross-shore and vertical distributions of the fluorescent-sand tracers for blue, yellow, and red at each time step. The vertical axis represents the elevation. The origin was set as the initial bed-profile level at each location. The solid lines in the figures indicate the bed level of each time step, shown in the title of the figures. The dashed lines indicate the bed level of the previous time step, i.e., the bed level before 10 min. The bar charts represent the total number of tracers at each layer. The tracer counts below 10 were removed from the results, except the ones at the top of the layer. The number of counts in the bar chart reached up to 100, indicating that more than 100 particles were found in the layer.

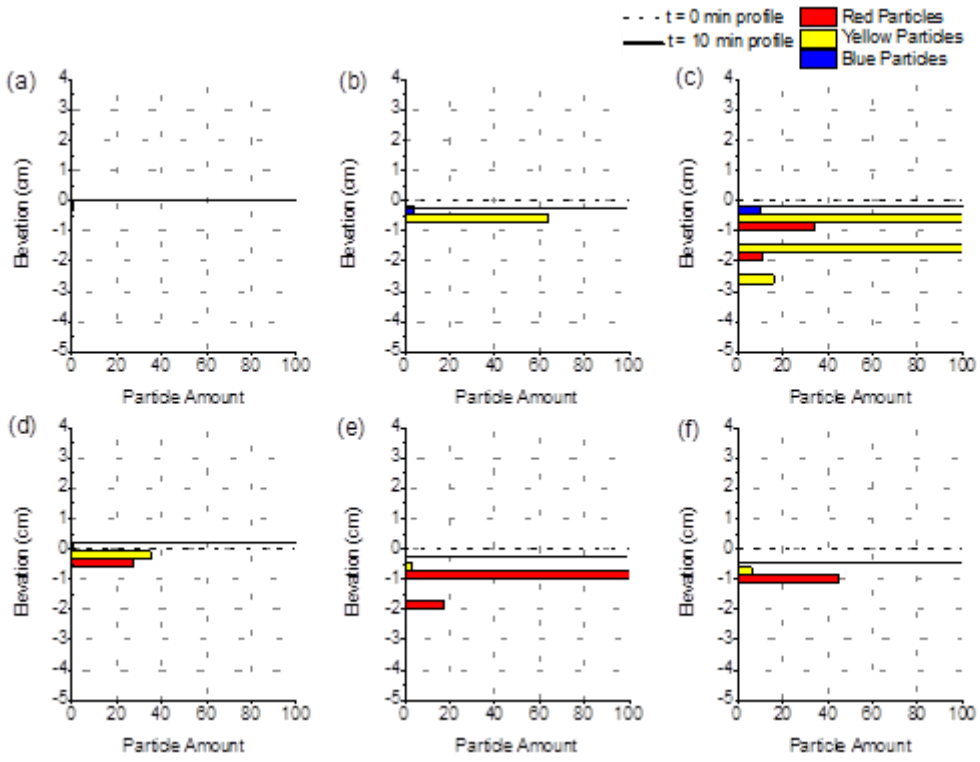

Fig. 3.5 Number of tracer particles along the depth after 10 min at each location under accretion condition; (a) x = 2.05 m, (b) x = 2.75 m, (c) x = 3.15 m, (d) x = 3.45 m, (e) x = 3.70 m, and (f) x = 3.85 m.

After the first 10 min of the experiment, as shown in Fig. 3.5 (accretion case), the blue tracers installed at x = 2.05 m (Fig. 3.5a) were found only on the surface layer at the

offshore region. Although the tracers were installed at the location, as shown in Figure 3.5a, only a few were collected at nearby locations. The yellow tracers installed at x = 3.15 m (Fig. 3.5c) were largely found at the installed location; moreover, the tracers were mixed along the depth without changing the bed profile, particularly around the impinging point. The results show that the sediment mixed before the change in topography. The red tracers installed at x = 3.70 m (Fig. 3.5e) were transported toward both onshore and offshore sides.

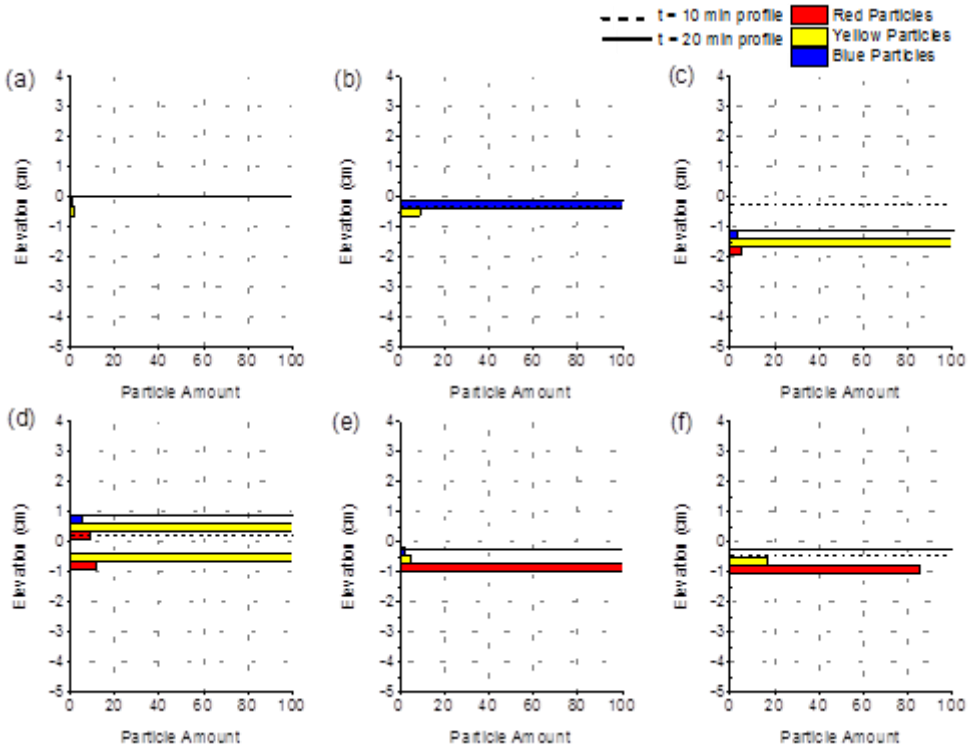

Fig. 3.6 Number of tracer particles along the depth after 20 min at each location under accretion condition; (a) x = 2.05 m, (b) x = 2.75 m, (c) x = 3.15 m, (d) x = 3.45 m, (e) x = 3.70 m, and (f) x = 3.85 m.

After 20 min from the beginning, as shown in Fig. 3.6, most of the blue tracers were transported to the area near x = 2.75 m. Few blue tracers were found on the surface of the onshore side from x = 3.15 m. The core-sample location at x = 3.15 m decreases in profile depth up to 1 cm; the location increased at x = 3.45 m by 1 cm. The maximum number of colored tracers were collected at the location x = 3.45 m.

At the end of the accretion case, i.e., t = 30 min, the yellow tracers were transported

more toward the onshore side, and the maximum number of blue tracers was found again at x = 2.75 m, as shown in Fig. 3.7. The red tracer mixed more along the depth at x = 3.70 m. The bed profile starts decreasing more than 1 cm at x = 3.15 m; however, the profile increases by 1 cm at x = 3.7 m. The highest number of tracer-gathering point shifts toward the onshore location x = 3.7 m.

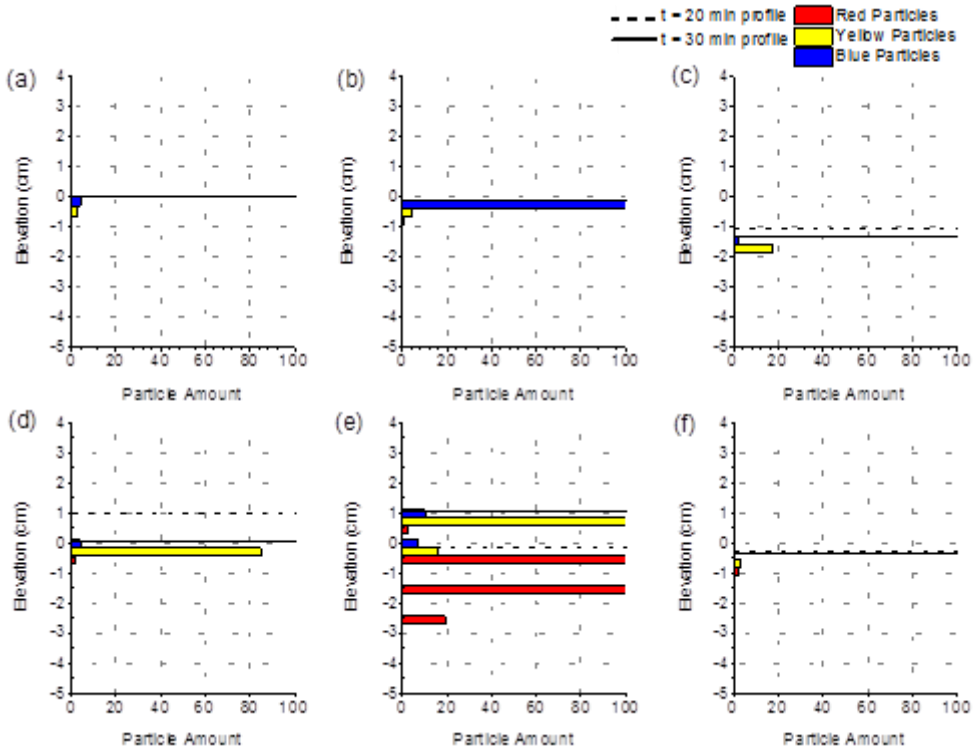

Fig. 3.7 Number of tracer particles along the depth after 30 min at each location under accretion condition; (a) x = 2.05 m, (b) x = 2.75 m, (c) x = 3.15 m, (d) x = 3.45 m, (e) x = 3.70 m, and (f) x = 3.85 m

Until the end of accretional waves, the blue tracers significantly remained at the same location, i.e., x = 2.75 m. The yellow and red tracers mixed well on the surface and along the depth at all locations except for the most offshore sampling location, i.e., x = 2.05 m. The position of highest number of all colors collected along the depth was initially recorded at x = 3.15 m; this position shifted with the progress of time until x = 3.45 m. In the beginning of the erosional-wave conditions (after 40 min from the start of the experiment, i.e., t = 40 min, as shown in Fig. 3.8), most of the blue tracers were washed away, which collects at x = 2.75 m in the previous interval. More number of yellow tracers were collected at x = 3.15 m and 3.45 m whereas more number of red tracers were located

at x = 3.7 m and x = 3.85 m. A slight decrease in the bed profile was observed at x = 2.75 m, 3.15 m, and 3.7 m. In this time step, the maximum number of colored tracers was mixed at x = 3.15 m up to a depth of 2 cm.

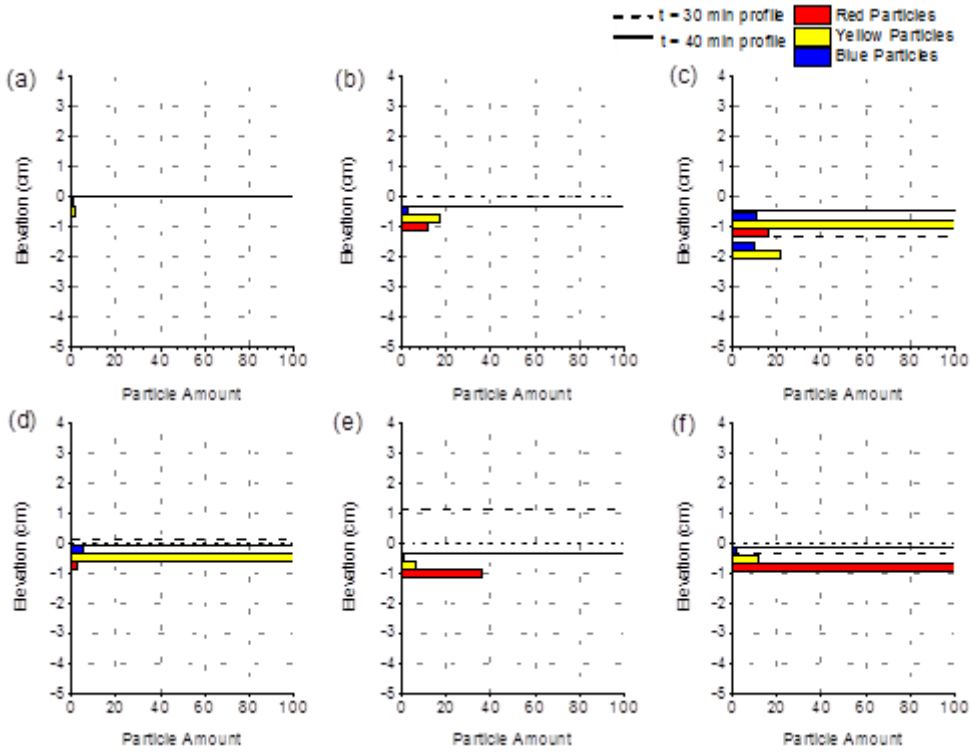

Fig. 3.8 Number of tracer particles along the depth after 40 min at each location under erosion condition; (a) x = 2.05 m, (b) x = 2.75 m, (c) x = 3.15 m, (d) x = 3.45 m, (e) x = 3.70 m, and (f) x = 3.85 m.

In this time step, the maximum number of colored tracers was mixed at x = 3.15 m up to a depth of 2 cm. At the end of the erosional wave conditions, i.e., t = 50 min, as shown in Figure 3.9, the red and yellow tracers were mixed along the depth at higher concentrations whereas the blue tracers appeared only at several locations in the surface layers. The highest mixing depth was reached at x = 2.75 m. The highest quantities of tracers was collected at x = 3.15 m.

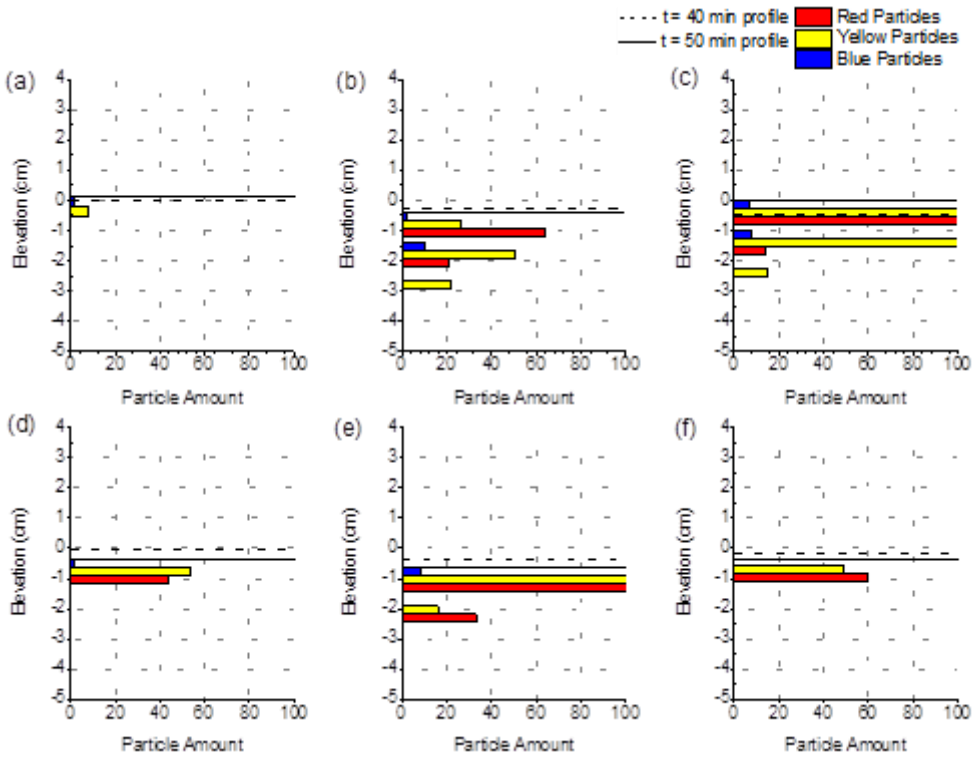

Fig. 3.9 Number of tracer particles along the depth after 50 min at each location under erosion condition; (a) x = 2.05 m, (b) x = 2.75 m, (c) x = 3.15 m, (d) x = 3.45 m, (e) x = 3.70 m, and (f) x = 3.85 m.

Using the results obtained from the tracer experiments, the temporal and spatial distributions of the mixing depth were analyzed. Figure 3.10 shows the temporal and spatial distributions of the mixing depth for the blue tracers. In the panel (a), a thick solid line indicates the surface profile at each time step. The blue tracers were installed at the most offshore location near the offshore side of the surf zone, i.e., x = 2.05 m. The maximum mixing depth during the accretion and erosion cases were 1 cm and 2 cm, respectively. In the accretion waves, the tracers mixed along the depth at the wave-breaking point, i.e., x = 3.20 m. Although the bed profile changed, the mixing depths of the blue tracers remained constant from the offshore zone to the swash zone. Under the erosional-wave conditions, a higher mixing depth was observed at x = 2.75 m, which was the offshore side of the wave-breaking point. The overall sediment movement was toward the onshore direction in the accretion case and toward the offshore direction in the erosion case in the experiment.

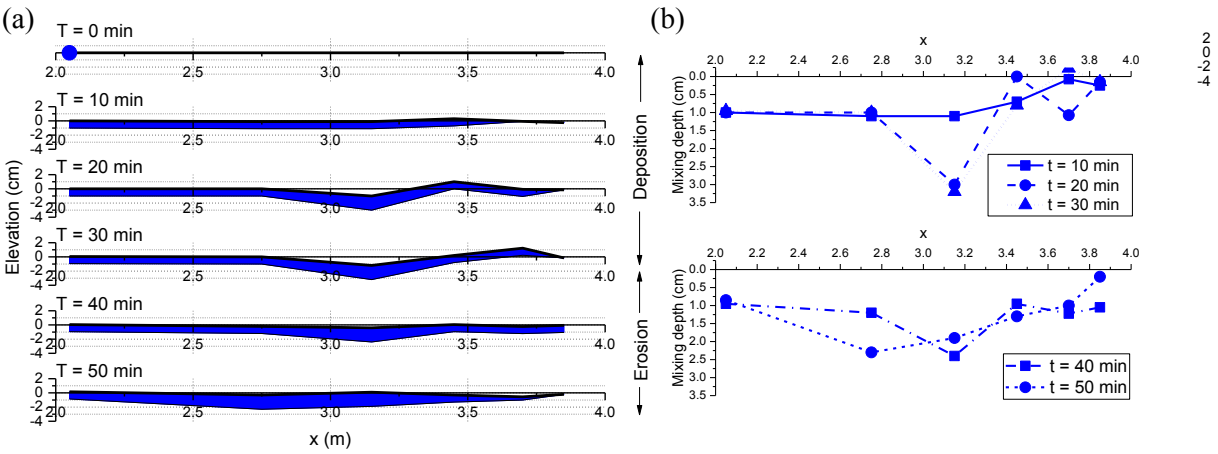

Fig. 3.10 Mixing depth of blue tracers; (a) Temporal and spatial distributions of mixing depth, (b) Mixing depths from the bed surface level of each time step.

Figure 3.11 shows the temporal and spatial distributions of the mixing depth for the yellow tracers. The yellow tracers were installed in the wave-breaking area, i.e., x = 3.15 m. The maximum mixing depth for the accretion and erosion cases was 3 cm. The mixing depths varied with respect to time and space continuously throughout the surf zone. In the beginning of the experiment, i.e., 10 min, the bed profile was largely constant, and the mixing depth around the breaking point reached up to 3.0 cm. After the mixing, the profile changed, and the berm started to form in the swash zone.

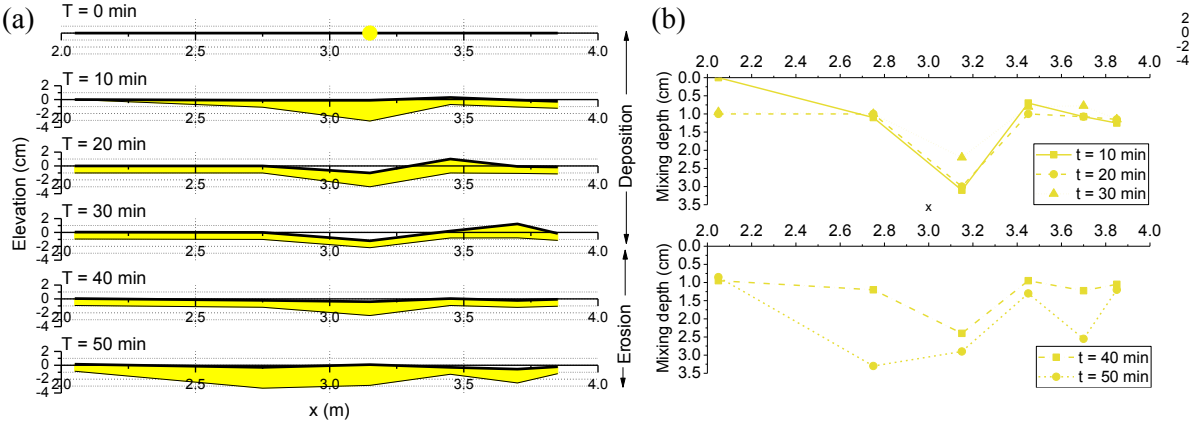

Fig. 3.11 Mixing depth of yellow tracers; (a) Temporal and spatial distributions of mixing depth, (b) Mixing depths from the bed surface level of each time step.

Fig. 3.12 shows the temporal and spatial distributions of the mixing depth for the red tracers. The red tracers were installed near the swash zone, i.e., x = 3.70 m. During the

first 20 min, the tracers were mixed only till the offshore side at $x = 2.75$ m. The sediments in the swash zone moved to the offshore side owing to the back wash and under tow. The sediment mixing occurred because of wave breaking and bore effects. Under the erosional-wave conditions, the red tracers were transported toward the offshore direction.

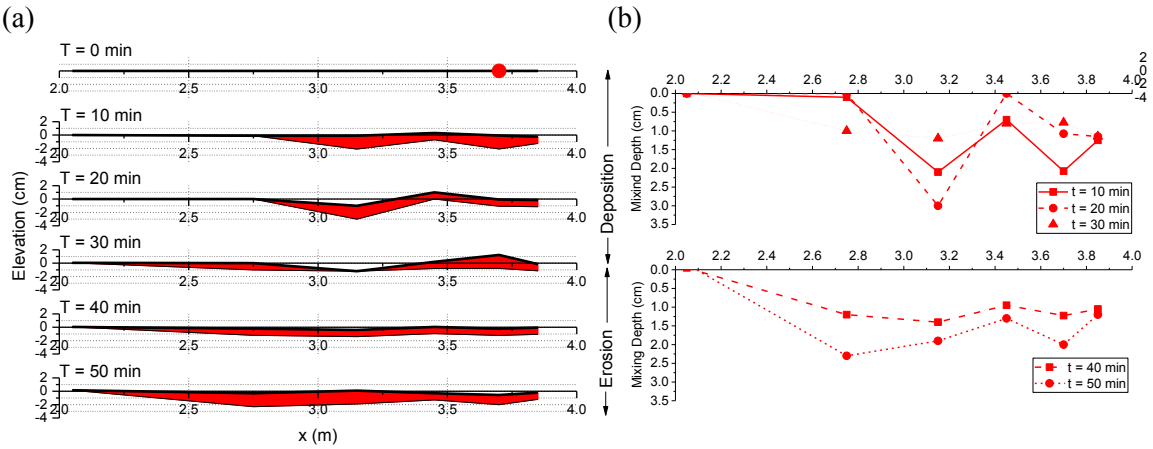

Fig. 3.12 Mixing depth of red tracers; (a) Temporal and spatial distributions of mixing depth, (b) Mixing depths from the bed surface level of each time step.

3.2 XBeach Simulation

It was initially planned to see the correlation between wave hydrodynamics to the mixing depths obtained by the experiments. For hydrodynamic purposes, Xbeach model was selected which give depth average simulation results as mentioned in Section 2. Bed Shear stress, near-bed velocities, turbulence and eddies were some of the parameter results which were interested to simulate. A stationary 2DH wave model was adopted that would effectively solve wave average equation neglecting infragravity waves. The wave grid setup arrangement is given in Fig. 3.13. The grid size for the flume experiment was changed from 1 cm, 5 cm and 10 cm in each x and y directions. However the results were only able to generate for 10 cm grid profile due to the limitation in scale by XBeach model.

The origin was set at the first wave gauge position, on the water level profile as in Fig. 3.13a. Initially the dipositive waves were generated at the boundary as a station regular wave for 30 min. Thereafter a new model was setup by defining erosive wave boundary conditions for 20 min with the new bed profile.

(a)

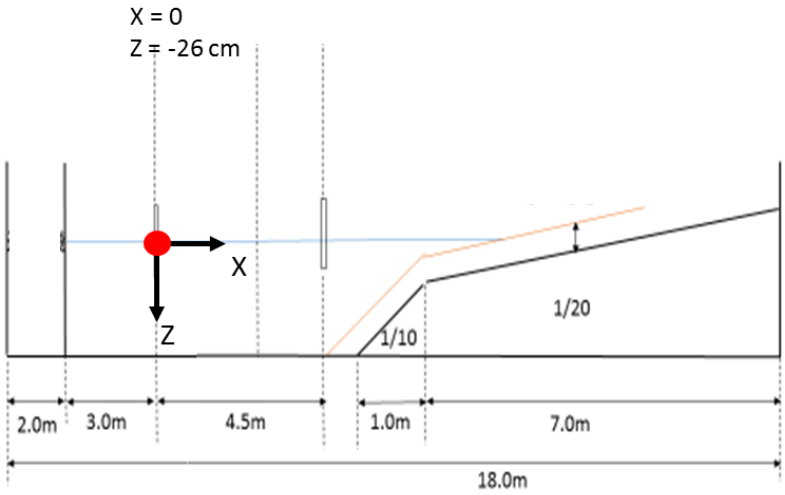

(b)

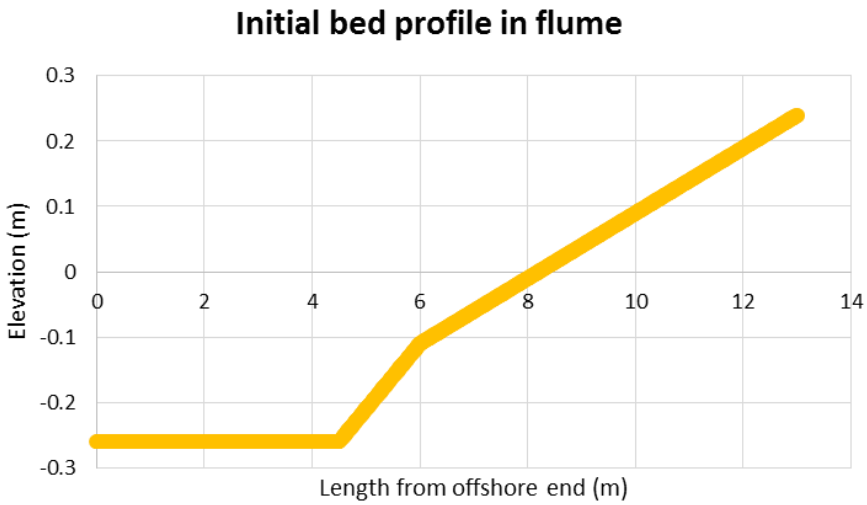

Fig. 3.13 The (a) Origin of the model and the (b) initial bed profile setup for XBeach simulations

A weakly reflective boundary at the offshore end and a no flux wall for the onshore side boundary condition was defined by the model. The both accretive and erosive models were simulated at 1 sec time interval for 20 min duration for calibration purposes. The tidal effect was switched off where the morphological option was on with no morphological acceleration considered. The Table 3.1 shows the considered parameters and model input and output parameter file for XBeach.

Table 3.1 The input and output parameter file for XBeach under accretive and erosive wave conditions

Parameter	Erosion	Deposition
Grid setup		
dx (cross-shore distance interval)	0.1	0.1
dy (long-shore distance interval)	0.1	0.1
nx (x number of grids)	130	130
ny (x number of grids)	5	5
q3d (turn on quasi 3d)	1	1
Morphological Data		
morstart (start time)	0	0
morstop (end time)	1200	1200
Flow boundary condition		
front (offshore)	1 (weakly reflective)	1 (weakly reflective)
back (onshore)	2 (no flux wall)	2 (no flux wall)
Time input		
tstart	0	0
tintg	1	1
tstop	1200	1200
Wave Boundary Condition Input		
instat	0 (regular waves)	0 (regular waves)
Hrms (Wave height)	0.028	0.018
Tm01 (wave period)	8	2
dir0 (wave direction)	270	270
Tidal conditions		
tideloc		0 (No tidal effect)
zs0		0 (water level)
Sediment Details		
D50 (Diameter size)	0.0002	0.0002

3.3 XBeach Calibration and Verification

XBeach has several calibration parameters which has to be adjusted according to the experiment environment. Some of the important calibration parameters are;

- dryslp – critical avalanching slope above water

- wetslp – critical avalanching slope below water
- hswitch – water depth at which is switched from wetslp to dryslp
- facua – calibration factor for time averaged flows due to wave skewness and asymmetry
- C – Chezy coefficient of bed friction
- morfac – morphological acceleration factor
- smax – Maximum shields parameter for equilibrium sediment concentration
- CFL – maximum courant-friedrichs-lewy number

The effect/sensitivity of above mentioned parameters on calibration and results generation have been discussed by many authors in past (Pender and Karunarathna, 2013; Vousdoukas et al., 2012; Vousdoukas et al., 2011). For the calibration of the current model setups, the bed profiles after 20 min of experiment and modeled were compared;

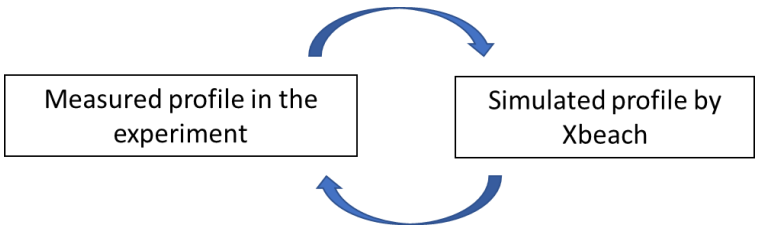

The brier skill score (BSS) values (eq. 3.1) were calculated using the bed profiles from accretive and erosive model simulation results. The accretive model results often gave negative BSS scores where the erosive model gave higher values of BSS scores generating accurate bed results (Fig. 3.14). The detailed calibration procedure and the BSS values according to each parameter changed, is given in Appendix A.

$$\mathrm{BSS} = 1 - \left[\frac{\sum|x_p - x_m|^2}{\sum|x_b - x_m|^2}\right] \quad \text{.....3.1}$$

where x_p is the predicted value; x_m is the measured value during the experiments; x_b is the initial value of bed profile. The BSS score < 0 is considered bad; 0 -0.3 as poor; 0.3 – 0.6 as reasonable/fair; 0.6 – 0.8 as good and > 0.8 to be excellent.

(a) (b)

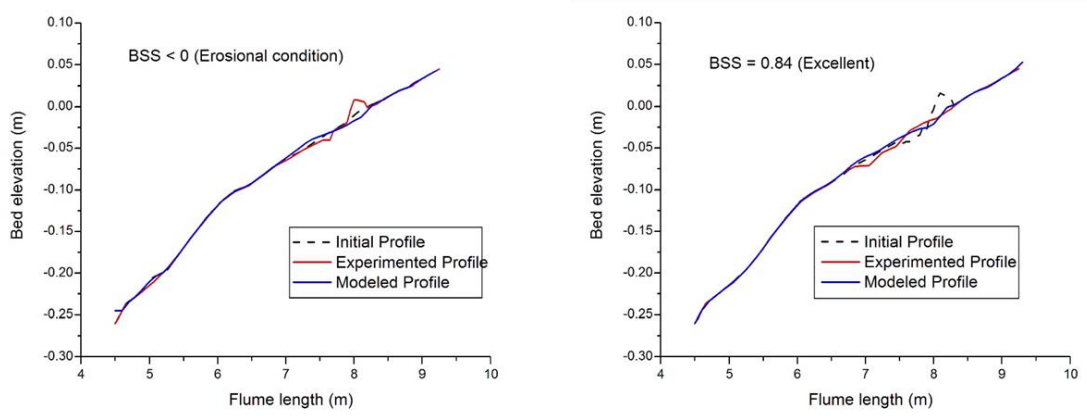

Fig. 3.14 The BSS scores and the bed elevations from experiments and simulation results for (a) accretive and (b) erosive wave conditions within 20 min interval.

During the calibration of erosive waves, 3 main calibration parameters were noted to give an excellent BSS score of 0.84 which are given below;

1. Critical Bed Slope *(mcr)* - drylp (0.1) the critical slope of cells above water
wetslp (0.2) the critical slope of cells below water

2. Facua - a parameter (γua = 0.5) determining the wave asymmetry (f_{As}) and skewness (f_{sk}) contribution in the sediment advection velocity.

$$\frac{\partial hC}{\partial t}+\frac{\partial hC(u^E-u_a sin\theta_m)}{\partial x}+\frac{\partial hC(v^E-u_a cos\theta_m)}{\partial y}+\frac{\partial}{\partial x}\left(D_h h\frac{\partial C}{\partial y}\right)=\frac{hC_{eq}-hC}{T_s} \quad \text{.....3.2}$$

$$u_a=(f_{sk}S_k-f_{As}A_s)u_{rms} \quad \text{.....3.3}$$

3. wci (=1) - affecting the wave action propagation speeds in the x- and y- directions:

$$c_x(x,y,t,\theta)=c_g\cos(\theta)+\mathrm{u^L} \quad \text{.....3.4}$$
$$c_y(x,y,t,\theta)=c_g\sin(\theta)+v^L \quad \text{.....3.5}$$

where ϑ represents the angle of incidence with respect to the x-axis, t the time variable, c_g is the group velocity and u^L and v^L are the cross-shore and along-shore depth-averaged Lagrangian velocities, which are ignored when wci = 0.

3.4 Experiment Conclusions

Laboratory flume experiments were conducted to investigate the sediment movement in the cross-shore direction with respect to time from the offshore side of the surf zone to the swash zone. Three colored fluorescent-sand tracers were placed at three different cross-shore locations: offshore side of the surf zone, wave-breaking area, and near the shoreline. During the experiments, the bed-profile observations and core sample collections were conducted at six different cross-shore locations with an interval of 10 min. The berm was created during the first 30 min by the accretional waves and was eroded in the next 20 min by the erosional waves. At 10-min intervals, the sediment mixing patterns were analyzed.

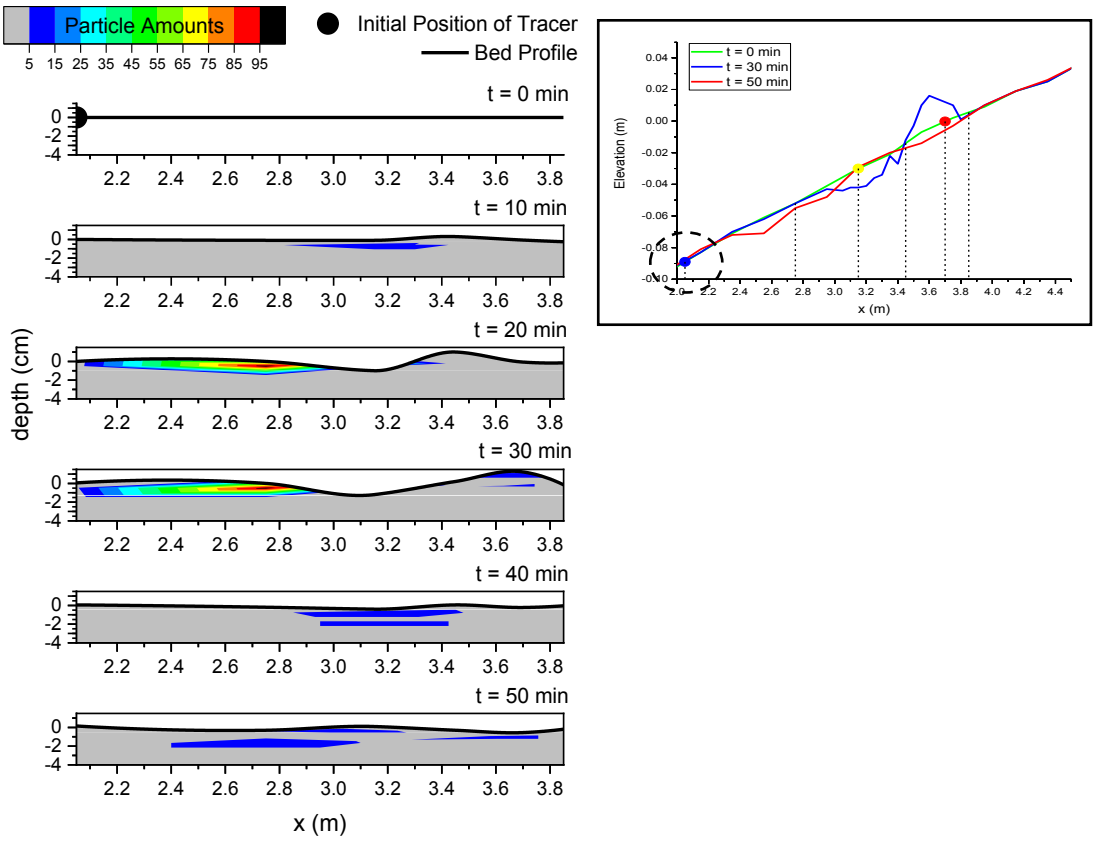

Fig. 3.15 The blue tracer mixing in space and time

During the initial 20 min time, the blue tracer movement seem to correlate with the orbital movement near the bed profile. Most of the tracer has gathered around 2.8 m location (Fig. 3.15). Tracer has been washed away to the offshore remaining less than 15

particles in most of the area after 30 min interval and the tracer has shifted to the eroded locations. Yellow tracer was mixed in depth and was moved towards the shore while most of the tracer mixing bed layer been eroded to create the berm in first 30 min. Thereafter, the tracer was washed back to the offshore side with time while mixing in depth. The maximum amounts were on the surface layers from x = 3.0 to x = 3.8 m (Fig. 3.16).

The Red tracer, on the other hand, has mixed in depth and never reached away from x = 2.8 m as seen in Fig. 3.17 during the accretive conditions. It was reached in depth under the berm area until 30 min of time. Afterwards, the tracer has been washed back to the offshore while again mixing in depth. More amount were on the surface layers from x = 2.4 m to the shore side.

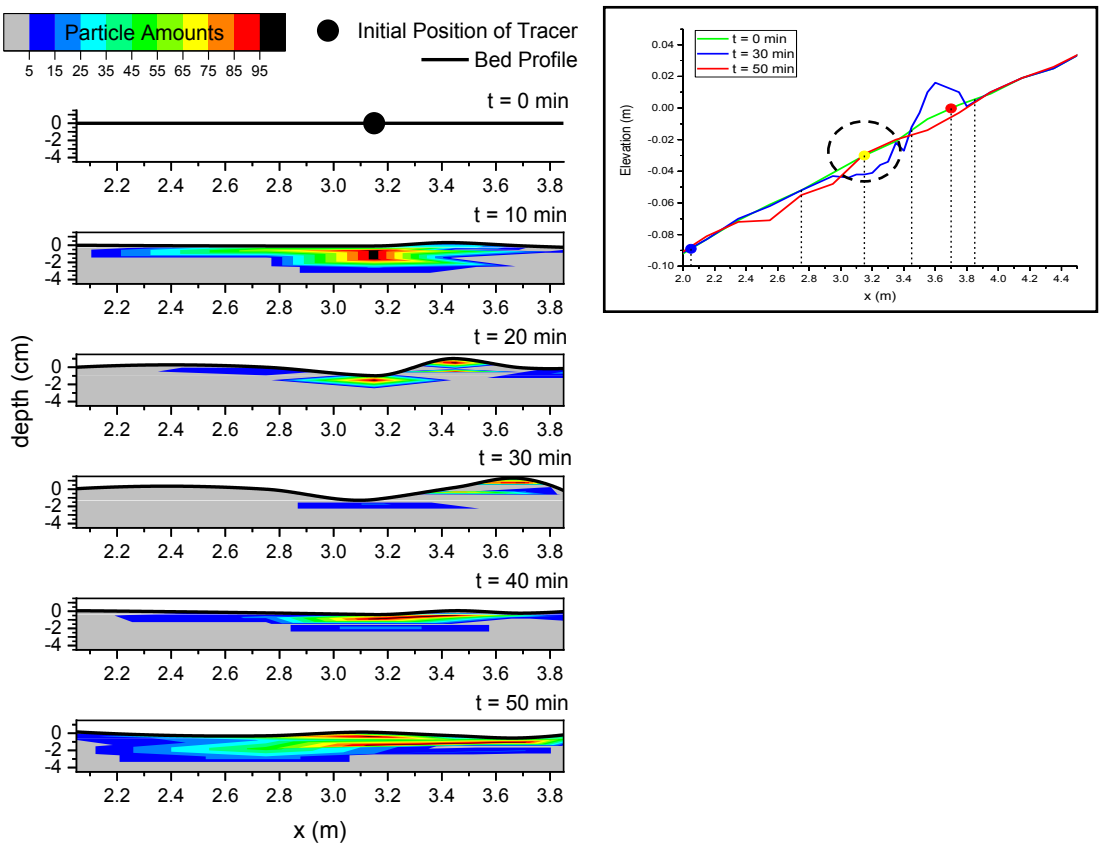

Fig. 3.16 The yellow tracer mixing in space and time

Although the variation in the bed profile is constant, the mixing depths were measured from the initial bed profile (1/20 flat slope) arranged prior to conducting the experiments. A dynamic pattern of sediment mixing occurred in the wave-breaking zones in the swash-zone direction. The highest mixing-depth location shifted to the nearby sampling location at each 10-min interval—toward the shore direction during the accretional waves and

toward the offshore direction under the erosional waves. The highest number of tracer colors was recorded at the maximum mixing-depth position at each interval.

The mixing depths and sediment movement were observed to be a combined effect of wave breaking, wave intensity, experiment duration, etc. The correlation between the mixing depths and hydrodynamic forces can be analyzed using the numerical results. The depth of disturbance (or the mixing depth) from the wave breaking and turbulence created nearshore is significant from the offshore side of the surf zone to the swash zone. The nearshore dynamics should be further studied to understand this complex scenario.

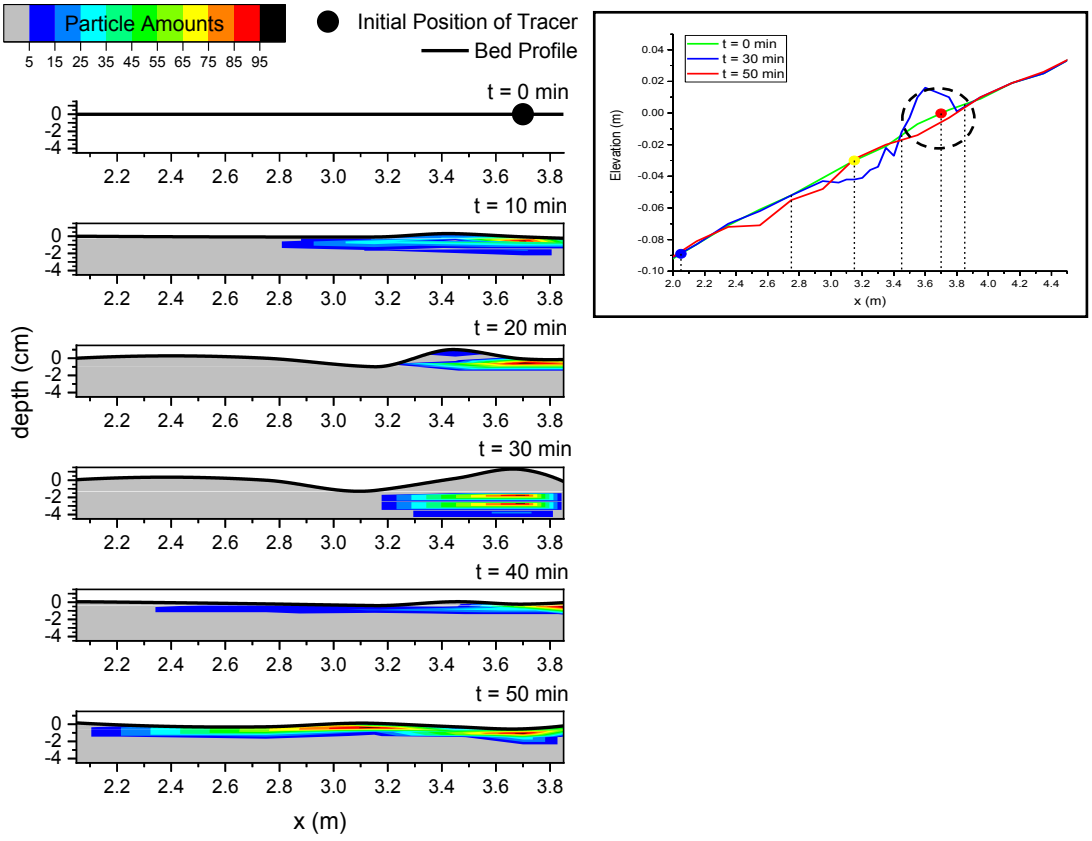

Fig. 3.17 The red tracer mixing in space and time

The hydrodynamic simulations of the experiment was failed to conduct due to the calibration difficulties of XBeach. XBeach was developed to conduct simulations related to extreme weather conditions and mainly for erosive beach profiles. The calibrations for accretive waves was very poor, however the erosive wave calibrations were acceptable.

4 SEDIMENT MIXING AND WAVE BREAKING

The present study was conducted to facilitate a hydrodynamic approach in analyzing the dependency on spatial and temporal mixing depths in the wave breaking zone. The main objective of the research was to evaluate the mixing depths along the wave breaking region and the effect of horizontal-plane eddies on sediment mixing for different wave breaking conditions. The laboratory experimental work was limited to a two-dimensional flume with regular wave conditions as same as the previous study. The experiments were conducted with collaboration with Saki Akimoto. The hydrodynamic conditions were simulated by a Large Eddy Simulation Model (LES) to in cooperate the current flow patterns and eddies created near the bed surface.

4.1 Experimental Setup and Results

Four times of flume experiments were conducted in a 2D glass fibre flume with dimensions of 0.6 m×0.6 m×18 m at Yokohama National University. A wooden sand box of 0.15 m deep and 1.0 m long was created and the box was set in the middle of the bed slope as shown in Fig 4.1. The bed slope on either sides of the sand box was 1/10, and the slope were created by impermeable aluminum sheets. The box was filled with a median diameter of 0.2 mm of fine sand. In the sand bed section, five wave gauges were fixed with a 0.2 m interval to read wave heights.

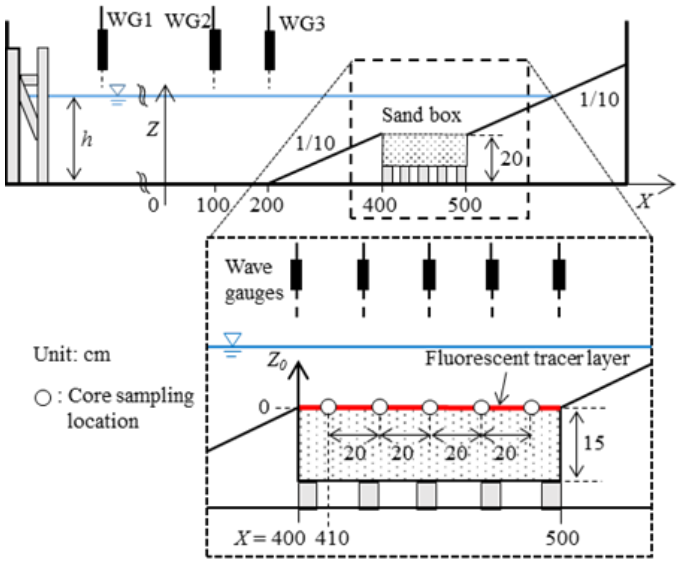

Fig. 4.1 Experimental set up of the 2D flume

At the beginning of each experiment, a thin layer of fluorescent sand tracers (120 g for Case 2, 4 and 240 g for Case 1, 3) were spread evenly on top of the flat sand bed. Noted here, for the each experiment, different color of the fluorescent sand tracer were used to distinguish the different trials.

$$\xi_b = \tan\beta \Big/ \sqrt{H_b / L_0} \quad \text{.....4.1}$$

Prior to the experiments, several waves were generated on an impermeable bed profile (Fig. 4.2) to decide on the wave heights and periods with different breaking styles that wave breaking point and wave impinging point were located inside the sand box. Table 3.2 lists the four wave conditions with different wave breaking parameters. The water depth, *h*, was 30 cm and 35 cm to attain different surf similarity parameters (ξ_b) which will emphasize the morphodynamic state of each wave condition. The equation 4.1 takes into account the wave breaking height (H_b), offshore wave length (L_0) and the bed slope ($\tan\beta$).

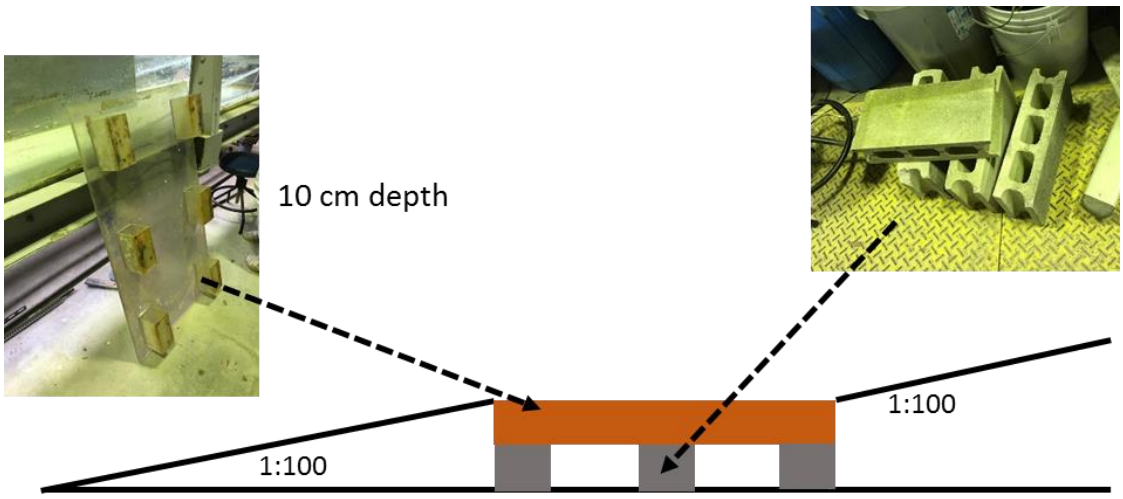

Fig. 4.2 An Impermeable bed made for wave trials before the experiments

The time duration for the each wave condition was set as 20 minutes. During each trial, the wave generator was stopped at 2, 5 and 20 minutes to conduct core sampling and survey the bed profile of sandbox area. The sand bed profile was observed every 10 cm at the middle of the flume width.

Table 4.1 The wave conditions of experiments

Case No.	H [cm]	T [s]	h [cm]	H_b [cm]	ξ_b
1	11.28	2.0	35.0	20.0	0.559
2	7.40	2.0	30.0	13.0	0.693
3	11.27	2.5	35.0	16.0	0.781
4	6.80	5.0	30.0	12.0	1.804

At the beginning of each experiment, fluorescent sand tracers were spread evenly on the top of the flat sand bed (120 g for Case 2, 4 and 240 g for Case 1, 3). Noted here, for each experiment, different colors of fluorescent sand tracers were used to distinguish the different trials.

At each time interval of the experiments, i.e. 2, 5 and 20 minutes, five core samples were collected from the sand bed with a distance interval of 20 cm (Fig. 4.1 of close up panel). The longshore direction of the sandbox area was divided into three sections, each with a width of 0.2 m. To avoid unexpected sediment mixing due to core sampling, each time step of the core sampling was conducted in different sections.

A PVC tube with a length of 20 cm and a diameter of 2.6 cm was used for the core sampling. After taking off a core, the bottom of the tube was sealed. The sampled tubes were then split into half using an automatic plastic cutter, and the cores were divided into every 1 cm layer (Fig. 4.3). The 1-cm-layer samples were air dried and taken to a dark room to count the number of fluorescent sand tracers using a UV light.

Fig. 4.3 The division of core sample layer process

Mixing depth has several definitions given by the previous researchers. For this research, the mixing depth was defined as the tracer depth from the bed surface at the time of core collection with a cut off value of 10 tracers. The value was based on a sample test conducted before the experiments. In the case of bed elevation higher than the initial bed level, i.e. accumulation, the mixing depth was measured from the initial level. The bed profile change for each case is given in Fig. 4.4. The least bed profile change was observed for Case 4 with the highest wave breaking parameter. Case 2 had a larger deposited sand with time which was accumulated in the center (Fig. 4.4 Case 2).

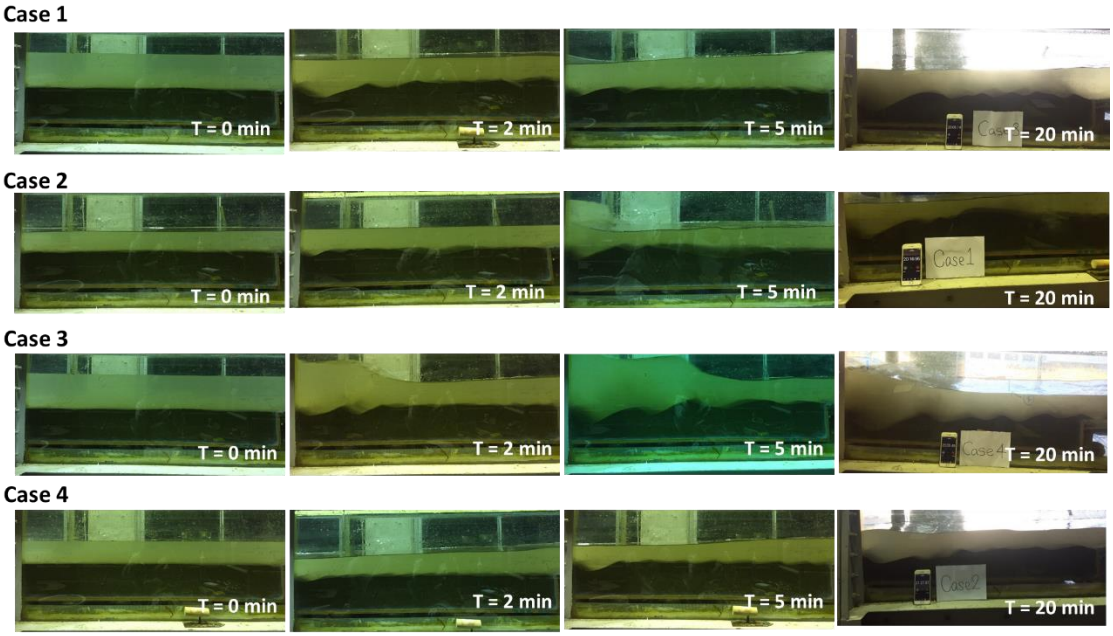

Fig. 4.4 The bed profile change of all four cases with time

The bed profile at 10 cm intervals were measured during the above mentioned t = 2, 5, 15 and 20 min before and after conducting the tracer experiments. The mixing of fluorescent tracer amounts were counted for each 1 cm thickness layer from each core sample at t = 2, 5 and 20 min (Fig. 4.5 and 4.6). During Case 1 and 2 where the wave breaking appears to have a plunging breaker style, have a scattered tracer patterns in depth while for the surge-plunge breaker cases a continuous fluorescent depths. The fluorescent tracer amounts along with the defined mixing depths for the interval t = 2 min of Case 2 and 4 have been separately shown in Fig. 4.7.

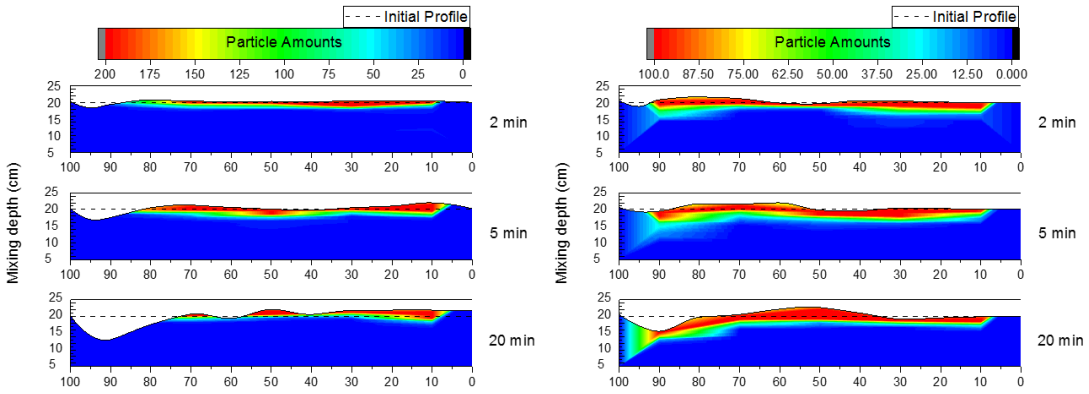

Fig. 4.5 The fluorescent tracer particle amounts counted along the bed profile for Case 1 and 2 under plunging breaker style.

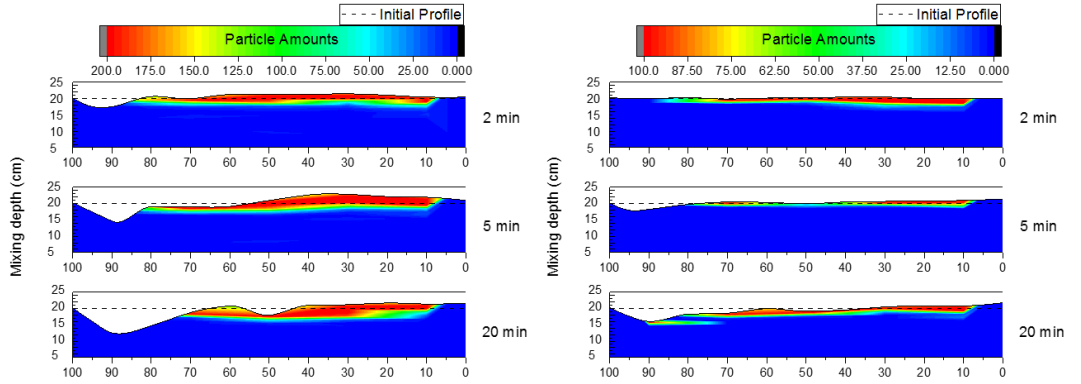

Fig. 4.6 The fluorescent tracer particle amounts counted along the bed profile for Case 3 and 4 under plunge-surging breaker style.

Fig. 4.7 shows the spatial distributions of fluorescent tracer amounts at $t = 2$ mins for Case 2 and 4. The contour colors indicate the number of tracers where warm and cold colors indicate a large and small number of the tracers, respectively. The vertical bars indicate the mixing depth at each cross-shore location. Moreover, the area from the wave breaking point to the impinging point is marked by a horizontal bar.

For both cases, a scour depth was noticed at the beginning of the sandbox. Since the figure shows the results of two minutes after the wave generation, the profiles were not changed drastically. For the Case 2 (plunging), the most of the intrusion of particles in depths has occurred in the beginning and at the end of flat bed where the maximum

mixing depths were at x = 410, 490 cm. in contrast, the mixing has decreased as in the center of the bed profile. In terms of Case 4 (plunge-surging), there were not many tracers within the scour area and a constant mixing depth was observed at all other locations.

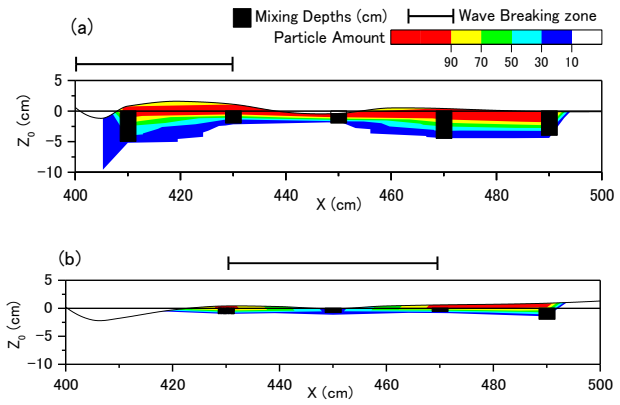

Fig. 4.7 Spatial distribution of fluorescent sand tracer amounts and mixing depths at t = 2 min, (a) Case 2 and (b) Case 4

Figure 4.8 shows the mixing depth patterns for the time intervals 2, 5 and 20 minutes along the sandbed of the four wave condition cases. Note that the mixing depths indicate the distance from the bed surface thus the origin varied depending on time and cross-shore location. The shaded area enclosed covers the observed region of wave breaking to the impinging point.

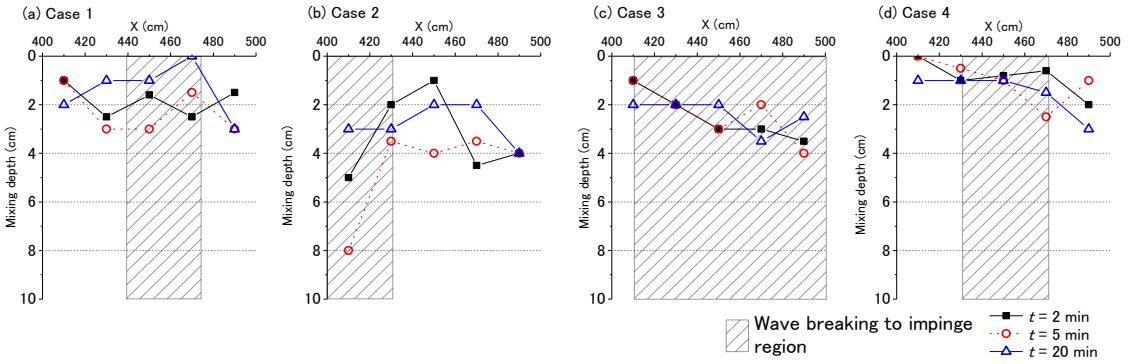

Fig. 4.8 Mixing depth patterns for the time intervals 2, 5 and 20 minutes along the sand bed, (a) Case 1, (b) Case 2, (c) Case 3 and (d) Case 4

For Case 1 and 2 (panels a and b, plunging) of each time interval, the spacial

distributions of mixing depths have varied between 0 to 3 cm and 1 to 8 cm, respectively. There is an irregular pattern of the location of maximum intrusion at each time intervals. It could be considered that the bed profile change will affect the mixing depth in time and space. However, for the 2 minutes distribution, both cases show two peaks.

In Cases 3 and 4 (panels c and d, plunge-surging), the mixing depths were within 4 cm where the values are minimum at the offshore side and constant or slightly deeper at the onshore locations. The same as the Case 1 and 2, the depths have fluctuated depends on time and space, the fluctuation bands are smaller.

In addition to the experimental work of this study, a comparison of investigated mixing depths in the flume study were done with the previous research work of Ciavola et al., 1997, Ferreira et al., 1998, Sunamura and Kraus, 1985, Anfuso et al., 2000 and 2003, Anfuso and Ruiz, 2004. The comparisons of wave breaking height (Fig. 4.9), surf scaling parameter, ε (eq. 4.2) in Fig. 4.10, wave breaking parameter (eq. 3.6) in Fig. 4.11 and $H_b \times$ bed slope (Fig. 4.12) with maximum mixing depths obtained by the experiments conducted by the authors mentioned and the current flume experiment were done.

$$\varepsilon = \frac{2\pi^2 H_b}{2gT^2 tan^2 \beta} \quad \text{.....4.2}$$

Investigation of mixing depths was conducted by previous authors using the collected field observation data at different sandy coasts and the mixing depths were compared with their particular wave breaking heights.

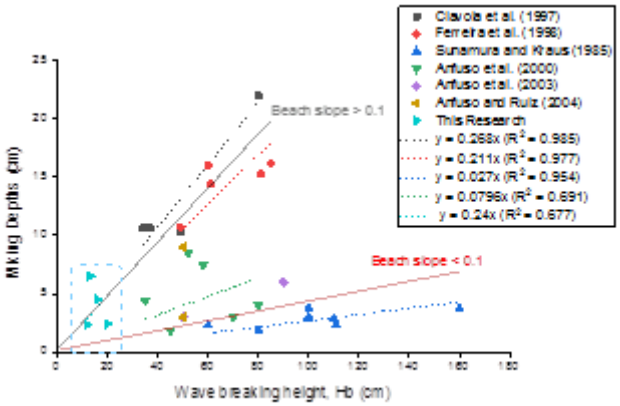

Fig. 4.9 The relationships of wave breaking height and mixing depths

Summarizing their results (Fig. 4.9), for the same wave height, higher mixing depths were observed for regions with a bed slope ≥ 1/10, while the mixing depths are lower for a mild beach slope of < 1/10. The increase turbulence created during wave breaking at a steeper slope might be contributing to the increase in mixing depths. The current study results were also compared along with the above-mentioned experiments to witness a similar trend as of steeper slopes of ≥ 1/10.

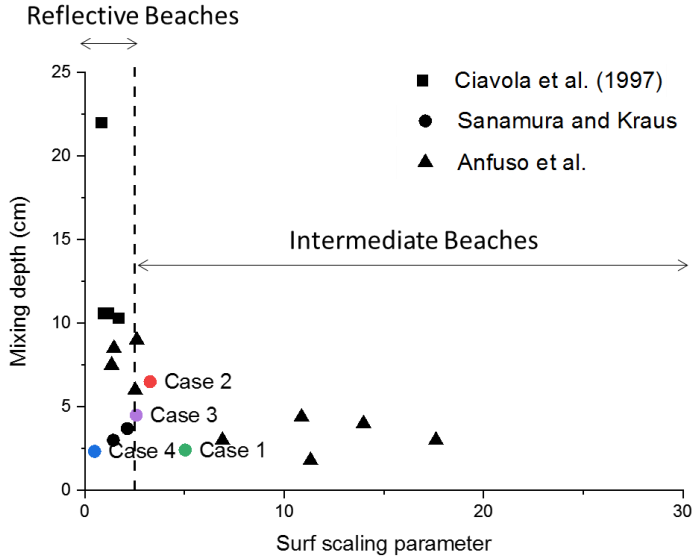

Fig. 4.10 The surf scaling coefficient and mixing depth relationship

Fig. 4.10 shows that the surf scaling parameter represents a reciprocal relationship to the mixing depths. When the beaches are reflective, the mixing depths would be higher and the intermediate to dissipative beaches have higher tendency to mix in depth. Similarly, the wave breaking parameters of research studies were compared in Fig. 4.11 to observe the trend of mixing depth when the breaking style changes. As of for spilling wave breaks, the mixing is smaller and increase in depth when the waves breaking style changes to plunging. However the trend has deviated for Case 4 of the flume experiments probably due to the difference in experiment environment/scale, grain size comparisons and etc.

Overall, the mixing has a strong correlation with the beachface slope which is included in both parameters of surf scaling and surf similarity which could be seen from Fig. 4.12

where the beachface slope × H_b was compared with mixing depths.

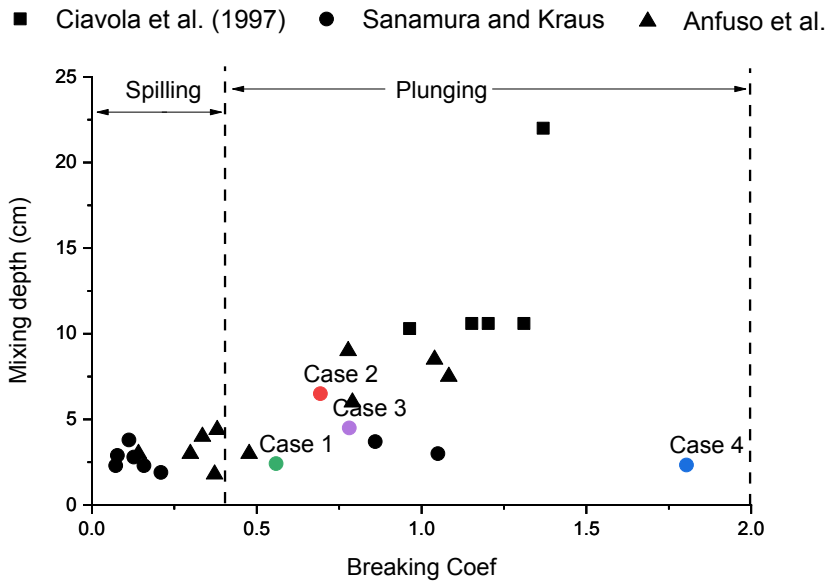

Fig. 4.11 The wave breaking coefficient/surf similarity parameter and mixing depth relationship

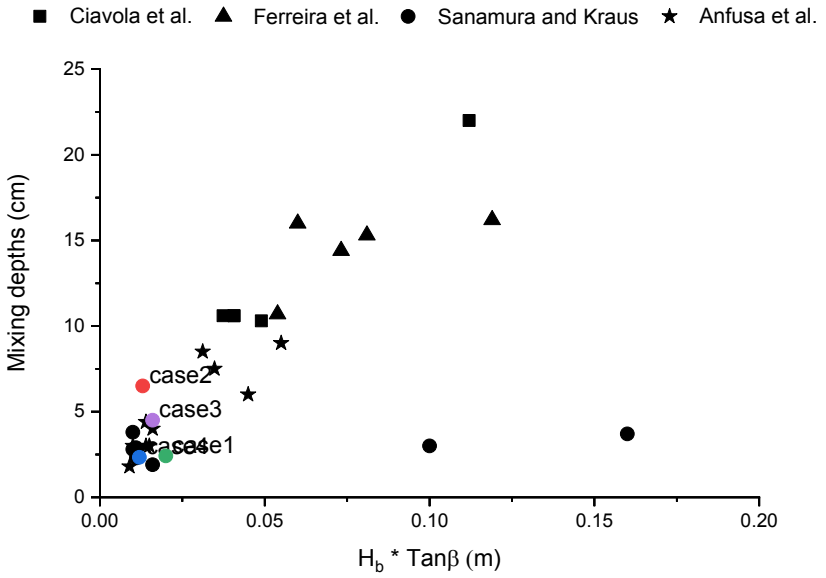

Fig. 4.12 The (H_b × tan β) and mixing depth relationship

4.2 LES Simulation

A three-dimensional Cartesian coordinate system (Fig. 4.13) was used to define the model domain. 800 grids in length, 24 in width and 52 in the vertical direction was adopted with a grid length of 1 cm with the origin at X and Z = 0 in Fig. 4.13. The calculation was started from the still water condition and the computational time step was 0.00064 s. This time step was determined by iteration until computational stability was achieved.

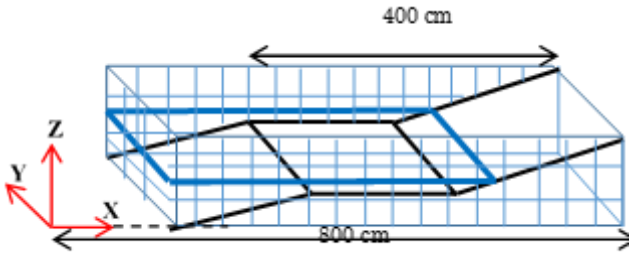

Fig. 4.13 The grid system of LES Model

For the calculation, 30 seconds were simulated with input values of the wave height, wave period and water depth given as in Table 4.2. The simulation results of water surface levels, wave heights, velocities and turbulence along the sand bed region (X = 400-500 cm, Y = 3-22 cm, Z = 23-50 cm) were extracted. The cross-shore and longshore velocities on the bottom cells are used to calculate the horizontal eddies. Note that the model did not calculate the profile change. The offshore boundary u_i velocities were calculated by finite amplitude theory, where the pressure and u_j were taken same values as one grid space inwards. The onshore boundary was considered to be steep wall/sea wall. The free surface was measured by a density function (Watanabe and Saeki, 1997) and the bottom/lateral boundaries were considered as Neumann Boundaries where further details could be obtained by Niroshinie (2014).

4.3 LES Model Verification

The calculated water surface elevations and velocity fields were verified by the wave height observed records and the fluid velocities analyzed by a Particle Image Velocimetry method (PIV), respectively.

4.3.1 Wave Height Verifications

Initially 6 wave gauges were setup in the flume to measure the wave height distribution along the flume length (Appendix B). After fixing the permeable sand box and while the experiments were conducted, 8 wave gauges were setup, and the wave heights were recorded (Fig. 4.14). Five wave gauges along the interested area of the flat bed profile was fixed to measure the wave heights as seen in Fig. 4.14.

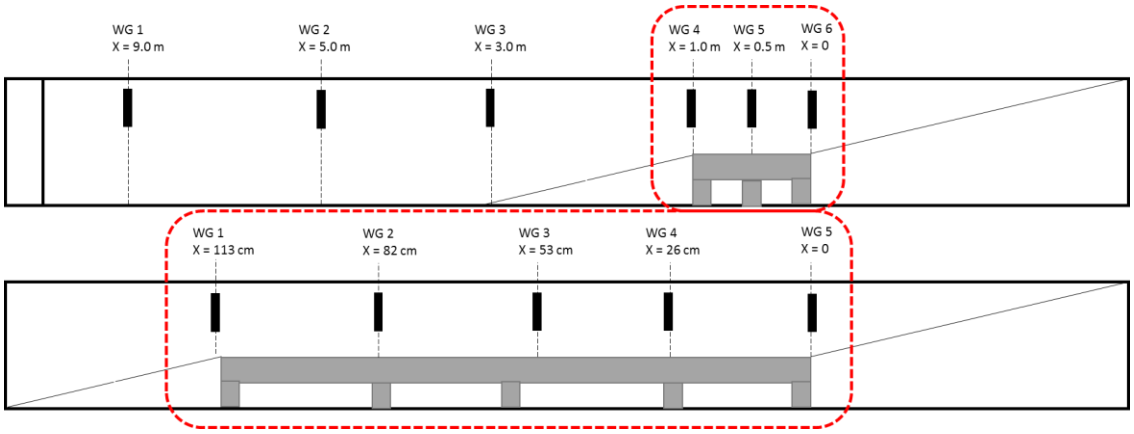

Fig. 4.14 The wave gauge setup for the flume test experiment.

The simulated wave heights from LES model at above mentioned locations of WG1, WG2, WG3, WG4, WG5 (Fig. 4.14) for all wave cases were compared with the recorded values for verification purposes of the model (Appendix C). The calculated and measured water elevations only for Case 1 at X = 100 cm, still water area, and 400 cm, where the maximum wave heights were recorded, are shown in Fig. 4.15. The model seems to slightly underestimate the wave height values as the experimental values. However the calculated values give an overall better representation of the experiment with a standard error (SE) of 0.057 (X = 100 cm) and 0.045 (X = 400 cm).

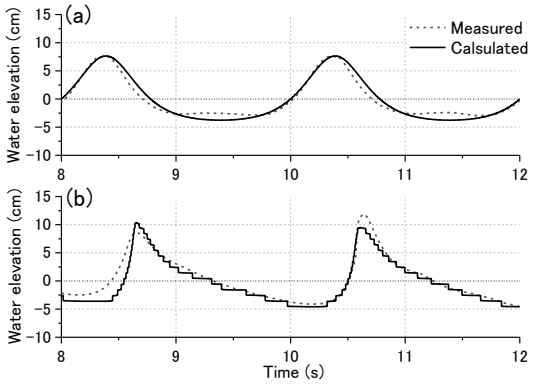

Fig. 4.15 Numerical and the experimental results of wave heights of Case 1, (a) X = 100 cm and (b) X =400 cm

The Fig. 4.16 shows the wave gauges used during the experiments to measure the wave heights and for the results of all wave gauge locations and model simulated wave height comparisons to them can be found in Appendix C.

Fig. 4.16 Wave gauges stationed along the flat bed profile for wave height measurements during experiments

4.3.2 Particle Image Velocimetry Method

The PIV method was adopted for the measurements of fluid velocities from each wave

condition. Consecutive images taken during the propagation of the wave were analyzed using the PIV to get the velocity of the flow field. This was done by seeding some particles which are strictly following the water flow, and analyzing the images to see the displacement of particles. From the displacement of particles in a given time slot (frame speed of the camera), the velocity of the flow field is obtained. A high speed camera for the film images, a laser to track the particles, fine tracer particles to track the flow streamline movement are the main sources for the PIV method (Fig. 4.17).

(a) (b) (c)

Fig. 4.17 The PIV setup equipments (a) The laser instrument, (b) High speed CCD camera and (d) The fine tracer particles used to measure the velocity fields

For the velocity verifications, the region of interest (X = 400-500 cm) were separated to five locations along the flatbed. The experiment setup for the PIV method using the equipment mentioned in Fig. 4.17 are given in Fig. 4.18. The velocity fields were captured by a high-speed CCD camera with a frame rate of 100 fps. At each area, 15.0×15.0 cm^2 was covered by one frame and due to the effect of wave breaking in the locations, only the bottom area of 15.0×5.0 cm^2 was used for velocity verification purposes. The Matlab image processing toolbox and the PIVlab program (Thielicke and Stamhuis, 2014) were used for the velocity calculations.

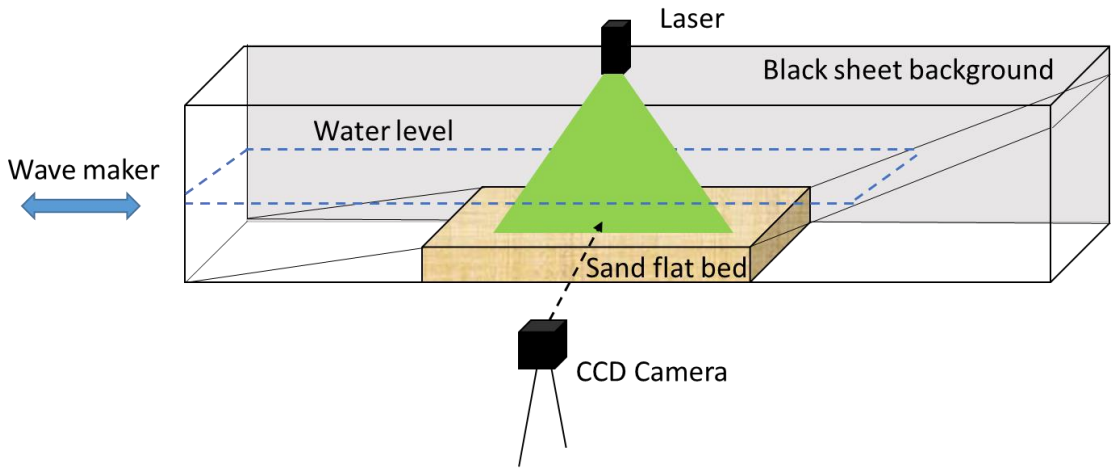

Fig. 4.18 The PIV experimental setup

The frames were analyzed using the PIV toolbox using the cross-correlation method and the velocity magnitudes in x (u) and y (v) directions were extracted. The Resultant velocity magnitude = $\sqrt{u^2 + v^2}$ and the velocity direction in degrees by = $\tan^{-1}(v/u)$ is further calculated using the extracted images after matching the wave phases of LES model results.

The velocity magnitude and vector diagram of one of the selected wave phases is given in Fig. 4.19 for Case 1. The numerical and experimental cross-shore velocity magnitudes for Case 1 at four wave phases; t/T = 0.0, 0.22, 0.44 and 0.66 are shown in Fig. 4.20.

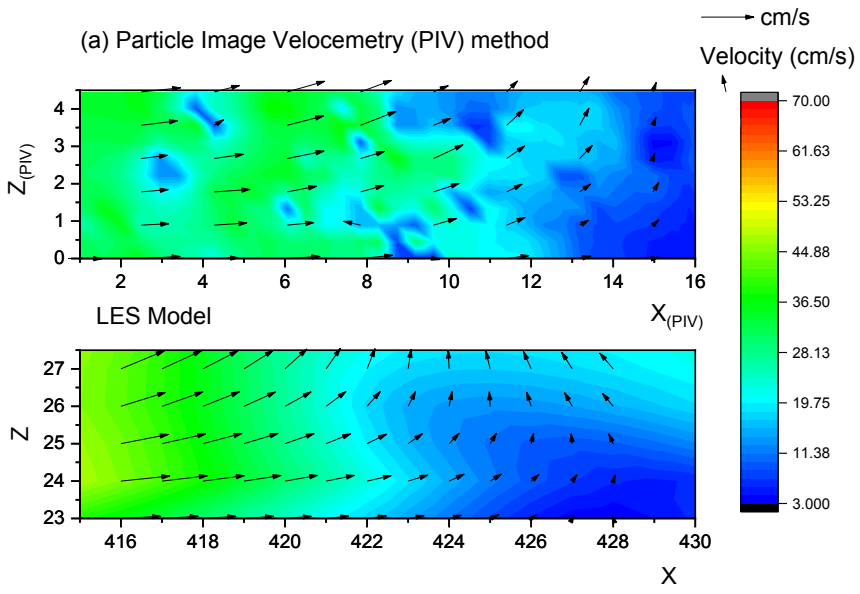

Fig. 4.19 The experimental and modeled velocity magnitude and vector diagrams for Case 1 frame location x = 415-430 cm during a selected wave phase.

The figure shows the instantaneous cross-shore velocity magnitude above the sand bed, X = 428 cm. Although discrepancies observed in velocities for t/T = 0.22, overall vertical profile and velocity magnitude show agreement. Due to the less inconsistency in wave height verifications and fewer discrepancies in most of the wave phases, the simulation results were used for the discussion.

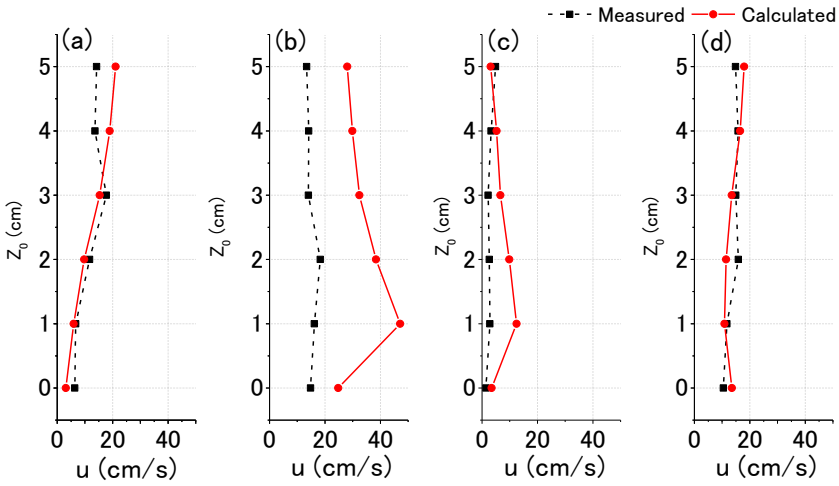

Fig. 4.20 Vertical distributions of cross-shore velocity magnitude at X = 428 cm for Case 1, (a) t/T = 0.0, (b) t/T = 0.22, (c) t/T = 0.44 and (d) t/T = 0.66

4.4 LES Results and Discussion

From the LES model, the x-y horizontal plane velocities, x-z vertical plane velocities, wave heights along the bed profile were generated. From the velocity components, the cross-shore vertical and horizontal eddies were calculated. The results at each instant wave phase for the four cases were later compared with the mixing depths investigated along the bed profile. The results of cross-shore horizontal and vertical plane velocities are given in Appendix C along with the wave height comparisons.

The cross-shore fluid velocities in x ($U_{i,j,k}$), y ($V_{i,j,k}$), z ($W_{i,j,k}$) directions, modeled by LES are further used to calculate cross-shore current velocities in both horizontal and vertical planes. The horizontal eddies ($UV_{i,j,k}$) and vertical eddies ($UW_{i,j,k}$) are further

calculated (eq. 4.3 and eq. 4.4) to compare with the spatial mixing depth variations in space under four different wave conditions.

$$\mathrm{UV(i,j,k)} = \left(\frac{U(i,j,k)-U(i,j-1,k)}{DY} - \frac{V(i,j,k)-V(i-1,j,k)}{DX}\right) \quad \text{.....4.3}$$

$$\mathrm{UW(i,j,k)} = \left(\frac{U(i,j,k)-U(i,j-1,k)}{DY} - \frac{W(i,j,k)-W(i-1,j,k)}{DZ}\right) \quad \text{.....4.4}$$

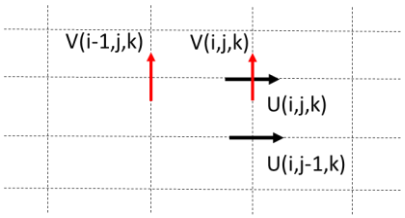

The instantaneous velocities at eight phases and ten wave phases were extracted from the LES results for Case 1, 2 and 3, 4, respectively, and the spatial distribution of the bottom horizontal and vertical eddies were calculated.

Figure 4.21a and 4.21b show the spatial distributions of the bottom horizontal eddy at three different wave phases during one wave cycle of Case 2 (plunging) and 4 (plunging-surging), respectively. The figures indicate the maximum eddy value along the longshore direction of the flume for each cross-shore location along with the water surface elevations. The left axis represents the eddy value and the right axis with the water surface elevation.

The bottom horizontal eddies for Case 2 (Fig. 4.21a) show significant peaks in phase t/T = 0.0 at the location x = 470 cm and in phase t/T = 0.44 at the offshore end of the investigated area. Nonetheless, the eddies are almost constant throughout the bed profile for Case 4 (Fig. 4.21b). The magnitudes of eddies for Case 4 are comparatively lower than the Case 2. It could consider that the difference of water levels and breaking patterns will affect the results.

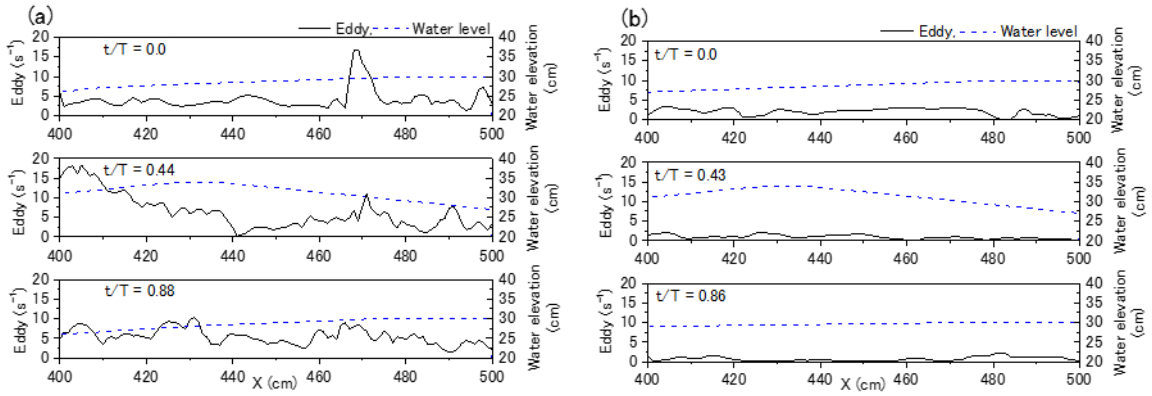

Fig. 4.21 Spatial distributions of bottom horizontal eddy and water elevation at three wave phases, (a) Case 2 and (b) Case 4

At last, the calculated bottom horizontal eddies and the observed mixing depths were compared. The spatial distributions of maximum bottom horizontal eddies out of all the wave phases and the observed mixing depth of each time interval for all the cases are shown in Fig. 4.22. The magnitude of bottom eddy will change depending on the bed profile. However, since the model could not calculate the profile change, the discussion is mainly focused on the correlation between bottom eddies and the observed mixing results of 2 minutes (solid lines).

The spatial distribution of maximum eddy of Case 1 shows that there is a depression in the middle of the flatbed, x = 450 cm, and peaks in the beginning and the end of the profile. For the Case 2, as discussed in Fig. 4.21, the peaks appear at the offshore end of the sandbox and the near the onshore end. In contrast, the Cases 3 and 4 have no peak and the value shows nearly the constant through the cross-shore direction.

For the Case 1 and 2, plunging breaker type, of mixing depth, although the magnitude of the mixing depths is not correlated with the eddy distribution, both cases also show peaks at 2 minutes. In Case 1 the 2 minutes mixing depths have maximums at x = 430 and 470 cm where the depths is decreased in the center following the trend of eddy changes. The eddy and mixing depth have a mutual relationship for Case 2 of t = 2 minutes depth trends. The mixing depths have increased at the beginning of the bed (x = 410 cm) and again at x = 470 cm which is similar to eddy variation along the bed.

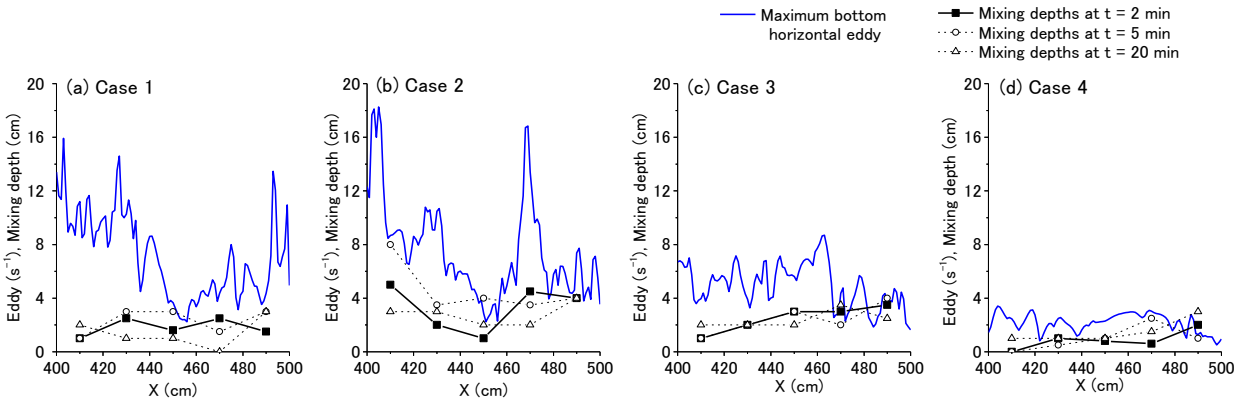

Fig. 4.22 Spatial distributions of maximum bottom horizontal eddies and mixing depths of 2, 5 and 20 minutes, (a) Case 1, (b) Case 2, (c) Case 3 and (d) Case 4

The 2 minutes mixing depths for Case 3 and 4, plunging-surging breaker type, follows a constant trend which is similar to the eddies along the profile. There is no significant peak of depression of the mixing depths other than the temporal fluctuations which cannot be considered due to the profile changes which was not included in eddy calculations.

Overall the plunging breakers have created larger eddy distributions compared with the plunge-surge breakers with several increments at the locations of wave break and plunge points. The initial mixing of sediments along the bed profile has followed the trend of the eddies at the bottom plane signifying the effect of breaker style and eddy on bed surface layer.

Apart from the bottom plane eddies, the effect of vertical plane eddies were also analyzed using the equation 3.9. The results were similar to the horizontal plane eddies, but larger in value as shown in Fig. 4.23 for Case 2. The figure compares the vertical and bottom maximum eddy distribution along the flume bed. Eventhough the trend in eddies are similar, the values are largely different. The vertical plane eddies during one wave cycle is given in Fig. 4.24 where an extra peak in eddies appear at the surface water in vertical plane as also can be seen from Fig. 4.24 at x = 480 - 500 m.

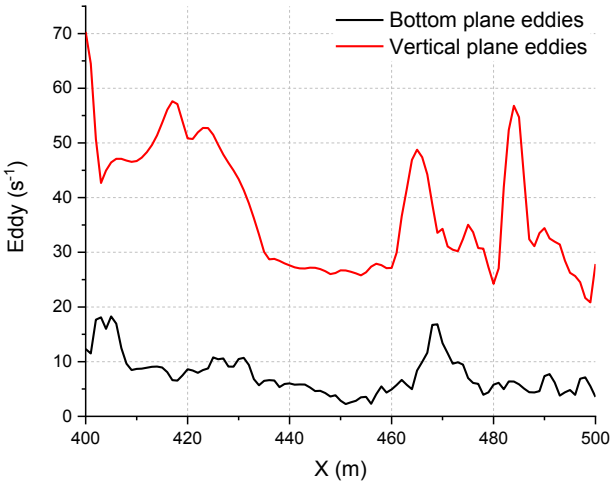

Fig. 4.23 The cross-shore maximum eddies in the bottom plane and vertical planes for Case 2

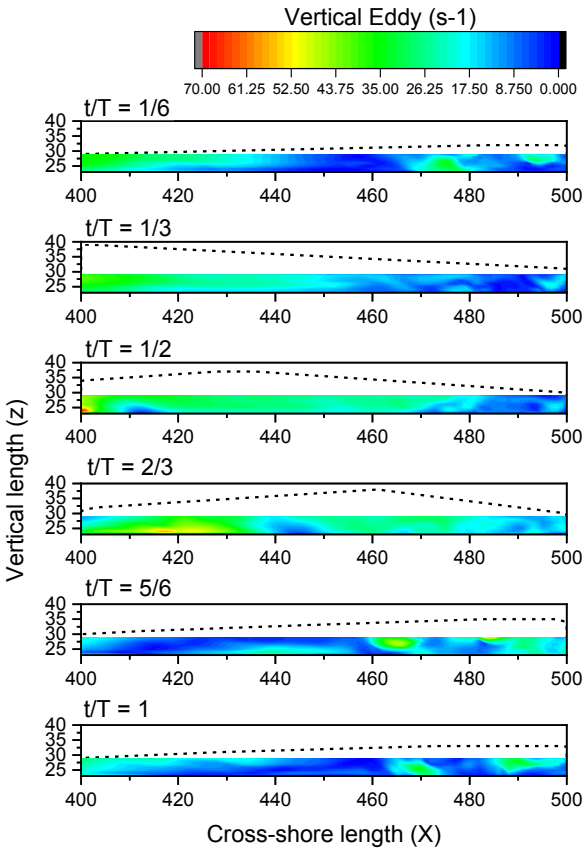

Fig. 4.24 The cross-shore vertical plane eddy distribution for Case 2 within a wave cycle

4.5 Experiment Conclusions

The wave conditions of two breaking styles, plunging and plunging-surging, were generated in a 2D flume to investigate the spatial and temporal mixing depths in the wave breaking region. In the experiment, fluorescent sand tracers were used to find the depth of mixing. A 1-m-length of the flat sand bed was installed in the middle of the slope, and the cores were sampled at 2, 5 and 20 minutes time intervals for every 20 cm in the investigate section. Each core of fluorescent sand tracers was manually counted every 1 cm, and find the mixing depth for each time and space. The hydrodynamic fields were simulated using the LES approach to assess the three-dimensional velocities, eddies, and turbulence during the wave cases.

The cases with lower breaking parameters (plunging) show a similar trend in maximum bottom horizontal eddies where several peaks in eddies were noted. As the surf similarity parameter gets larger (plunging-surging), the maximum bottom horizontal eddies were constant through the breaking area within a wave cycle. For the plunging breaker type of mixing depth, although the magnitude of the mixing depths is not correlated, the spatial distribution has correlation with the bottom horizontal eddy. The plunging-surging breaker type of the results show that weak bottom horizontal eddy and constant mixing depth in space.

5 SEDIMENT MIXING AND SEDIMENT PROPERTIES

In this chapter, field experiments of sediment mixing and sediment diameter analysis which was conducted at Hazaki Oceanographical Research Station (HORS) in Japan is being discussed. The experiments were conducted in the years from 2014 – 2017 during a certain periods of times as mentioned further in the paper. The initial objective of these studies were to investigate the sediment mixing in the surf zone within a field environment, but the studies were further extended by myself to analyse the sediment properties and the heterogeneous behavior in the nearshore bed profile. The experiments were conducted and inspected by several Masters and Undergraduate students.

5.1 Sediment Properties of Hasaki, Ibaraki, Japan

The sediment mixing in the surf zone was investigated by many authors in the past in order to investigate the effect of wave characteristics on bed profile evolution. Generally these experiments were conducted under normal wave conditions within a tidal cycle. The current experiments were conducted to investigate the sediment mixing under extreme wave conditions.

The spatial and in-depth variation of sediment textural parameters, grain size, sorting, and skewness of a sandy beach are also been discussed. The data were collected in 2014, 2015, and 2016 during high and mild wave conditions. The analysis of sediment parameters will further elevate the understanding of the sediment transport direction, fore- and backshore slope, infiltration and exfiltration capabilities (e.g., McLean and Kirk, 1969; Sunamura, 1984; Komar, 1998), and environmental and dredging studies (Oyedotun, 2016)

The field observations were conducted along a 427 m long pier perpendicular to the shore, which was constructed for research purposes at the Hazaki Oceanographical Research Station (HORS), facing the Pacific Ocean, owned by the Port and Airport Research Institute (Fig. 5.1a). The cross-shore distance along the pier is defined relative to the HORS reference point and a positive seaward direction is used. The beach topography was measured once a week at 5 m intervals. The high, mean, and low water levels based on the datum level (D.L.) at the port of Hasaki (Tokyo Peil: 0.687 m) are 1.252 m, 0.651 m, and -0.196 m, respectively. The Hasaki Coast comprises sandy beach with almost constant topographical change in the longshore direction (Kuriyama, 2002)

as seen by Figure 5.1b. The beach experiences high waves during the winter season and is relatively calm during summer (Suzuki and Kuriyama, 2006).

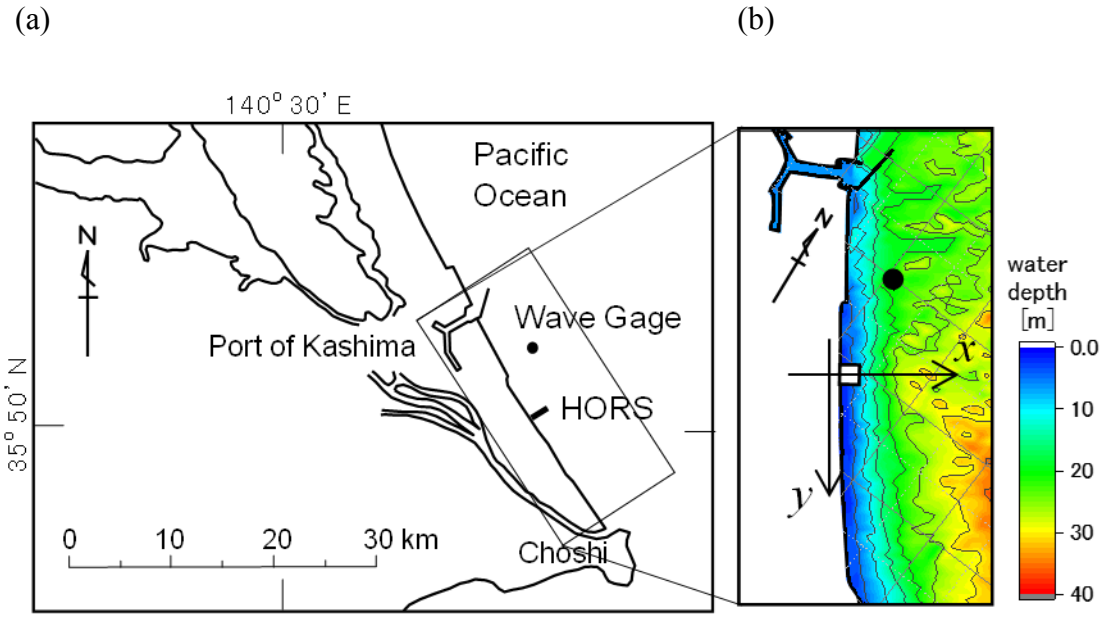

Fig. 5.1 Location of the (a) Hasaki Oceanographical Research Station (HORS) and (b) The bathymetric map

Prior to 2006, Hasaki Coast formed a berm near the shoreline during calm wave conditions, which is eroded due to the long-period wave run-ups. This pattern drastically changed in October 2006 due to large waves breaking near the shoreline, creating a continuing berm with a steep slope at the beach face (Yanagishima, 2016). This event has altered the cross-shore profile and created a bar on the offshore side, which carries coarser sand in trough areas and finer material in crests. The sediment movement and mixing have a direct impact due to this alteration.

5.1.1 Field Experiment Setup

The field experiments were conducted along the pier of HORS during four times in 2014, 2015, 2016 and 2017. The former two years, the experiments were during the winter season, while the latter were during summer. The wave conditions of each experiment period are given from Fig. 5.2 and 5.3.

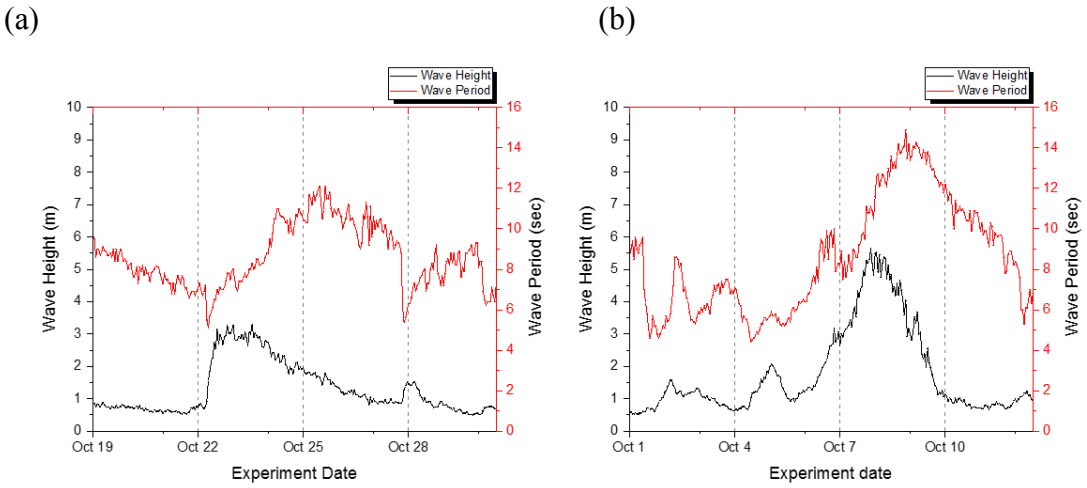

Fig. 5.2 The significant wave height and wave period in the offshore for experiment durations in (a) 2014 and (b) 2015 during winter.

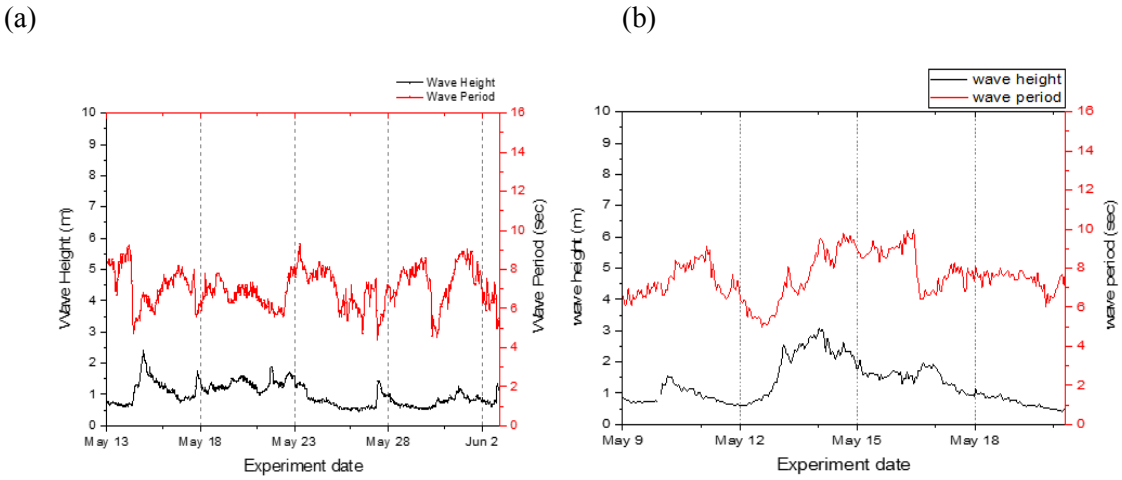

Fig. 5.3 The significant wave height and wave period in the offshore for experiment durations in (a) 2016 and (b) 2017 during summer.

Continuous wave data collected near the pier of Hasaki are available for every year, 23.4 m offshore the Port of Kashima. The recorded waves are available for public use on the website of the Nationwide Ocean Wave Information Network for Ports and Harbors (NOWPHAS). The experiments were conducted during the time periods which is mentioned in Table 5.1. The characteristics of the waves and profile change is given in the table as well.

Table 5.1 The wave condition table for the experiment periods

Exp no.	Experiment Period	Avg Hs (m)	Avg Ts (s)
1	(2014) 10/18 – 10/30	1.26	8.5
2	(2015) 10/01 – 10/12	1.72	8.5
3	(2016) 05/12 – 05/24	1.31	7.2
	(2016) 05/24 – 06/02	0.97	7.2
4	(2017) 05/09 – 05/21	1.26	7.6

Note :

H_s – Offshore significant wave height

T_s – Offshore significant wave period

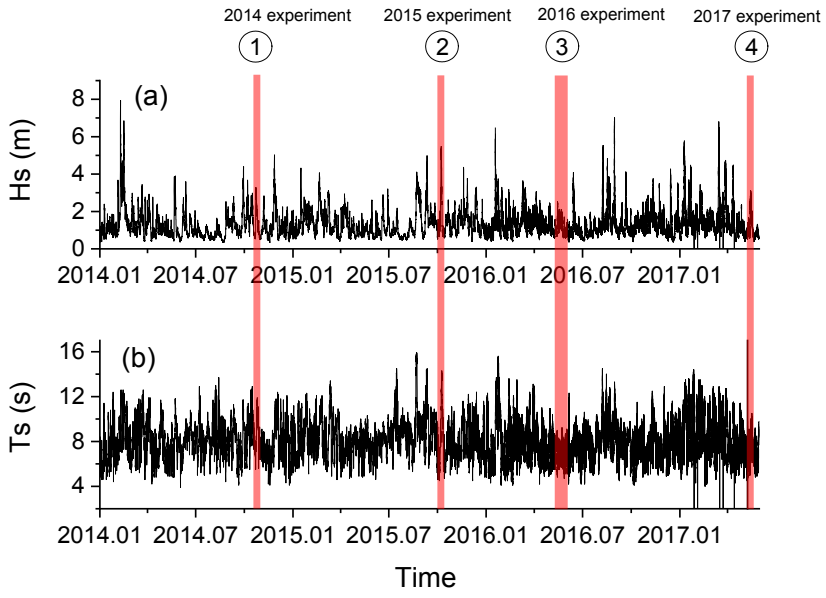

Fig. 5.4 Time series data for the offshore wave, (a) significant wave height, (b) significant wave period. The vertical lines indicate the time of the field observations.

A traditional core sampling method was used in the current study to obtain the particle properties and sediment mixing in the surf zone. Fig. 5.4 shows the offshore H_s and T_s variation for the years 2014 – 2017. The significant wave heights generally varied

between 0.5 to 3.0 m in 2014, with a significant wave period ranging from 5 to 12 s. At this coast, relatively high waves could be noticed during the period from October to February. The 2014 core sample collection was conducted during this period when high waves hit the Hasaki Coast on October 30, 2014. The wave climate in 2015 shows a similar trend and range of waves approaching the coast as the previous year. However, the high waves with a higher wave period arrived much earlier, that is, in mid-August. The core samples were collected on October 12 after three high wave events. In 2016, the core sample days were shifted to the period in which the coast experienced mild wave conditions with lower offshore heights and lower wave periods ranging from 6 to 9 s. Two sets of core samples were conducted a few days apart on May 24 and June 2 under these mild wave conditions. The wave conditions in 2017 were somewhat similar to the year 2014 where a mild storm hit the coast during the experiment period.

The experiments for sediment mixing was based on a tracer method where coloured fluorescent tracer particles were placed on previously decided locations along the bed profile. After several days, core sample from the swash zone to the offshore end of the surf zone was collected. The Fig. 5.5 shows the HORS pier where the cores were collected from and the core sample collection procedures. A clear, 1.3 m long PVC pipe with 5.2 cm inner and 6 cm outer diameter was inserted at each location into the sea bed using a hammer as seen in Fig. 5.5c (2014 and 2015) and vibration hummer as seen in Fig. 5.5b (2016 and 2017). The colours of tracer particles, the initial locations and the core sampling locations are given under each years' experiment;

(a) (b) (c) (d)

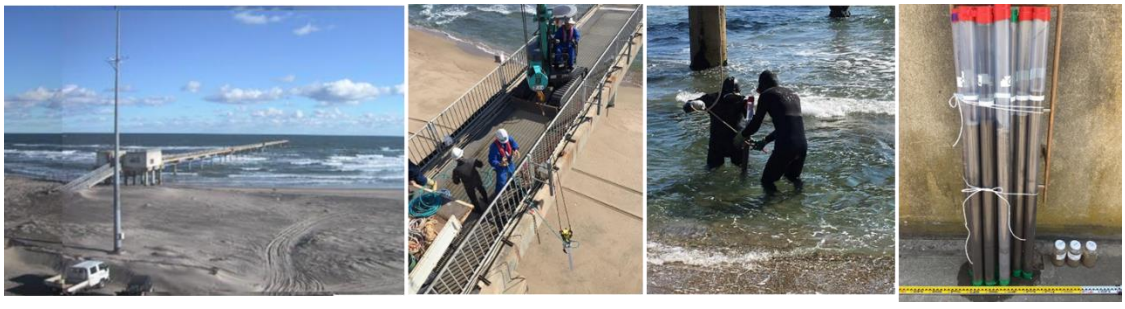

Fig. 5.5 Some of the experiment photos from (a) Hasaki HORS pier, (b) Descending of cores using a hydraulic vibration hummer, (c) Divers inserting cores to the ground using a hammer and (d) Collected core samples.

2014 Experiment (2014/10/19 – 2014/10/30)

Five colours were placed at the locations of x = 65 m (pink), 115 m (yellow), 180 m (blue), 240 m (green), 290 m (red) initially on 2014/10/19. The bed profile was measured during the experiment period at 20 m length intervals using a weighted rod. 8 core samples were taken from the area concerned (Fig. 5.6)

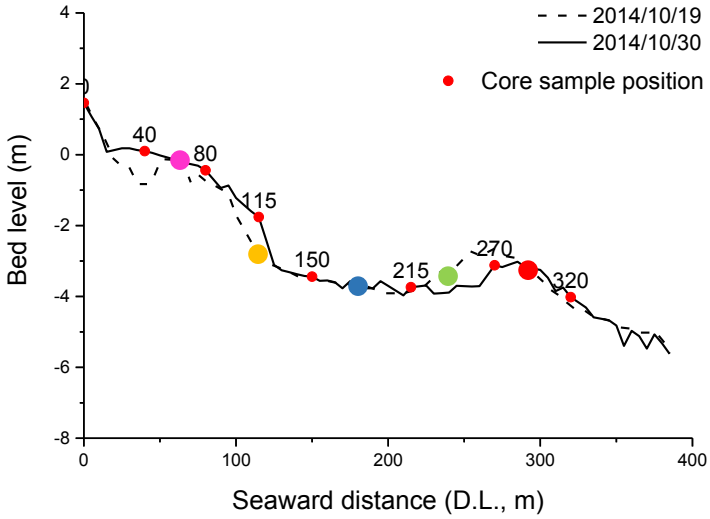

Fig. 5.6 The bed profile change, the core locations and tracer positions for experiment in 2014

2015 Experiment (2015/10/01 – 2015/10/12)

Only two colours were placed at the locations of x = 140 m (yellow), 290 m (red) initially on 2015/10/01. The bed profile was measured during the experiment period at 5 m length intervals using a weighted rod. 8 core samples were taken from the area concerned (Fig. 5.7).

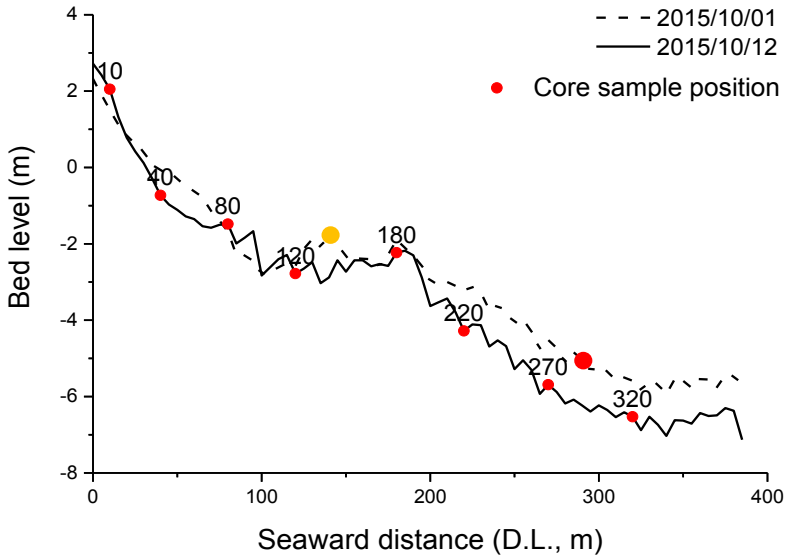

Fig. 5.7 The bed profile change, the core locations and tracer positions for experiment in 2015

2016 Experiments (2016/05/13 – 2016/06/02)

Two core samplings were done during the period mentioned for 2016. Initially five tracers were placed on 2016/05/13 on the bed profile at locations x = 70 m (pink), 120 m (yellow), 170 m (blue), 220 m (green), 280 m (red). The core samples at 8 different locations along the bed profile were collected on two days ; 2016/05/24 (Fig. 5.8a) and 2016/06/02 (Fig. 5.8b) respectively. The Fig. 5.8 shows both of the experiment profiles for 2016 during the mild beach conditions. The core sample locations of each experiment on 2016 were not changed.

(a)

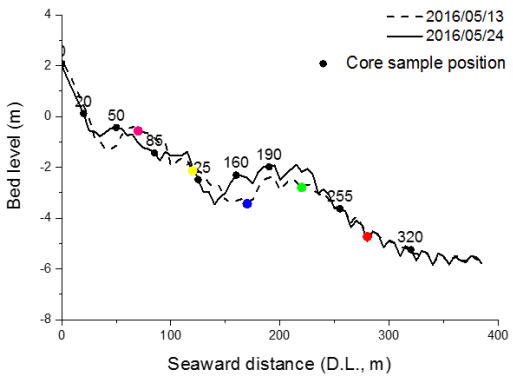

(b)

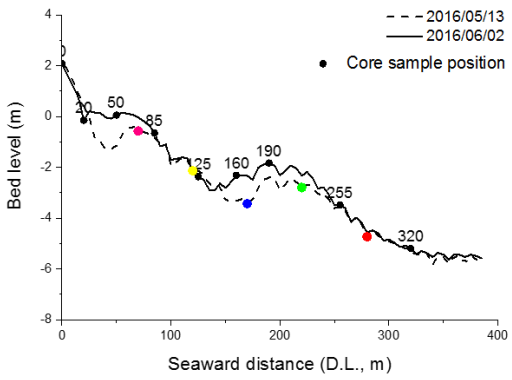

Fig. 5.8 The bed profile change, the core locations and tracer positions for experiment in 2016

2017 Experiments (2017/05/09 – 2017/05/21)

In 2017, 9 core samples were collected starting from 0 – 380 m along the cross-shore. Initially 3 colours of tracers, Green, yellow and red were placed at 3 locations as given in Fig. 5.9 The profile was eroded in most of the locations.

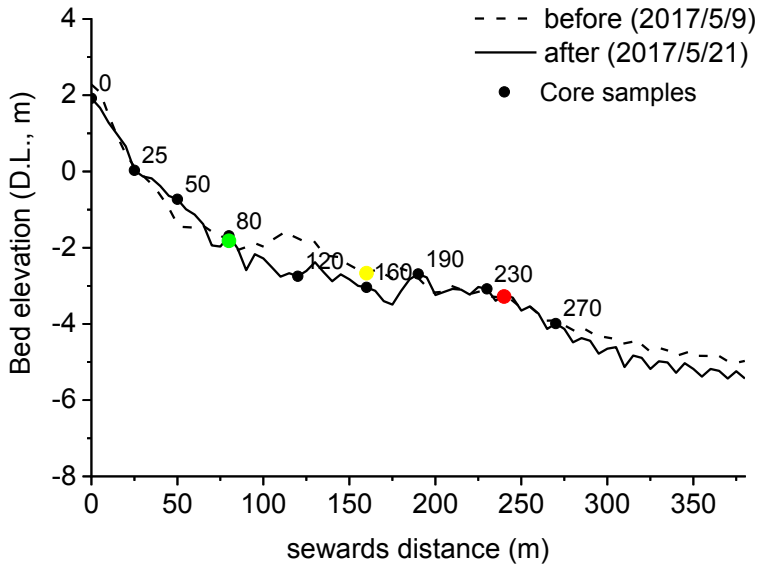

Fig. 5.9 The bed profile change, the core locations and tracer positions for experiment in 2016

Each core sample was separated into layers of 5 cm (2014,2016 and 2017) and 2.5 cm (2015) for the analysis of the particle sizes D_{25}, D_{50}, and D_{75} (in mm) and tracer amounts in each separated layer. The core samples were initially scanned with an X-ray Computed Tomography (CT) system to understand the sand accumulation. The results of the 2014 observations were published by Suzuki et al. (2017). A summary of all the core sample locations and their sample heights are given in Table 5.2. Comparatively longer cores were obtained during 2016. The shortest samples were obtained in 2015 due to the sediment diameter of the sea bed and the use of a different core sampling method.

Table 5.2 Core sample details for the observations conducted in 2014, 2015, and 2016

2014/10/30		2015/10/12		2016/5/24		2016/6/2		2017/5/21	
x (m)	Core length (cm)	x (m)	Core length (cm)	x (m)	Core length (cm)	x (m)	Core length (cm)	x (m)	Core length (cm)
0	77	10	65	0	69	0	87.4	0	96.5
40	40	40	47	20	40.5	20	97	25	69.5
80	50	80	24	50	113.7	50	117.2	50	104.5
150	52	120	30	85	92.5	85	96	80	105
215	30	170	27	125	111.7	125	90.3	120	105.5
270	46	220	28	160	104.8	160	92.1	160	100
320	51	270	26	190	92.2	190	105.6	190	83
		320	8	255	103.5	255	92.6	230	103
				320	114	320	93.4	270	99.5

5.1.2 Sediment Diameter Pattern in the Surf Zone of Hasaki

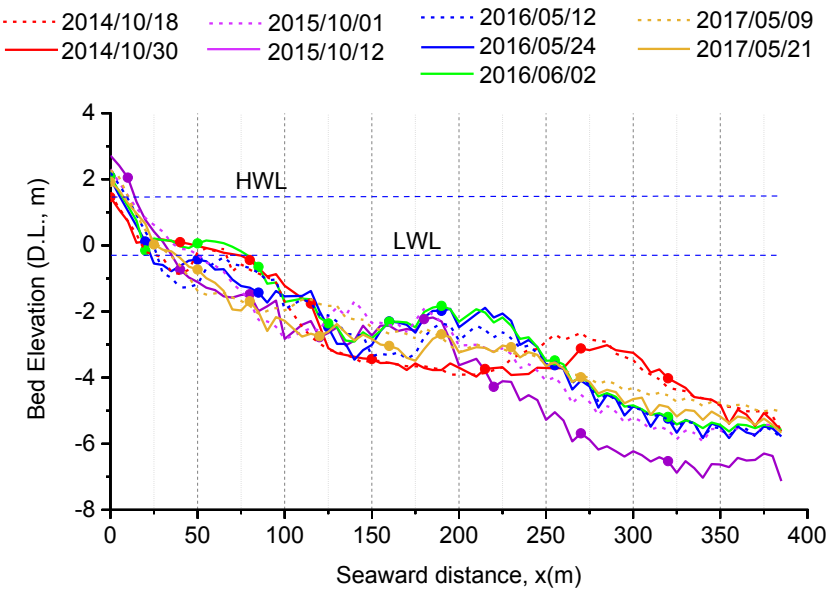

Fig. 5.10 Cross-shore profile variation and core sample positions (dotted locations) during the observations

The diameter sizes of D_{50}, D_{25} and D_{75} were plotted along the depth of each core sample from 2014 to 2017 experiment results. Fig. 5.10 shows the bed profile change and the core sample locations of the years. The beach profiles in Figure 5.10 show a steep and stagnant beach slope near the shoreline and offshore bar formations that were created after 2006, as mentioned in Yanagishima (2016). In addition to the diameters, the sorting and skewness along depth was calculated using the equation mentioned in Chapter 2.

2014 Experiment Observations

The October 2014 observation was conducted during a period with relatively high waves. The offshore bar appears around at offshore location (x = 275 m). The trough width is longer (x = 150–250 m) than that of other observation days (Fig. 5.10). The longest sediment core sample (maximum length) was collected near the shoreline position (x = 0 m) and the shortest one (minimum length) at x = 40 m (Table 5.2).

The in-depth and spatial variation of D_{25}, D_{50}, and D_{75} are shown in Figure 5.11 as of measured from the core sample surface. Based on the figure, the median diameter of the entire region is below 2 mm and above 0.1 mm, which represents a fine and medium sand bed composition according to the ASTM standards. The gap between the percentile diameter values increased at locations x = 0, 80 and 150 m. The D_{50} values also notably increase at these locations. The percentile diameters at other locations in depth remain almost equivalent.

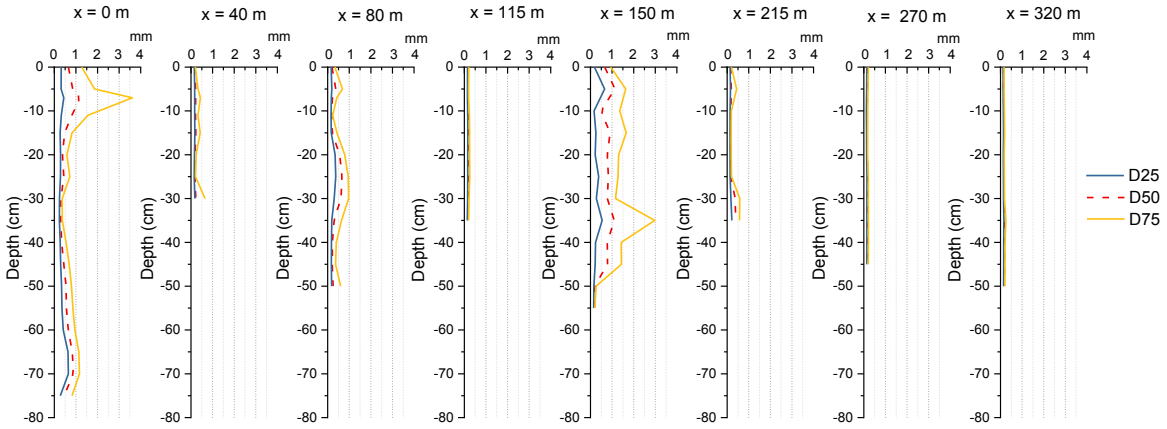

Fig. 5.11 In-depth and spatial variation of D_{25}, D_{50}, and D_{75} for the observation conducted in 2014

2015 Experiment Observations

The core samples were taken on October 12, 2015, after the beach experienced two storms and higher waves than that during other observation years. The bed profile eroded from the shoreline to the offshore due to the high waves (Fig. 5.10). The offshore bar is not visible in the study region.

The median diameter of all the sample locations ranged from fine and medium sand, similar to the previous year (Fig. 5.12). However, several sample locations with coarse sand (4.75 mm > D_{75} > 2 mm) exist based on the swash and offshore sample plots. The gaps between the percentile diameters also increase at these locations. Higher gaps are noted at x = 10, 40, 80, 215, 270, and 320 m. The sample lengths decreases in the offshore direction due to difficulties with the core insertion into the ground. The divers claimed that the offshore sampling failed due to the existence of coarser material.

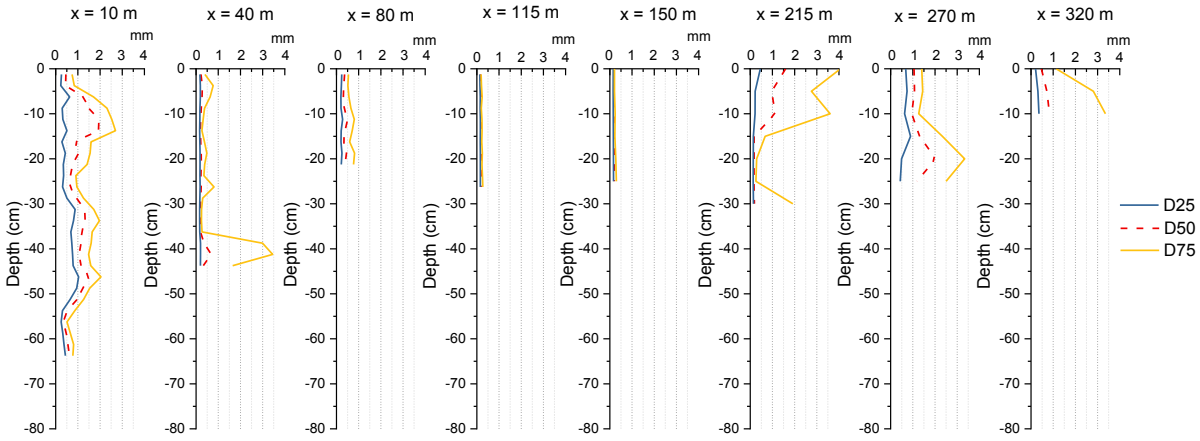

Fig. 5.12 In-depth and spatial variation of D_{25}, D_{50}, and D_{75} for the observation conducted in 2015

2016 Experiment Observations

The 2016 observation was conducted in the middle of the year on May 24 and June 2 when the beach was calm and experienced mild waves. The profile has already recovered from high wave climate effects and sediments were deposited near to the shoreline (Fig. 5.10). The offshore bar is visible again but is closer in the nearshore direction than in the

year 2014. Two core sampling sessions were carried out on May 24 and June 2, 2016. The results of both sessions are displayed in Figures 5.13a and b, respectively.

The median diameter of all samples remained around 0.2 mm, except for the locations closest to the shore (x = 0 and 20 m; Fig. 5.13). Very fine sand has been collected along the cross section during the depositional period. However, according to the results at x = 20 m, the sediments near the shoreline consist of various grain sizes within 5 mm. Similar gaps between the percentile diameter values are recorded near this location, as mentioned for previous observation years. The results of both observations in 2016 show similar trends with respect to the grain size variation. The results obtained on June 2 were used for further analysis.

(a)

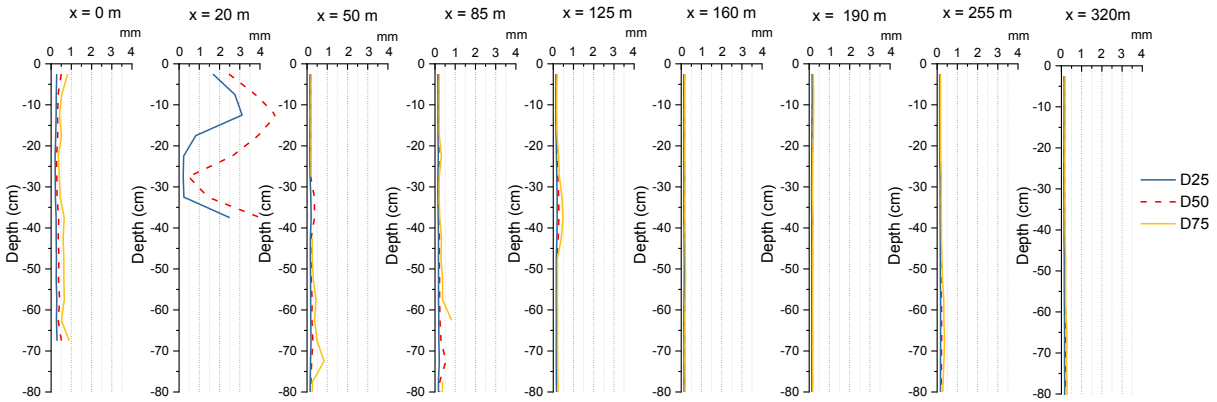

(b)

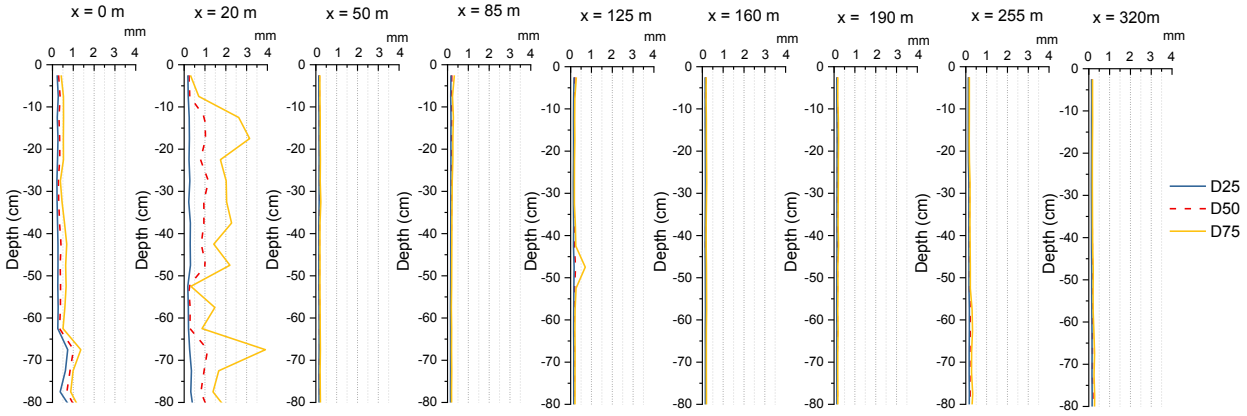

Fig. 5.13 In-depth and spatial variation of D_{25}, D_{50}, and D_{75} for the observation conducted on (a) May 24 and (b) June 2, 2016.

2017 Experiment Observations

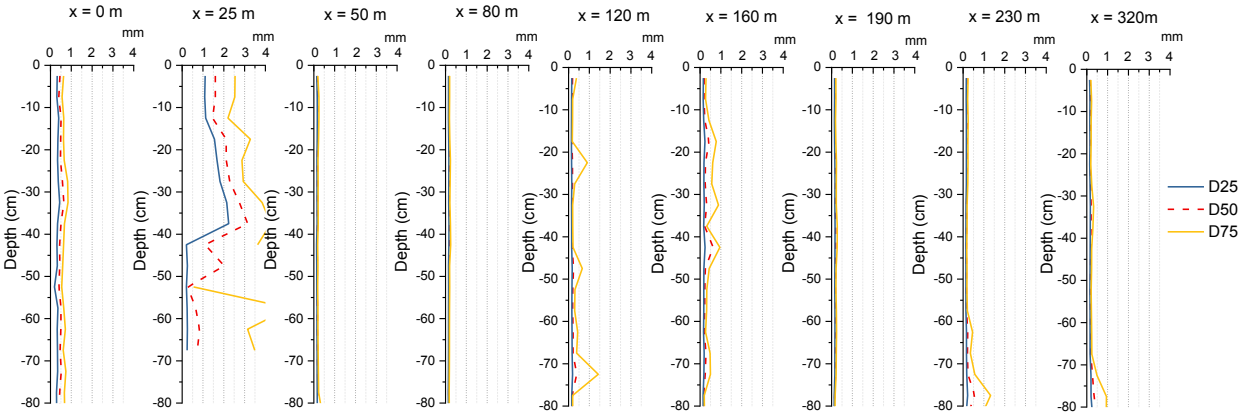

Fig. 5.14 In-depth and spatial variation of D_{25}, D_{50}, and D_{75} for the observation conducted on May 21, 2017.

The 2017 core samples were divided into 5 cm intervals and the same procedure of diameter percentile analysis was done. The observed diameters as in Fig. 5.14, showed large percentile values at location x = 25 m and several gaps in D75 at locations of x = 120, 160 m and at deeper elevations of x = 230, 270 m. The rest of the locations' percentile diameters were almost around 2 mm in size.

The in-depth diameters of certain locations differ and shifted between x = 0 to 320 m each year. During each observation year, the percentile diameters of several locations were comparatively higher/coarser (x = 0, 80, 150 m for 2014, x = 40, 80, 215, 270, 320 m for 2015, x = 20 m for 2016 and x = 25 m for 2017) than at the rest of the sample locations. These locations are plotted in Figure 5.15 along with the bed profiles.

The lowest bed levels along the cross-shore direction to the offshore for all three years can be identified based on the figure: x = 0 - 20 m in 2014, x = 20 - 40 m in 2016, x = 40 - 125 m in 2015, x = 125 - 215 m in 2014, and x = 215 m in 2015. The marked locations falls on these lowest profiles along the cross-shore direction, except for x = 10 m.

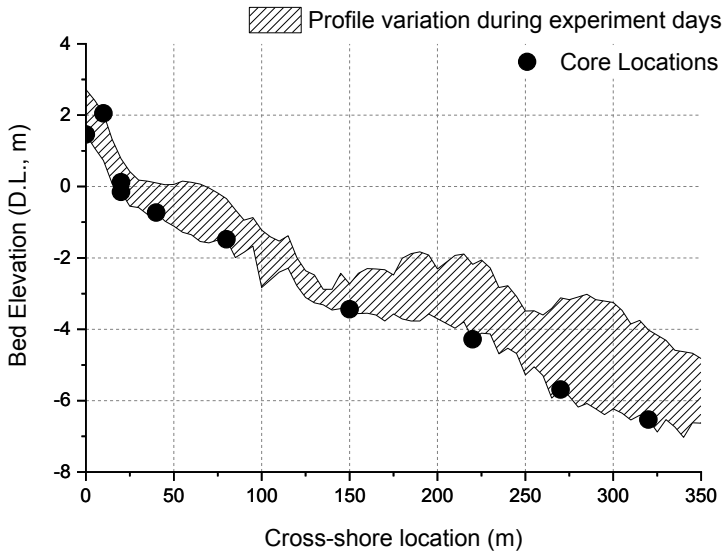

Fig. 5.15 Profile variation for the observation years 2014, 2015, 2016, 2017 and the sample locations with percentile diameter gaps.

This pattern suggests an in-depth sediment layering of the mixed particle sizes at each location from the shoreline to the offshore. If the diameters in-depth can withstand the energy dissipated at the Hasaki Coast, the bed profile variation along the cross-shore direction might be limited. To justify this suggestion, the profile variation for every week, from the first day of all the observations (October 19, 2014) to the last day of the observations (June 2, 2016), has been plotted in Figure 5.16.

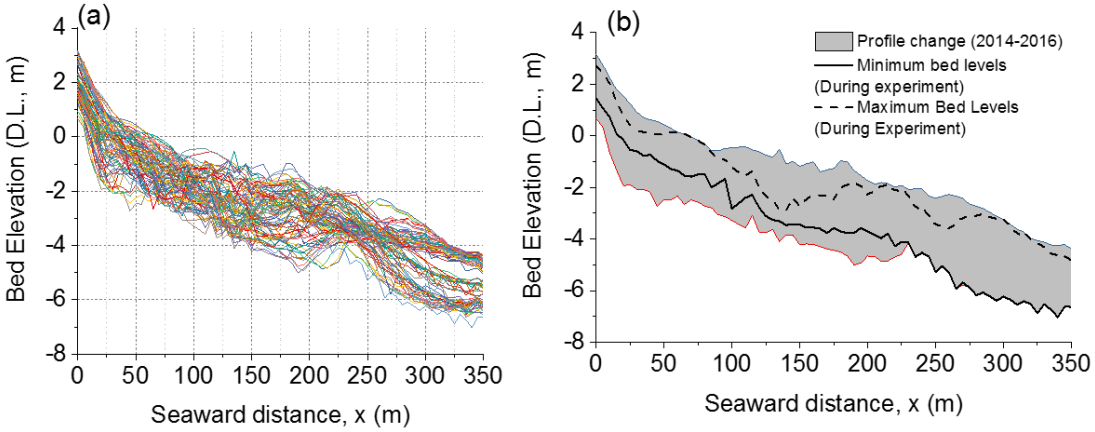

Fig. 5.16 Beach topography change from October 19, 2014, to June 2, 2016, data from HORS, PARI.

The vertical profile variation of the weekly profile changes from October 19, 2014 to June 2, 2016, is shown by the ash-colored area in Figure 5.16 along with the minimum profile variations (solid black line) and the maximum bed profile values (dashed black line) for each field observation day. Figure 5.16 shows that the bed profile has not been eroded below the 2015 profile measurements from $x = 225$ m to the offshore. Nonetheless, the area $x < 225$ m was eroded for 1 to 2 m from the minimum bed elevations measured during the observations. Although the bed profile is eroded when $x < 225$ m, the sediment size increases with depth at locations marked in Fig 5.15.

5.1.2.1 Cross-shore Sediment Zones and their Properties

To further analyze the soil samples, the area was divided into four sections, that is, Zones 1 to 4 from onshore to offshore (Fig. 5.17). Zone 1 extends from the average shoreline to the end of the swash zone, Zone 2 from the swash end to the nearshore side of bar trough 1, Zone 3 is within the offshore bar in 2016, and Zone 4 is on the offshore side. All four core sampling day profiles were plotted and the zones were chosen depending on bed profile variations.

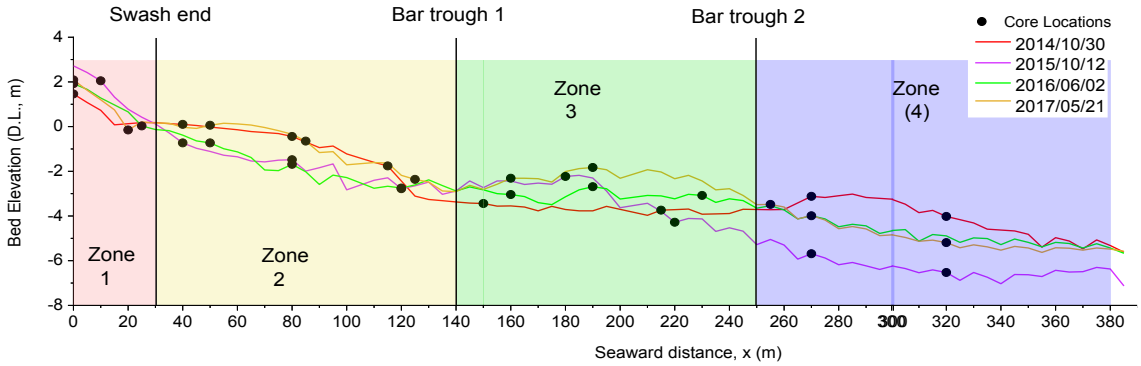

Fig. 5.17 Cross-shore zones defined according to bed profile variations.

In addition to the bed profile characteristics of the each zones, the shields stress of the zones and wave height distributions were calculated (eq. 5.1) by transforming the waves from the offshore locations of pier. The wave height records of HORS offshore points at location x = 380 and 303 m and nearshore point of x = 260, 145, 40, 10 were used in verification of waves transformed.

$$Hrms = a^{1/5}h^{9/10}\left[1 - h^{23/4}\left(\frac{1}{h_0^{23/4}} - \frac{a}{r_0^{5/2}}\right)\right]^{-1/5} \quad \text{.....eq. 5.1}$$

where $a = \frac{23}{15}\left(\frac{g}{\pi}\right)^{1/2}\frac{\gamma^4 \tan\beta}{B^3 f_p}$ and $r_0 = H_0^2 h_0^{1/2}$.

The significant wave heights were transformed to H_{rms} (Thornton and Guza, 1986) values in the offshore before transformations. The offshore wave depth and wave height are denoted by h_0 and H_0 respectively. The value of γ is based on the field data and breaking style, where B also depends on the wave breaking style which is <1 for spilling and almost 1 for plunging breakers. The f_p is taken as the $1/T_p$ as recorded by the wave data. The shields stress was calculated for each zone using the equations 5.2 (Thornton and Guza, 1986) and 5.3 (Camenen and Larroudé, 2000) mentioned below;

$$|\bar{u}|\ (Wave\ velocity) = \frac{1}{2}\left(\frac{g}{h}\right)^{1/2}\left[\frac{\sqrt{\pi}}{2}H_{rms}\right]\left(\frac{2}{\pi}\right) \quad \text{.....eq. 5.2}$$

$$\emptyset\ (Shields\ Parameter) = \frac{0.5 C_f \bar{u}^2}{(s-1)gd} \quad \text{.....eq. 5.3}$$

where C_f is the friction factor of 0.01, s is the specific gravity of sand, d is the diameter. The values used for each parameters are given in Table 5.3. The verification graphs are added in the Appendix E for further clarifications.

Table 5.3 The parameter values used for wave transformation for Hasaki coast

Parameter	Value used	Reason
γ	0.34/0.4	Calibrated and verified
$\tan\beta$	1/80	Calibrated and verified
B	0.5	Assuming mostly plunging waves
h_0, h	AWL- topography	h_0 - used 23.4m as per literature for NOWPHAS location
H_0	varies	Use from the buoy data offshore

The transformed wave heights and the calculated shields parameter values for the entire duration of the experiments are further given in Appendix E. The Fig. 5.18 shows

the average shields parameter for each zone during the experimental periods. The maximum values of average shields parameter holds for 2015 which was hit by 2 storm events. Except for this year, the maximum shields parameter is within zone 3 which might be prone to maximum amount of sediment movement in the entire cross-shore region. The least of all the average values are in zone 1, where the sediment movement is minimum which was also mentioned by Yanagishima (2016).

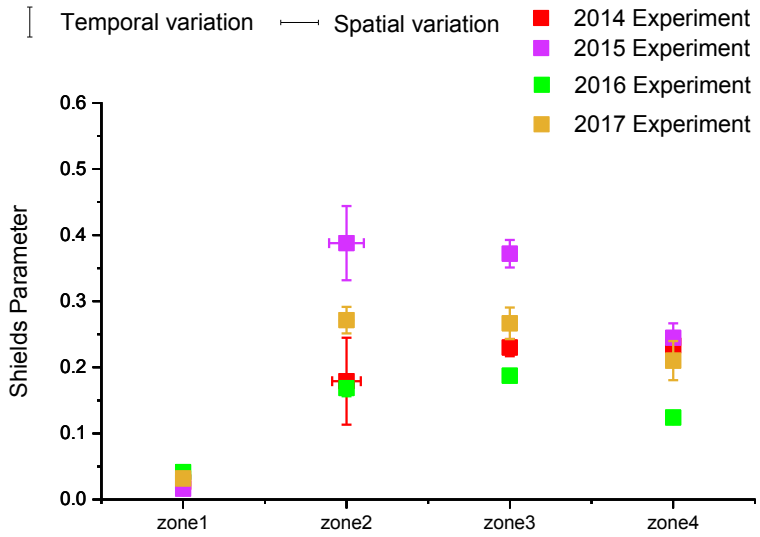

Fig. 5.18 The calculated average shields parameter and the temporal and spatial standard deviations inside each zone for experiment year 2014, 2015, 2016 and 2017

Zone 1: Swash Area

Zone 1 starts at $x = 0$ m and ends at $x = 30$ m, which is in the swash area. A steep bed profile is visible; four core samples were collected from this zone. Each color represents the year of the observation (Fig. 5.19). After the 2014 observations, the sediments moved into shore direction. Sediments were deposited in the sloped bed, creating the highest elevations in 2015 (Fig. 5.19a). Figures 5.19b and c show the results for the sorting coefficient and skewness, respectively. The size of each dot represents the median diameter for each location. Figure 5.19b shows that some sample values remain below 4, while most of them are below 2.

According to the sorting coefficient classifications of Trask (1932), the samples on the surface are along the range from well to poorly sorted, while they become poorly

sorted with depth. The skewness values in depth and size variation are plotted in Figure 5.19c. The top layers of the sample are much concentrated around unity or lean towards finer skewness, while the samples at the smallest depths clearly show a finer skewness. Except for the location x = 0 m data of 2016, overall, the zone consist of moderately to poorly sorted, finer or symmetrically skewed sediments. The existing diameter varies in no particular order; mainly coarser sediments. The overall properties were verified by the addition of 2017 data which has a similar profile and diameter trend as 2016 data. The year also consisted of the most coarse sand compared to other experiment days.

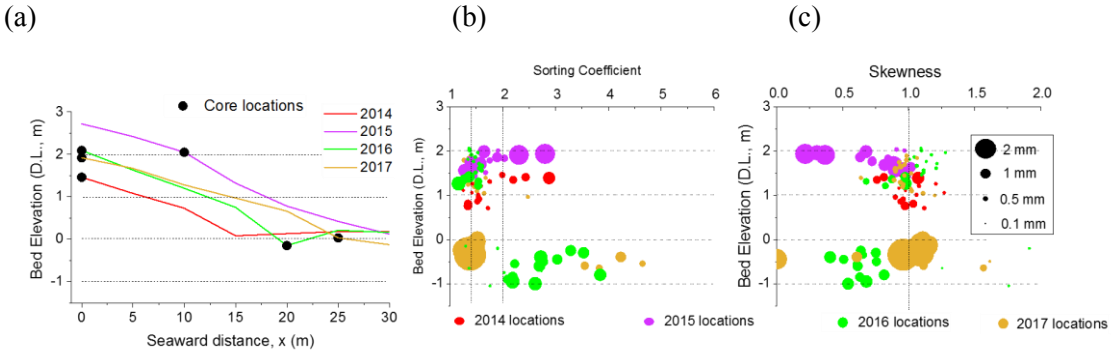

Fig. 5.19 Results obtained for Zone 1; (a) bed profile and core locations, (b) sorting coefficient (S_0), and (c) skewness (S_k). [Note: $1>S_0>1.4$ well sorted, $1.4<S_0<2.0$ moderately sorted, $2.0<S_0$ poorly sorted]

Because of the coarser sand and poorly sorted materials in this area (for a depth of 1 m in bed elevations) compared with the other zones, the beach slope remains compacted and fixed. Finer particles gathered during mild wave conditions at location x = 0 m in 2016, would wash away into offshore direction once the high waves attack the shore, which keeps the beach face slope constant, as reported in Yanagishima (2016).

Zone 2: Area between the Swash End and Trough

The cross-shore distance from x = 30 m to 140 m defined as Zone 2 is shown in Fig. 5.20. The lowest bed profile for the zone is observed for 2015 (Fig. 5.20a), while the 2014 and 2016 profiles remain almost equivalent up to x = 110 m.

The sediments in this zone have a sorting coefficient below 2, except for five data points (Fig. 5.20b). During 2014 and 2015, the sediment samples at the x = 80 m location are moderately sorted and the other core samples are well-sorted. The grain size is finest

in this zone compared with the other three zones of the study area. This indicates the segregation of finer particles from the cross-shore profile and deposition in Zone 2 during high wave climate years (2014 and 2015). Because the observations were conducted during depositional wave conditions in 2016, the highest concentration of 2016 sediment samples is within unity, showing a symmetrical sediment pattern; almost all other values are coarser skewed (Fig. 5.20c). As of verified by 2017 data, the trend of sediment properties remain same where the zone consists of very fine, well-sorted and coarser skewed sand. The 2017 profile has also followed the least elevation levels within the zone as similar to 2015.

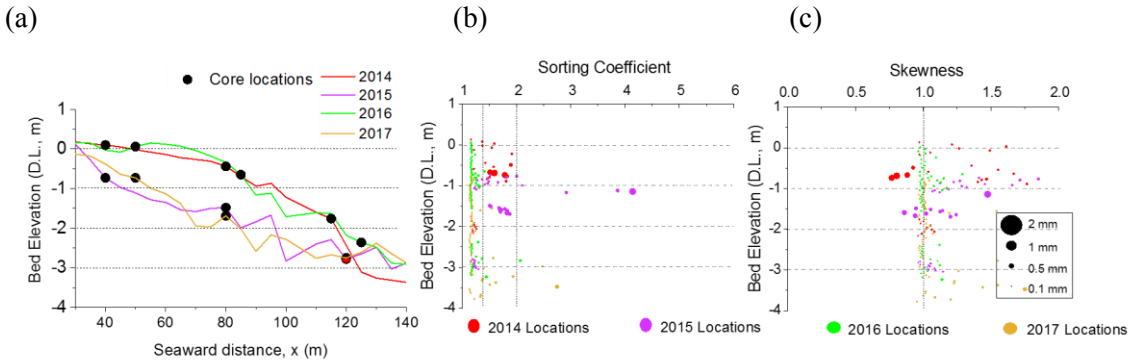

Fig. 5.20 Results for Zone 2; (a) bed profile and core locations, (b) sorting coefficient (S_0), and (c) skewness (S_k). [Note: $1>S_0>1.4$ well sorted, $1.4<S_0<2.0$ moderately sorted, $2.0<S_0$ poorly sorted]

Zone 3: Onshore-Biased Bar Location

Zone 3 lies within the cross-shore area at x = 140 - 250 m, which includes the bar crest in 2016. Based on Figure 5.21a, rapid bed slope change occurred in 2015. Six core samples were collected from this region.

Figures 5.21b and c show that the median diameter, equivalent to the size of the circle, again significantly increased with depth. The D_{50} value at a bed elevation of -2 m to -3.25 m is very small in 2015 and 2016; it increases thereafter. According to the bed elevation in Figure 5.21a, median diameter difference between the elevations -2 m and -3.25 m to less than -3.25 m, is due to the bar crests in 2016. The diameters increase below an elevation of -3.25 m because they approach the bar trough of 2014. The sand samples from these elevations are very well-sorted and symmetrically distributed, while the

sorting becomes poor and finer skewed below a bed elevation of -3.25 m. Eventhough the sediment size is around 1 mm for 2017 data, the sorting and skewness follows the trends of 2014 and 2015 as reach further in depth.

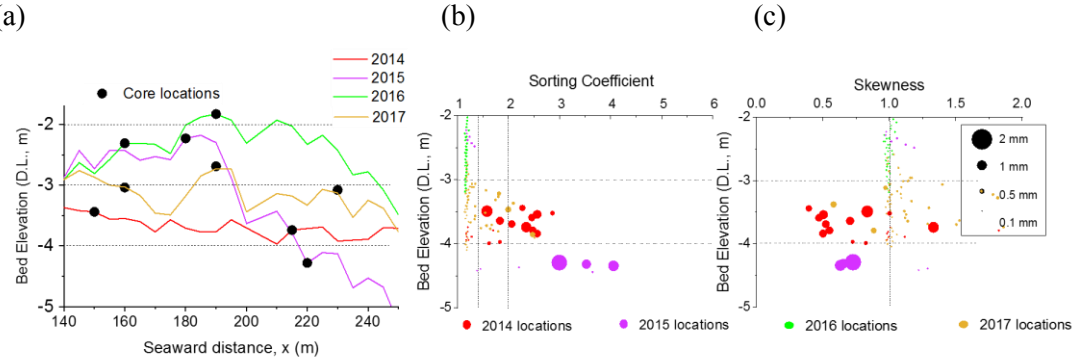

Fig. 5.21 Results for Zone 3; (a) bed profile and core locations, (b) sorting coefficient (S_0), and (c) skewness (S_k). [Note: 1>S_0>1.4 well sorted, 1.4<S_0<2.0 moderately sorted, 2.0<S_0 poorly sorted]

Zone 4: Offshore-Biased Bar Location

Zone 4 lies at x = 250 - 380 m. The largest depth profile variation occurred in this zone, which shows an elevation difference of approximately 3 m. The bar crest in 2014 lies within this region and the lowest bed levels were recorded during the 2015 observation (Fig. 5.22a). Based on Figures 4.23b and c, a depth increase of the median diameter and sorting can be noticed in this zone and in the core sample collected from the 2015 bed profile.

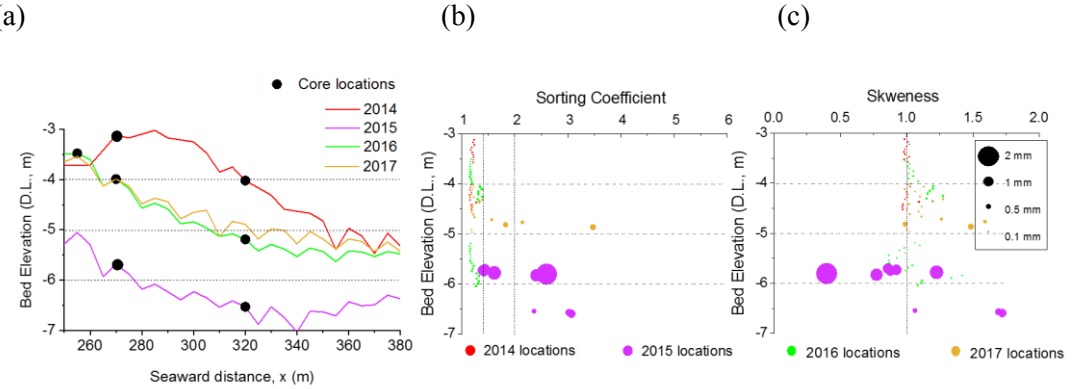

Fig. 5.22 Results for Zone 4; (a) bed profile and core locations, (b) sorting coefficient (S_0), and (c) skewness (S_k). [Note: 1>S_0>1.4 well sorted, 1.4<S_0<2.0 moderately sorted, 2.0<S_0 poorly

sorted]

The zone consists of well-sorted sediments up to a bed elevation of -5.75 m when it suddenly becomes poorly sorted. However, at most depths, the samples are symmetrical or finer skewed, except for the 2015 values, which show mixed values of coarser and finer skewness.

The sediment characteristics, such as sorting, skewness, and the mean diameter, of all the zones are summarized in Figure 5.22. The symbols represent the average values for each 1 m depth and the standard deviation is given using error bars. Zone 1 consist of medium-sized sand with an average size between 0.425 mm and 2.0 mm based on ASTM standards (Fig. 5.22a). The average D_{50} and deviation of the sediment size from the averages in this zone are larger than that of other areas. The sediment diameter of Zone 2 is the smallest (~0.2 mm). The offshore Zones 3 and 4 show an increment in the diameter size with depth. The diameters reach that of medium-sized sand in the lower layers of Zones 3 and 4 (Fig. 5.22a).

Figure 4.24b shows the sorting values for each 1 m depth interval averaged using the results obtained from core sample analysis. Zone 1 consist of either moderately or poorly sorted sediments and well-sorted samples can be found in Zone 2 and at the initial depths of other zones (Fig. 5.22b). The skewness of the surface of each zone is within unity and becomes coarser with depth (Fig. 5.22c). However, the skewness range is higher near the shoreline (bed elevation 0 to -2 m). The figures also show a positive correlation of sorting and sediment size, which both increase.

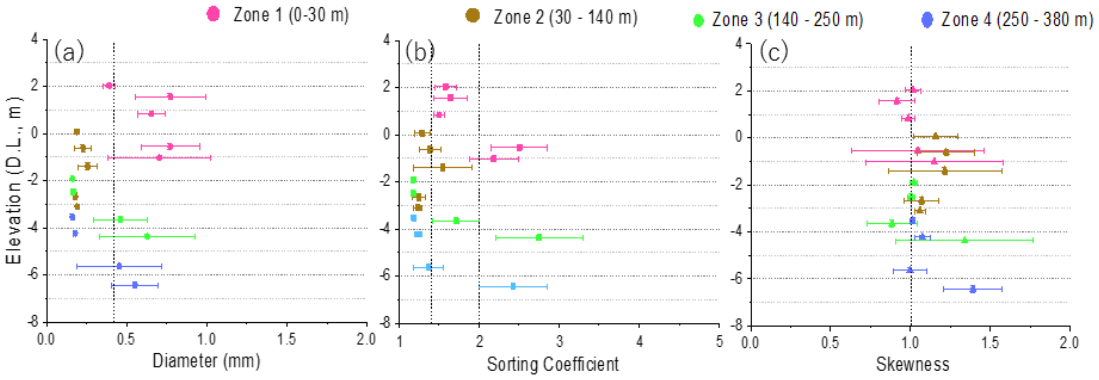

Fig. 5.23 Averaged depth and standard deviation of each parameter in each zone; (a) D_{50}; (b) sorting coefficient, S_0; and (c) skewness, S_k.

A significant negative correlation can be observed between Zones 1 and 2. Zone 1 consists of coarser, poorly sorted material, while Zone 2 comprises finer, well-sorted material. The deeper locations of Zones 3 and 4 show a similar trend, that is, increasing diameter and sorting. Overall, two primary layers are created under the two beach conditions: poorly sorted coarser material that is exposed to erosion of bed material during high wave conditions and a well-sorted, finer particles, which is transported from offshore to onshore by mild waves, currents and by the backwash due to wave breaking. During erosional conditions, the finer layer of sediments is dragged away exposing in-depth coarser, poorly sorted sediment layers that were observed at the depths of Zones 3 and 4 and in Zone 1. These in-depth coarser, poorly sorted layers seem to consist of well compacted sediments creating a stagnant beach profile along the cross-shore, which can only be damaged by high waves and speedy bottom currents. After high-wave conditions, the area will recover and fine sediment layers will be deposited on these coarser layers. This will be repeated every year under mild and high wave conditions, generating different beach profiles. However, the shape of the bed profile is considered to be limited to a certain depth because of the well compacted coarse material, which was confirmed by weekly bed profile variations (Fig. 5.16), as mentioned before.

5.1.3 Experiment Conclusions

Understanding the sea bed sediment characteristics and their segregation and sediment mixing/movement during seasonal wave conditions leading to bed profile evaluation was explored by four field observations conducted in the Hasaki Coast, Japan. The coast is vulnerable to both high waves and mild beach conditions during winter and summer, respectively. An offshore bar crest moves in on-offshore direction during each period. The area shows heterogeneous sediment behavior, both spatially and in depth. Four field observations were conducted at this coast and sediment cores were collected from the shoreline to the offshore end of the surf zone. The cores were subdivided into 2.5 cm or 5 cm layers. Each sand layer was manually checked for the tracer particles in depth for sediment mixing analysis and the sediment characteristics of vertical profiles from the swash zone to the offshore side of the outer bar were investigated.

The area near the shoreline includes coarser material, that is, poorly sorted sand showing depth-dependent skewness variation. The existence of coarser material in this region, which causes a steep bed slope profile, has also been discovered by Yanagishima (2016). The sorting becomes poor in this region, which is possibly due to the mixture of

existing coarser material with finer sediments that pile up near the shore during mild wave conditions. According to the sorting and sediment size, the area has higher energy and turbulence, which could be due to wave breaking. The cross-shore from x = 30 - 140 m, which lies between the offshore bars and steep beach face slope, consists of finer, very well-sorted sediments with a coarser skewness compared with that of other zones. The good sorting could be due to the laminar flow and backwash after wave breaking and overtopping near the shore, which sort out particles with larger diameters that were deposited on the shoreline and become finer afterwards. The cross-shore region offshore beyond x = 140 m shows a similar trend with respect to the diameter, sorting, and skewness. The particles become coarser and poorly sorted with a higher skewness range. The trend in the sediment characteristic change is significant in these areas, suggesting vertical layering of sediments, which should be further investigated. An offshore bar of morphology changes occurred in the region, by the high waves moving/creating a bar crest with well sorted, finer particles from the offshore and troughs which expose the coarser, poorly sorted layers underneath.

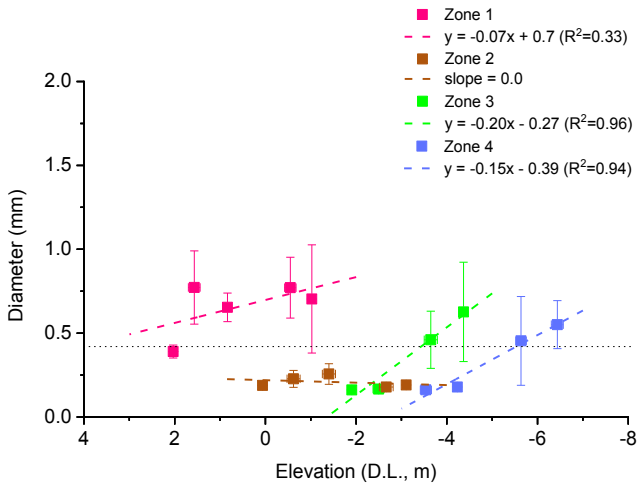

Fig. 5.24 The average values and the standard deviations of D_{50} along the depth of each zone for Hasaki Coast

The arrangement of the bed profile has a direct impact by the sediment properties. Based on the weekly profile measurements, the bed profile offshore beyond x = 225 m has a limited erosion depths constraining the profile change. Further studies need to be carried out to understand the bed profile limitations of the cross-shore profile of the study area.

The sediment diameter and sorting pattern increase with depth has been justified using the Fig. 5.24 which could be further verified by series of core sample analyses. The prediction of sediment diameter at each zone along the depth of the sea bed profile could be possibly done with further validations.

5.2 Sediment Mixing in Hasaki Coast, Japan

Along with the sediment properties, the sediment mixing depths were to be discovered. The mixing depth was defined as similar to the previous definitions. The intension of this study was to analyse the effect of sediment properties on sediment mixing and movement. The mixing depths were discovered by the tracer particles which were placed before each experiments.

5.2.1 Observations of Sediment Mixing

Amount of each coloured tracer particles were counted manually by Masters and Undergraduate students for each sand layer of core samples for the years 2014, 2015 and 2016. The sediment mixing depths are defined as the depth where the tracer particles have intruded in from the surface elevation on the core sample day (D_1). The results of the experiment in 2014 (Fig. 4.9), 2015 (Fig. 4.10) and 2016 (Fig. 4.11) of their mixing depths according to the definition and the movements are given. The detailed figures of amount of tracer at each core location is given in Appedix D.

From Fig. 5.25, it was discovered that the tracers were only moved within the initial location. The blue tracer was not found at any of the locations suggesting it was washed away either to the offshore direction or in the longshore direction which was further investigated by Suzuki et al. (2017). It was later discovered the offshore bar at the location of 250 m in the cross-shore direction has an effect of the movement of tracer in space separating the movements of pink and yellow to the onshore side and green and red in the offshore side of the bar. A maximum of 50 cm mixing depth was discovered from the experiments of 2014.

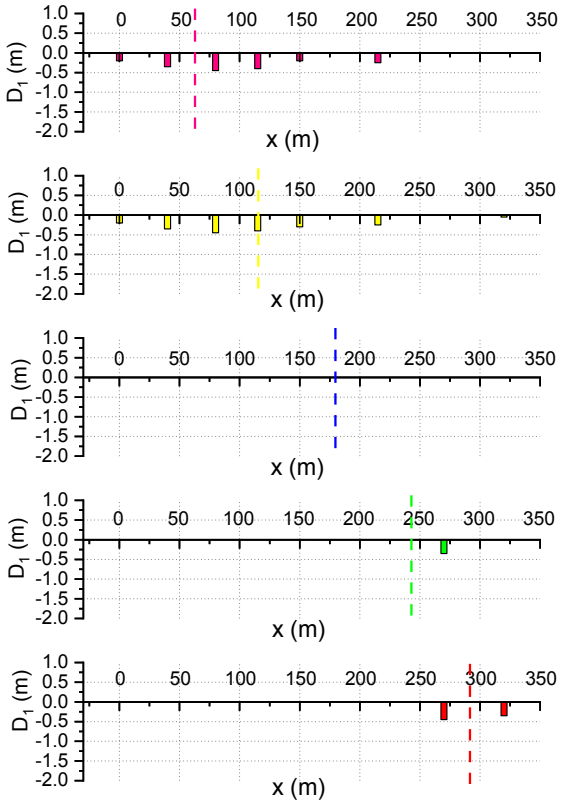

Fig. 5.25 The sediment mixing depths and movements for each tracer colour in the cross-shore direction for 2014.

During the year 2015, eventhough the profile was eroded drastically during the stormy events, the particles were moved and mixed in the onshore direction as seen in Fig. 5.26.

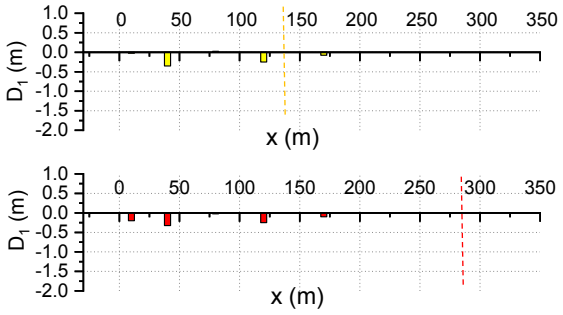

Fig. 5.26 The sediment mixing depths and movements for each tracer colour in the cross-shore direction for 2015.

The recorded mixing depths were smaller than the previous year. However the profile change from the day of tracer placement is much larger, which is difficult to decide on the exact mixing depth. The Fig. 5.27 shows the mixing depths for 2016 two experiments. The initial position of tracers are given in a vertical dashed line at their initial position along the cross-shore profile. The tracers of pink has mixed in within the initial location area in depth upto a 1 m and the yellow tracer was seen to mix along the bed profile from offshore to onshore with almost a constant depth level of 0.5 – 1.0 m. The blue tracer was initially mixed at the position around 150 m and by the last core sample day, it was not recorded. The green tracer movement and mixing is similar to the yellow tracer and the red tracer has shifted towards the onshore side while mixing in depth upto a 1 m.

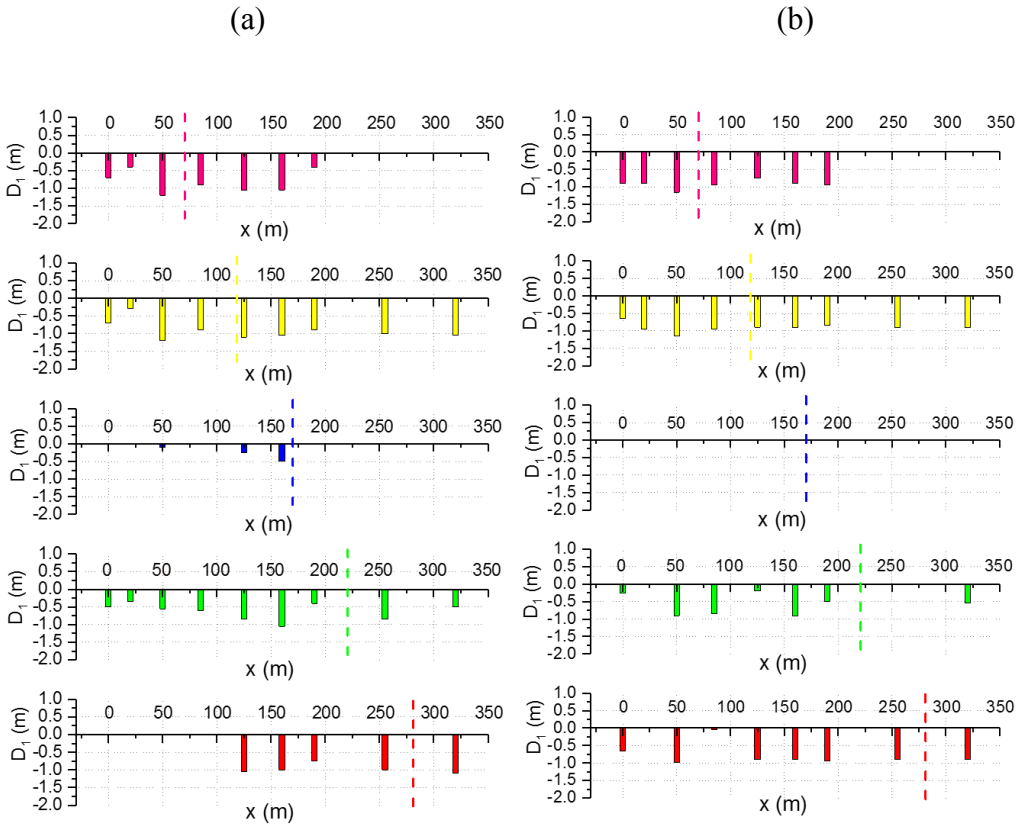

Fig. 5.27 The sediment mixing depths and movements for each tracer colour in the cross-shore direction for (a) 2016 experiment 1 and (b) 2016 experiment 2.

Due to the large erosions in bed profile during 2014 and 2015 and accumulations in 2016, the true definition of sediment mixing was unable to analyse. The detailed descriptions of the figures are given in Appendix D and the analysis work was extended

to sediment diameter properties of the experiment periods.

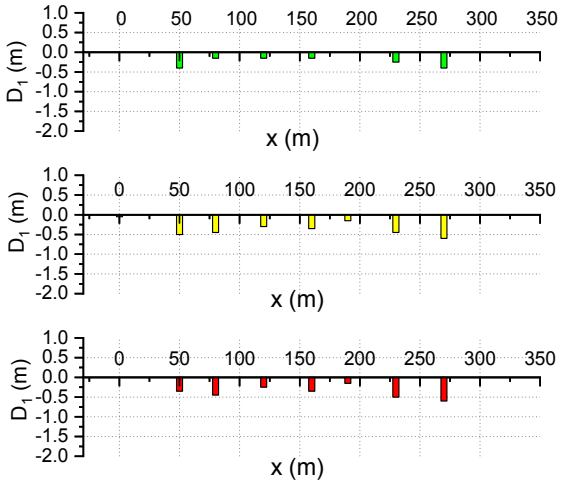

Fig. 5.28 The sediment mixing depths and movements for each tracer colour in the cross-shore direction for 2017.

For the year 2017, three colours were place at x = 80, 160 and 230 m with green, yellow and red accordingly. The colours have spread along the area from x = 50 to x = 280 m as of the core sample locations. The colour placed nearshore was mixed the least in depth compared to other two colours over the area. According to the above measurements of mixing amounts and depths, the analysis of mixing depths with sediment properties were done in the next section of the paper.

5.2.2 Mixing Depths and Spatial Sediment Properties

The total mixing depths for each location from all tracer colours in each year's experiments were calculated and plot along with the sorting and bed elevation graphs as seen in Fig. 5.29. The Mixing depth is shown in vertical error bars in the bed profile figures.

According to each zones of data, the maximum amount of mixing could be seen in zone 2 where the wave heights start to gradually decrease with time (the wave height transition zone) which also consist of fine, well-sorted sediments. The least mixing has occurred in zone 1 where coarse, poorly sorted sand exists. The upper elevations of zone 3 and zone 4, where the sediments were fine and well-sorted, the mixing could be observed.

(a) Zone 1 (0-30 m)

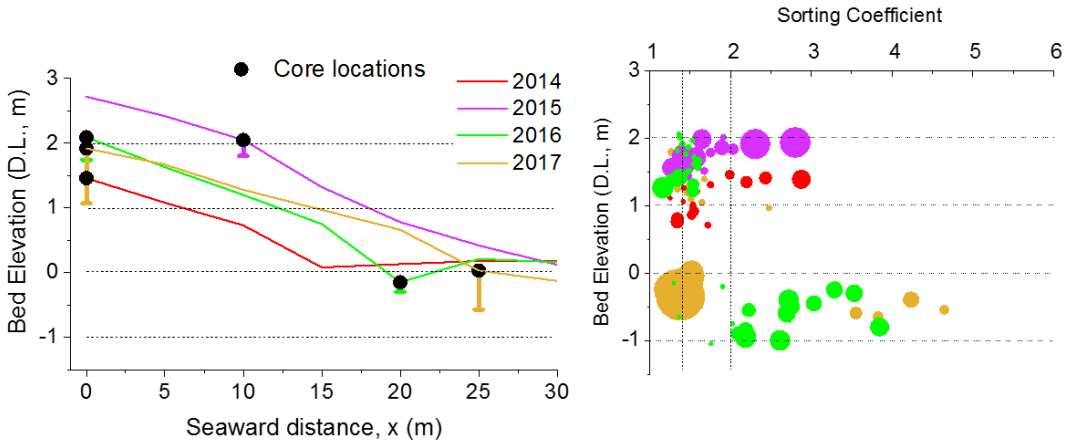

(b) Zone 2 (30-140 m)

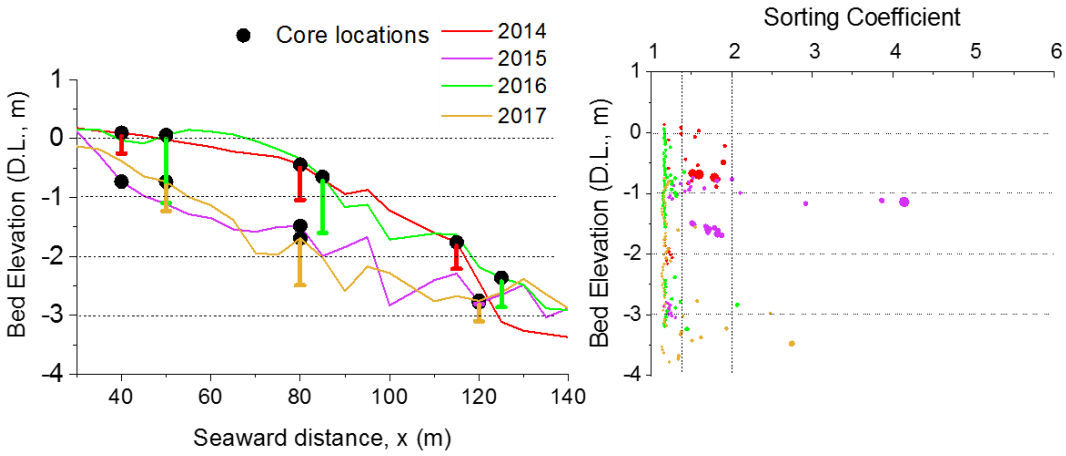

(c) Zone 3 (140-250 m)

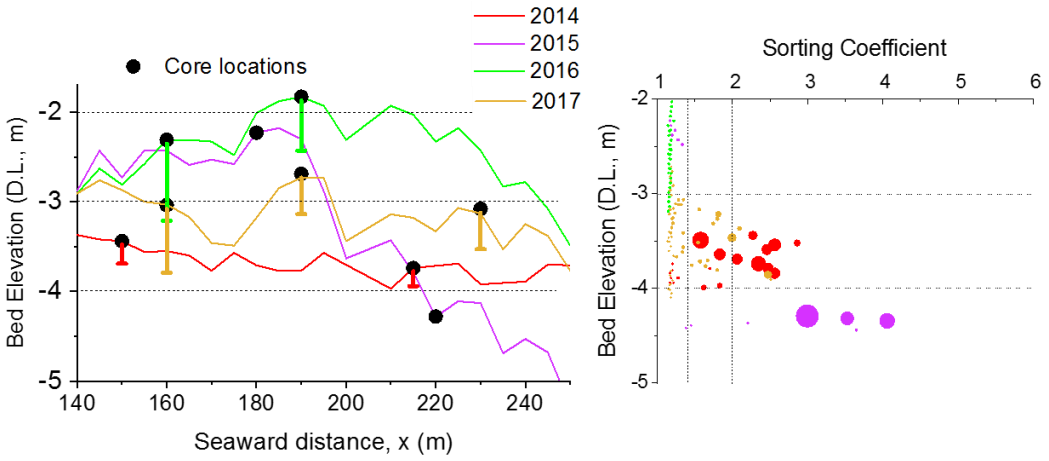

(d) Zone 4 (250-380 m)

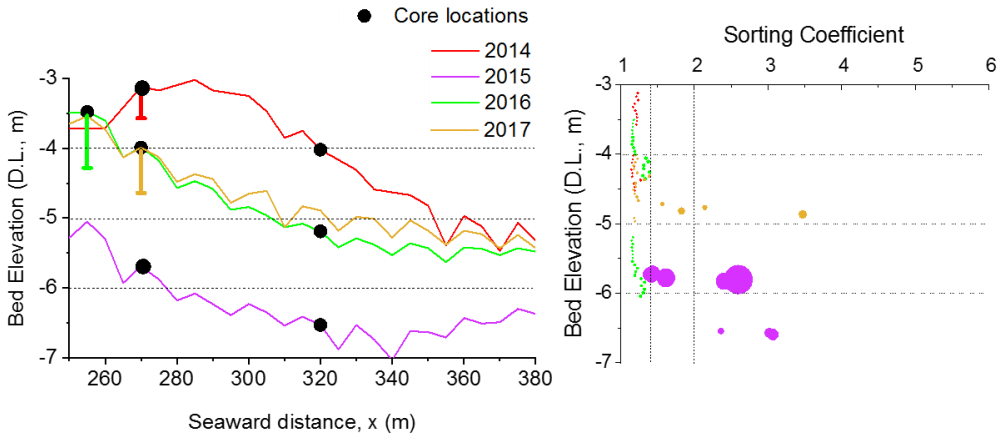

Fig. 5.29 The mixing depths compared with the bed elevation, D_{50} and sorting coefficient for each zone in each experiment year.

The results suggest a probable connection between the sediment mixing and sediment properties of D_{50} and sorting coefficient which was not observed in past literature. In order to further evaluate the relationship, the average percentile diameter and sorting coefficient at each core location depths were calculated. The data has been plot in Fig. 5.30 where the D_{50} value is represented by a scale factor and the depth average sorting value in the x-axis where the y-axis showing the mixing depth for the respective core location point.

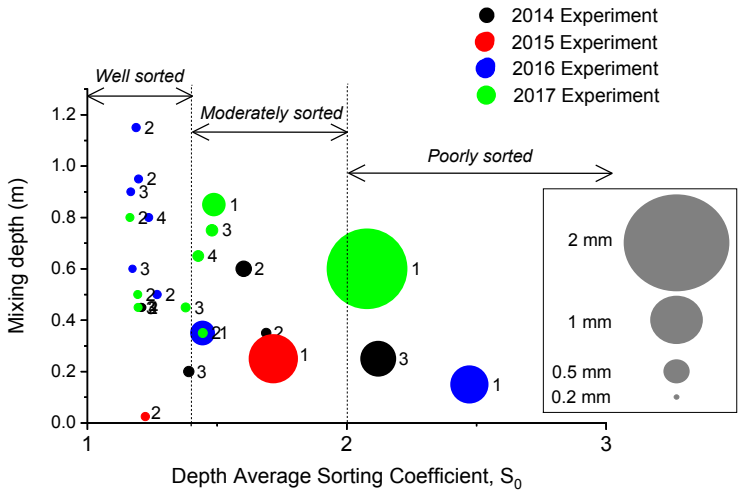

Fig. 5.30 The effect of depth averaged sorting coefficient and D_{50} for the mixing depth from the experiments conducted in Hasaki coast, Japan.

From the above figure, it is noticed that most of the location points were within the well-sorted category in the graph where the size of the sediments were least compared to other location points (<0.5 mm). Also the points were mostly from the years of 2016 and 2017. As the points approach higher sorting values, the diameter significantly increases and the mixing decrease. The overall figure suggests a significant relationship of sorting and diameter to sediment mixing which is further explained by Fig. 5.31.

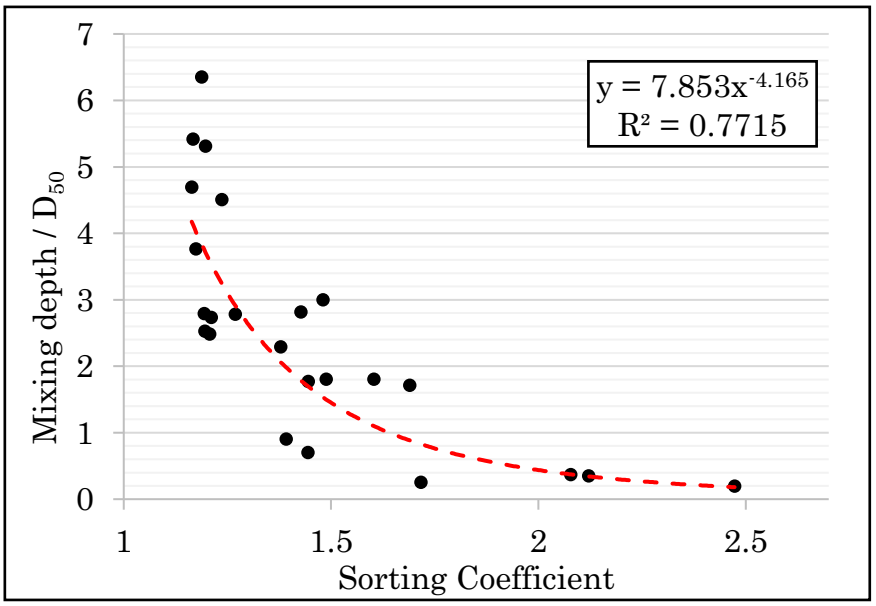

Fig. 5.31 The possible relationship between sediment properties and sediment mixing observed by the experiment data set from Hasaki Coast.

An inversely correlated relationship could be given by the location data from the swash to the end of surf zone which suggest a relationship of $y = 7.853\ x^{-4.165}$ that has an accuracy level of $R^2 = 0.77$. However, the relationship equation is only based on the results of Hasaki experiments which is probably needed to be compared with other coastal areas with a variety of beach conditions. Note that the graph values does not include the hydrodynamic conditions at each location point which is suggested to be improved further in future research work.

5.3 Sediment Diameter Inclusion

5.3.1 WD-Princeton Ocean Model Simulation

The model is a complex tool initially used for ocean circulation studies which

was able to simulate tidal current velocities which was named as Princeton Ocean Model. With further addition of wave module to the program, the model is now capable of calculating wave induced currents which was modified into Wet and Dry Princeton Ocean Model. Dr. Ken-ichi Uzaki has further introduced the sand and mud transport modules to the program and by this research, the sand module would be modified further.

For the initial simulation process, few regular waves were generated for the bathymetry of Hasaki coast, Japan. A grid system of 30 × 30 with a $\Delta x = 50$ m and $\Delta y = 20$ m (Fig. 5.32) were used which covers an area of 1500 × 600 m^2. Five vertical depth stratifications were defined which was generated by the curvilinear grid coordinates as mentioned in Section 2 of this paper. Two model runs were done in order to clear the boundary conditions and to clear out the bugs in the program caused by modifications and changes made by many researchers before. However the wave axis and the bathymetric axis has alterations from the previous researchers introduced in the program and thus, only the waves from angle = 0 (longshore) to 79.7 (from longshore) degrees could be generated by the end of the research period. The bathymetric map used in the model is given by Figure 5.33. The input parameters of the two trials are given in Table 5.4 for both trials before and after boundary condition adjustments.

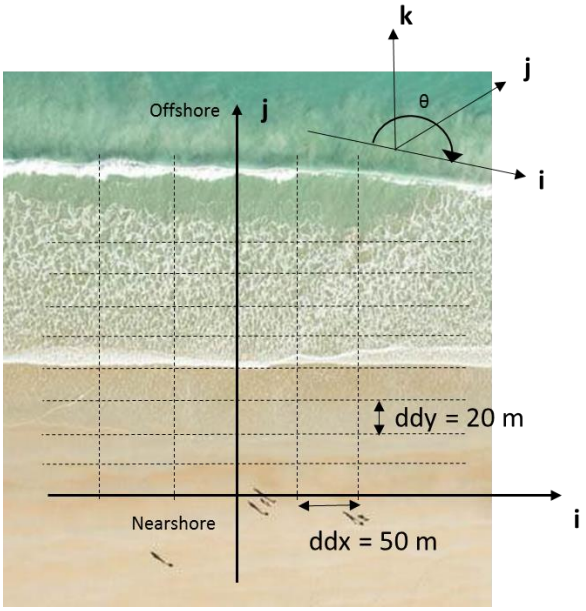

Fig. 5.32 The bathymetric grid for Hasaki coast

(a) (b)

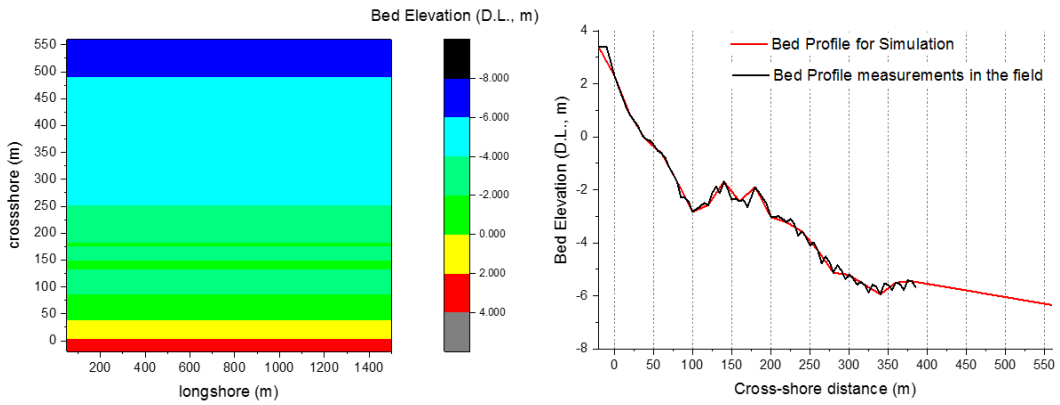

Fig. 5.33 The (a) plan view and a (b) side view of the model bathymetry input as of 2015/10/01 bed profile in Hasaki, Japan

The output results of wave height/water level distribution in the area, topography change, depth average longshore and cross-shore current velocities, bottom and top bed currents distribution are being checked for the adjustments of boundary conditions. The bed profile change after 4 days of simulation (Fig. 5.34), wave height distribution (Fig. 5.35), longshore (Fig. 5.36) and cross-shore (Fig. 5.37) depth averaged velocities are given before and after boundary condition adjustments.

Table 5.4 The input parameters of the simulation trials

Parameter	values used
Start date	2015/10/1
Calculation days	4
internal time step	0.1 sec
external time step	1 sec
Hs	2 m
Tp	12 sec
Wave angle	79.7
Water level	0 m (datum level)
Wind force	Not considered

(a) (b)

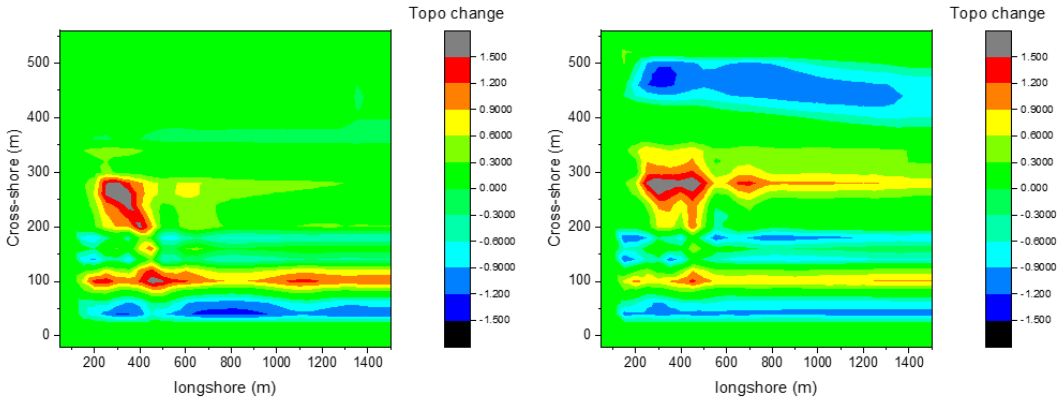

Fig. 5.34 The topography change (m) for (a) before and (b) after boundary condition adjustments

According to the bed profile changes, there are significant changes in profile erosion and accretion areas. Before the boundary conditions, there was higher erosion near to the shoreline and there is an uneven profile changes in the longshore direction due to the high viscosity boundary condition defined by the previous researches in the model program. In the trial 2 (after boundary condition adjustments), the profile variation is more evenly distributed in the longshore, but there is higher profile changes noticed in the left side of the model framework which has to be further adjusted by changing boundary onditions of other variable parameters. It could also be the influence of wave direction from the north-west direction (angle = 79.7 deg).

(a) (b)

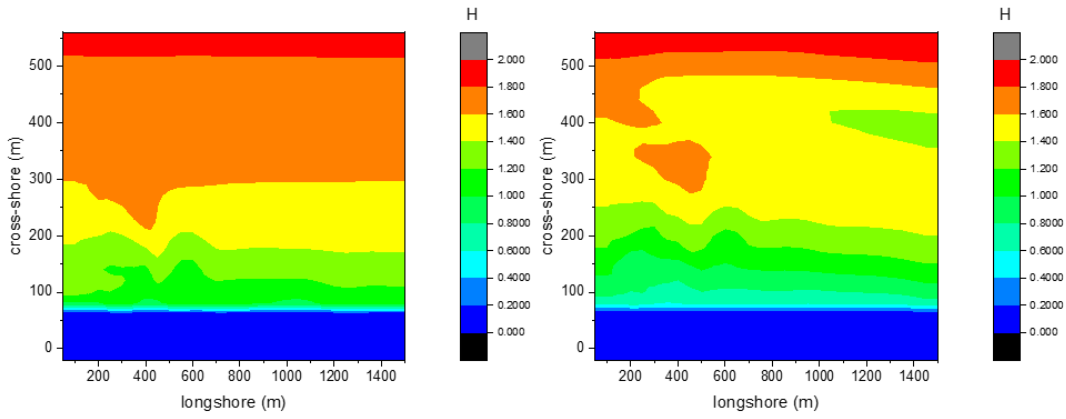

Fig. 5.35 The wave height distribution (m) for (a) before and (b) after boundary condition

adjustments

(a) (b)

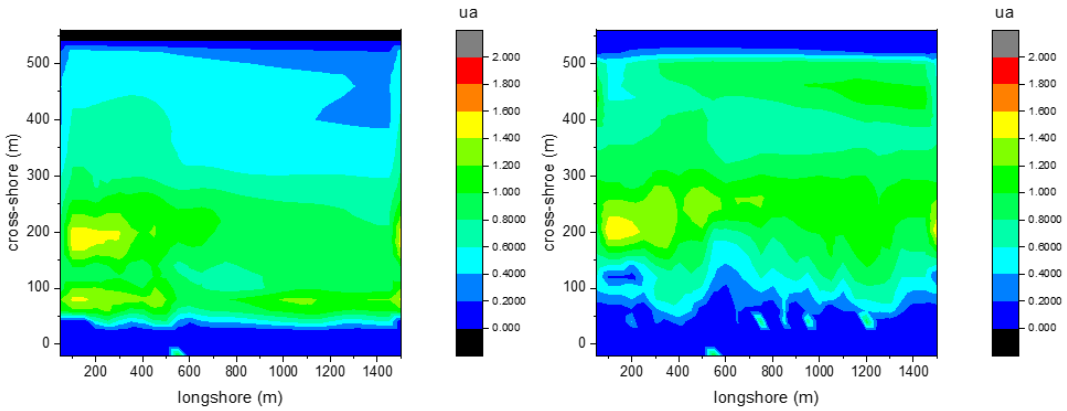

Fig. 5.36 The depth averaged longshore currents (m/s) for (a) before and (b) after boundary condition adjustments

There is a visible acute in wave height distribution which is probably due to the offshore boundary conditions which is not yet configured. There is a longshore current directing towards the right side of the model framework and a higher positive cross-shore current is observed near to the shoreline after the boundary condition fixing. The model is not successfully recovered for simulation purposes until the boundary conditions and previous research adjustments are recovered.

(a) (b)

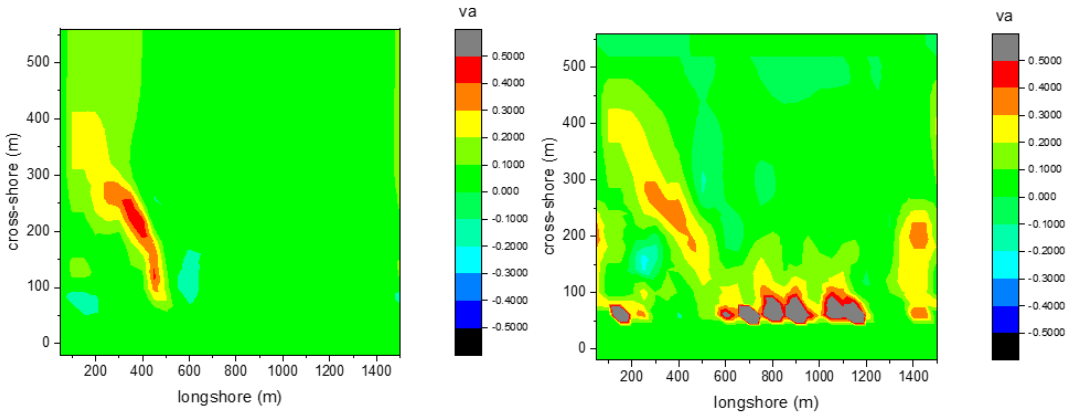

Fig. 5.37 The depth averaged cross-shore currents (m/s) for (a) before and (b) after boundary condition adjustments

5.3.2 Proposed Sediment Transport Model Adjustments

The current study is interested in modifying the sediment transport module by Dr. Ken-Ichi Uzaki in Princeton Ocean model for the inclusion of the effect of heterogeneous sand bed profile with more than one single diameter. The sediment transport rate in the sand transport model is calculated using the bed load formulae (eq. 2.9) by Bailard (1981). The formulae is slightly modified to include several diameters and the original method of bed profile modification is re-defined.

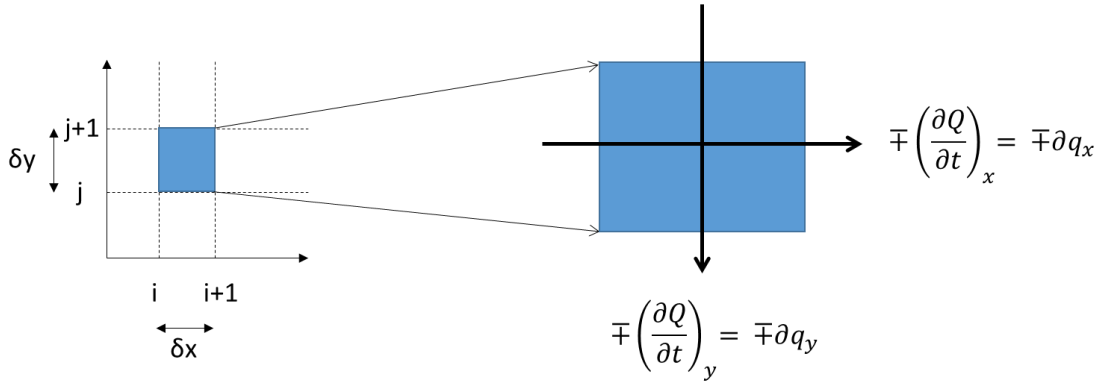

Fig. 5.38 The schematic diagram of net sediment transport calculation within a grid cell in POM

In the initial version of POM sediment transport module, the sediment rates of transport is calculated in the x (∂q_x) and y (∂q_y) axis direction (Fig. 5.38) of the bottom grids using eq. 2.9. The bed elevation difference in the cell corners would be calculated as shown in eq. 5.4.

$$\partial z = \partial t\{[\partial q_x(i+1) - \partial q_x(i)]\partial x + [\partial q_y(j+1) - \partial q_y(i)]\partial y\} \quad \text{.....5.4}$$

where ∂z is the elevation difference due to the net sediment transport within the cell; ∂t is the time interval of sediment calculations in POM, ∂x and ∂y are the grid spacing length of both x and y directions respectively.

Considering the approach of longshore sediment transport rates calculated by the concept of Bagnold model for a mixed sand beach (Serizawa et al., 2017), the Bailard model of transport is modified. In the concept includes addition of an extra terminology of volume content rate calculated for each diameter size (eq. 5.5 to eq. 5.8) as introduced by Uda et al. (2004) and Kumada et al. (2006).

$$\vec{q_t^k} = \mu_k \left[\vec{q_x^k} + \vec{q_y^k} \right] \quad (k = 1,2,3,\ldots,N) \quad \ldots\ldots 5.5$$

$$\frac{\partial Z^k}{\partial t} = -\nabla . \vec{q^k} \quad (k = 1,2,\ldots,N) \quad \ldots\ldots 5.6$$

$$\frac{\partial Z}{\partial t} = \sum_{k=1}^{N} \frac{\partial Z^k}{\partial t} \quad \ldots\ldots 5.7$$

$$\frac{\partial \mu^k}{\partial t} = \begin{cases} \frac{1}{B_h}\left(\frac{\partial Z^k}{\partial t} - \mu^k \frac{\partial Z}{\partial t}\right) & \frac{\partial Z}{\partial t} \geq 0 \\ \frac{1}{B_h}\left(\frac{\partial Z^k}{\partial t} - \mu_B^k \frac{\partial Z}{\partial t}\right) & \frac{\partial Z}{\partial t} < 0 \end{cases} \quad \ldots\ldots 5.8$$

where the net sediment transport rates in x, y directions for each sediment size class of k, (q_t^k), calculated by the Bailard model (ep. 2.9) will be multiplied from the additional term μ_k which is the volume content for each sediment class. Initially the value of μ_k will be assumed as per the study area as a percentage of volume content of each sediment class of k. The value of k represent the number of sediment classes in the area considered. B_h is another additional parameter introduced as the thickness of the exchange layer which is assumed to actively participate in change of bed elevation. The value of B_h is assumed to be the maximum particle size out of all sediment classes considered.

The calculation modifications in each step introduced with respect to the new method could be given summarized as in Table 5.5. Additional steps were introduced to the sand transport flux calculations and bed profile update.

Table 5.5 The step by step alterations for the sand transport model in WD-POM

Step no.	Current Method	Proposed Method
1		Take the volume rate (μ^k) of each diameter size k where k = 1,2,3…
2	Calculate Sediment Flux (q) using the Bailard Model according to bottom flow velocities using a single diameter (D50)	Calculate Sediment Flux (qk) using the Bailard Model according to bottom flow velocities for all diameters (Dk) and combine the sediment fluxes
3	Calculate the bed elevation change rate (∂ Z/ ∂ t) for D50 by multiplying the cell dimensions	Calculate the bed elevation change rate for each diameter (∂ Z/ ∂ t)k , multiply by the cell dimensions and sum up each elevation differences
4		Calculate the new volume content rate for each cell depending on the bed change
5	Update the new bed levels by Znew = Zold ∓ ∂ z	Update the new bed levels by Znew = Zold ∓ ∂ z total

CONCLUSIONS AND RECOMMENDATIONS

Two laboratory experiments and field experiments along with numerical simulations were conducted to investigate the sediment mixing in the surf zone and the sediment properties along the cross-shore for Hasaki Coast, Japan. The sediment mixing observed from the swash zone to the offshore end of surf zone reveals a dynamic pattern of sediment mixing in the area along the cross-shore direction where the maximum intrusion occurs towards the offshore direction during erosive waves and otherwise. The sediments were moving in direction while mixing in depth and as time goes by, the areas with maximum intrusions get eroded which is an important observation that could help in future research work of sediment transport and ecological, sediment pollution studies. It is recommended to expand the mixing depth relationships observed in past to re-evaluate according to the area of interest since the validation of them is only within the surf zone.

The sediment transport has great influence by the turbulence occurrence during wave breaking. Also there are various wave breaking styles existing in the coast which depends on the wave intensity approaching the coastline. Thus the sediment mixing in the wave breaking region under different wave breaking styles were observed in a flume experiment setup. It was observed that the bottom plane eddies created during wave breaking has a significant influence on sediment mixing. The bottom plain eddies created by different wave breaking styles in the coastal area would initially affect sediment mixing which would further be carried away by the bed shear stress exceedance as mentioned by past researchers under bed load transport. It is recommended by this finding to include in sediment mixing studies in future and also shows the importance of considering eddies formed during wave breaking into sediment flux calculations.

The Hasaki Coastal bathymetry has been drastically changed after the high waves generated in 2006 which has moved offshore coarser particles to the swash area creating a stagnant beach slope near to the coastline. The high wave occurrences during the period has changed the sedimentological properties along the cross-shore direction which has influenced in bed profile evolution. This study reveals that there is a poorly sorted, coarse materials as reached in depth which appears during the winter high wave conditions when the profile is eroded and covered back during summer calm wave conditions by a fine, well-sorted sediment layer. The well compacted sediment layer underneath would limit the profile elevation change in the cross-shore direction that alters the general transport mechanism of sediment transport. The amount of depth in sediment mixing has been also

making a significant relationship with the sediment properties of sorting coefficient and percentile diameters. The coarser and poor the sorting of a sand sample, the mixing was observed to be higher in depth which could also be affected by the wave hydrodynamics which has not been compared in this research. The majority of mixing in the fine, well-sorted sand areas could also be a result of high porosities. The mixing is mostly significant in the wave height transition zone where the height reduces after wave breaking. It is recommended to investigate further into sediment properties and sediment mixing correlations for further clarifications of what was observed in this research that would help in the areas of sediment transport and eco-system studies.

Other than for sediment mixing, the heterogeneous sediment behavior in the coastal area should be included in sediment flux calculation models for better simulation results of research work. A new method was introduced to include different diameters in a volumetric content ratio that would help to calculate sediment transport amounts and bed elevation change for beaches with a varying diameter pattern.

REFERENCES

Abuodha, J.O.Z., 2003. Grain size distribution and composition of modern dune and beach sediments, Malindi Bay coast, Kenya. *Journal of African Earth Sciences*, *36*(1-2), pp.41-54.

Airoldi, L., Fabiano, M. and Cinelli, F., 1996. Sediment deposition and movement over a turf assemblage in a shallow rocky coastal area of the Ligurian Sea. *Marine Ecology Progress Series*, pp.241-251.

Anfuso, G. and Ruiz, N., 2004. Morphodynamics of a mesotidal, exposed, low tide terrace beach (Faro, southern Portugal). *Ciencias Marinas*, *30*(4), pp.575-584.

Anfuso, G., 2005. Sediment-activation depth values for gentle and steep beaches. *Marine Geology*, *220*(1-4), pp.101-112.

Anfuso, G., Benavente, J., Del Río, L., Castiglione, E. and Ventorre, M., 2003. Sand transport and disturbance depth during a single tidal cycle in a dissipative beach: La Barrosa (SW Spain). In *Proceeding of the 3rd IAHR Symposium on River, Coastal and Estuarine Morphodynamics* (Vol. 2, pp. 1176-1186).

Anfuso, G., Gracia, F.J., Andrés, J., Sánchez, F., Del Río, L. and Lopez-Aguayo, F., 2000. Depth of disturbance in mesotidal beaches during a single tidal cycle. *Journal of Coastal Research*, pp.446-457.

Bagnold, R., 1963. An approach of marine sedimentation. In: Hill, M.N. (Ed.), The Sea, vol. 3. Interscience, New York, pp. 507–528.

Bagnold, R.A., 1940. BEACH FORMATION BY WAVES: SOME MODEL EXPERIMENTS IN A WAVE TANK.(INCLUDES PHOTOGRAPHS). *Journal of the Institution of Civil Engineers*, *15*(1), pp.27-52.

Bagnold, R.A., 1966. An approach of sediment transport model from general physics US Geol. *Survey Prof. Paper*.

Bailard, J.A., 1981. An energetics total load sediment transport model for a plane sloping

beach. *Journal of Geophysical Research: Oceans*, *86*(C11), pp.10938-10954.

Bellido, C., Anfuso, G., Plomaritis, T.A. and Buitrago, N.R., 2011. Morphodynamic behaviour, disturbance depth and longshore transport at Camposoto Beach (Cadiz, SW Spain). *Journal of Coastal Research*, (64), p.35.

Bijker, E.W., 1968. Littoral drift as function of waves and current. In *Coastal Engineering 1968* (pp. 415-435).

Blinovskaya, Y.Y., 2012. Topical Coastal Environmental Issues of Japan Sea. *Shimane Journal of North East Asian Research*, *23*, pp.41-46.

Botton, M.L., Loveland, R.E. and Jacobsen, T.R., 1988. Beach erosion and geochemical factors: influence on spawning success of horseshoe crabs (Limulus polyphemus) in Delaware Bay. *Marine Biology*, *99*(3), pp.325-332.

Brian, G. and Peter, B., Depth of Activity, Sediment Flux, and Morphological Change in a Barred Nearshore Environment.

Brook, A.M. and Lemckert, C., 2011. *A new technique for measuring Depth of Disturbance in the Swash Zone*. Griffith University.

Buscombe, D. and Masselink, G., 2006. Concepts in gravel beach dynamics. *Earth-Science Reviews*, *79*(1-2), pp.33-52.

Camenen, B. and Larroudé, P., 2000. Numerical comparison of sediment transport formulae. *Marine Sandwave Dynamics*.

Camenen, B. and Larroudé, P., 2003. Comparison of sediment transport formulae for the coastal environment. *Coastal Engineering*, *48*(2), pp.111-132.

Camenen, B. and Larroudé, P., 2003. Comparison of sediment transport formulae for the coastal environment. *Coastal Engineering*, *48*(2), pp.111-132.

Chau, K.W. and Jiang, Y.W., 2001. 3D numerical model for Pearl River estuary. *Journal of Hydraulic Engineering*, *127*(1), pp.72-82.

Ciavola, P., Taborda, R. and Ferreira, Ó., 1997. Field observations of sand-mixing depths on steep beaches. *Marine Geology*, *141*(1-4), pp.147-156.

Cooper, N.J. and Pethick, J.S., 2005. Sediment budget approach to addressing coastal erosion problems in St. Ouen's Bay, Jersey, Channel Islands. *Journal of Coastal Research*, pp.112-122.

De Falco, G., Molinaroli, E., Baroli, M. and Bellaciccob, S., 2003. Grain size and compositional trends of sediments from Posidonia oceanica meadows to beach shore, Sardinia, western Mediterranean. *Estuarine, Coastal and Shelf Science*, *58*(2), pp.299-309.

Dean, R.G. and Dalrymple, R.A., 2004. *Coastal processes with engineering applications*. Cambridge University Press.

Dibajnia, M. and Watanabe, A., 1993. Sheet flow under nonlinear waves and currents. In *Coastal Engineering 1992*(pp. 2015-2028).

Douglass, S.L., 1994. Beach erosion and deposition on Dauphin Island, Alabama, USA. *Journal of Coastal Research*, pp.306-328.

DuBoys, P., 1879. Le Rhône et les rivières à lit affouillable. In *Annales des ponts et chaussees* (Vol. 18, No. 5, pp. 141-195). [in French]

Edwards, A.C., 2001. Grain size and sorting in modern beach sands. *Journal of Coastal Research*, pp.38-52.

Edwards, A.C., 2001. Grain size and sorting in modern beach sands. *Journal of Coastal Research*, pp.38-52.

Einstein, H.A., 1950. *The bed-load function for sediment transportation in open channel flows* (Vol. 1026). Washington DC: US Department of Agriculture.

Einstein, H.A., 1971. A basic description of sediment transport on beaches. *Waves on*

beaches and resulting sediment transport, pp.53-93.

Feagin, R.A., Sherman, D.J. and Grant, W.E., 2005. Coastal erosion, global sea‐level rise, and the loss of sand dune plant habitats. *Frontiers in Ecology and the Environment*, *3*(7), pp.359-364.

Ferreira, Ó., Bairros, M., Pereira, H., Ciavola, P. and Dias, J.A., 1998. Mixing depth levels and distribution on steep foreshores. *Journal of Coastal Research*, pp.292-296.

Ferreira, O., Ciavola, P., Taborda, R., Bairros, M. and Dias, J.A., 2000. Sediment mixing depth determination for steep and gentle foreshores. *Journal of Coastal Research*, pp.830-839.

Folk, R.L., 1954. The distinction between grain size and mineral composition in sedimentary-rock nomenclature. *The Journal of Geology*, *62*(4), pp.344-359.

Friedman, G.M., 1962. On sorting, sorting coefficients, and the lognormality of the grain-size distribution of sandstones. *The Journal of Geology*, *70*(6), pp.737-753.

Frihy, O.E. and Komar, P.D., 1993. Long-term shoreline changes and the concentration of heavy minerals in beach sands of the Nile Delta, Egypt. *Marine Geology*, *115*(3-4), pp.253-261.

Fucella, J.E. and Dolan, R., 1996. Magnitude of subaerial beach disturbance during northeast storms. *Journal of Coastal Research*, pp.420-429.

Füchtbauer, H., 1959. Zur Nomenklatur der Sedimentgesteine. *Erdöl und Kohle*, *12*(8), pp.605-613.

Gallagher, E., Wadman, H., McNinch, J., Reniers, A. and Koktas, M., 2016. A conceptual model for spatial grain size variability on the surface of and within beaches. *Journal of Marine Science and Engineering*, *4*(2), p.38.

Gaughan, M.K., 1978. Depth of disturbance of sand in surf zones. In *Coastal Engineering 1978* (pp. 1513-1530).

Greenwood, B. and Hale, P.B., 1980. Depth of activity, sediment flux, and morphological change in a barred nearshore environment.
Holland, K.T. and Elmore, P.A., 2008. A review of heterogeneous sediments in coastal environments. *Earth-Science Reviews*, *89*(3-4), pp.116-134.

Inman, D.L. and Chamberlain, T.K., 1955. Particle-size distribution in nearshore sediments.

Isobe, M., 1998, July. Toward integrated coastal zone management in Japan. In *ESENA Workshop: Energy-Related Marine Issues in the Sea of Japan* (pp. 11-12).

Jackson, D.W.T. and Malvarez, G., 2002. A new, highresolution 'depth of disturbance'instrument (SAM) for use in the surf zone. *Journal of Coastal Research*, *36*, pp.406-413.

Jiang, C., Wu, Z., Chen, J., Deng, B. and Long, Y., 2015. Sorting and sedimentology character of sandy beach under wave action. *Procedia Engineering*, *116*, pp.771-777.

Kakinoki, T., Tsujimoto, G. and Uno, K., 2011. Grain-Size Sorting In The Swash Zone On Unequilibrium Beaches At The Timescale Of Individual Waves. *Coastal Engineering Proceedings*, *1*(32), p.27.

Katoh, K. and Tanaka, N., 1986. Local movements of sand in the surf zone. *Coastal Engineering Proceedings*, *1*(20).

Komar, P., 1998. Beach Processes and Sedimentation, 2nd edn., Prentice-Hall Press, New Jersey, 544pp.

Kraus, N.C., Isobe, M., Igarashi, H., Sasaki, T.O. and Horikawa, K., 1982. Field experiments on longshore sand transport in the surf zone. In *Coastal Engineering 1982* (pp. 969-988).

Krumbein, W.C. and Aberdeen, E., 1937. The sediments of Barataria bay. *Journal of Sedimentary Research*, *7*(1).

Kumada, T., Uda, T. and Serizawa, M., 2006. Model for predicting composition changes

of grain size of bed materials. *Proc. 30th ICCE, ASCE*.

Kuriyama, Y., 2002. Medium‐term bar behavior and associated sediment transport at Hasaki, Japan. *Journal of Geophysical Research: Oceans*, *107*(C9).

Leatherman, S.P., 2001. Social and economic costs of sea level rise. In *International Geophysics* (Vol. 75, pp. 181-223). Academic Press.

Lin, P. and Liu, P.L.F., 1998. A numerical study of breaking waves in the surf zone. *Journal of fluid mechanics*, *359*, pp.239-264.

McCall, R.T., De Vries, J.V.T., Plant, N.G., Van Dongeren, A.R., Roelvink, J.A., Thompson, D.M. and Reniers, A.J.H.M., 2010. Two-dimensional time dependent hurricane overwash and erosion modeling at Santa Rosa Island. *Coastal Engineering*, *57*(7), pp.668-683.

McLean, R.F. and Kirk, R.M., 1969. Relationships between grain size, size-sorting, and foreshore slope on mixed sand-shingle beaches. *New Zealand Journal of Geology and Geophysics*, *12*(1), pp.138-155.

Mellor, G.L., 1998. A Three Dimensional, Primitive Equation, Numerical Ocean Model (Users Guide). *Available on the Princeton Ocean Model web site:< http://www. aos. princeton. edu/WWWPUBLIC/htdocs. pom*.

Moutzouris, C.I., 1989. Longshore Sediment Transport Rate vs. Cross–Shore Distribution of Sediment Grain Sizes. In *Coastal Engineering 1988* (pp. 1959-1973).

Niroshinie, M.A.C., 2014. Investigation of fluid motion and sediment concentration under breaking waves considering the change in bed topography, PhD Dissertation Yokohama National University, Japan.

Nordstrom, K.F. and Jackson, N.L., 1990. Migration of swash zone, step and microtopographic features during tidal cycles on an estuarine beach, Delaware Bay, New Jersey, USA. *Marine Geology*, *92*(1-2), pp.147-154.

Oyedotun, T.D.T., 2016. Sediment Characterisation in an Estuary-Beach System. *J Coast*

Zone Manag, *19*(433), p.2.

Pender, D. and Karunarathna, H., 2013. A statistical-process based approach for modelling beach profile variability. *Coastal Engineering*, *81*, pp.19-29.

Quick, M.C., 1991. Onshore-offshore sediment transport on beaches. *Coastal Engineering*, *15*(4), pp.313-332.

Ribberink, J.S., 1998. Bed-load transport for steady flows and unsteady oscillatory flows. *Coastal Engineering*, *34*(1-2), pp.59-82.

Riesenkamp, M.J., 2011. Probabilistic modelling of extreme beach erosion using XBeach.

Rijn, L.C.V., 1984. Sediment transport, part II: suspended load transport. *Journal of hydraulic engineering*, *110*(11), pp.1613-1641.

Roelvink, D., Reniers, A., Van Dongeren, A.P., de Vries, J.V.T., McCall, R. and Lescinski, J., 2009. Modelling storm impacts on beaches, dunes and barrier islands. *Coastal engineering*, *56*(11-12), pp.1133-1152.

Saini, S., Jackson, N.L. and Nordstrom, K.F., 2009. Depth of activation on a mixed sediment beach. *Coastal Engineering*, *56*(7), pp.788-791.

Schneiderhöhn, P., 1953. Untersuchungen zur Siebanalyse von Sanden und zur Darstellung ihrer Ergebnisse. *N. Jb. Miner., Abh*, *85*, pp.141-202.

Serizawa, M., Uda, T., San-nami, T., Furuike, K., Ishikawa, T. and Kumada, T., 2007. Model for predicting beach changes on coast with sand of mixed grain size based on Bagnold's concept. In *Coastal Sediments' 07* (pp. 314-326).

Short, A.D., 2012. Coastal processes and beaches. *Nature education knowledge*, *3*(10), p.15.

Smagorinsky, J., 1963. General circulation experiments with the primitive equations: I. The basic experiment. *Monthly weather review*, *91*(3), pp.99-164.

Soulsby, R., 1997. *Dynamics of marine sands: a manual for practical applications*. Thomas Telford.
Stauble, D.K., 2005. A review of the role of grain size in beach nourishment projects.

Sunamura, T. and Kraus, N.C., 1985. Prediction of average mixing depth of sediment in the surf zone. *Marine Geology*, *62*(1-2), pp.1-12.

Sunamura, T., 1984. Quantitative predictions of beach-face slopes. *Geological Society of America Bulletin*, *95*(2), pp.242-245.

Suzuki, T. (2004), Investigation of fluid motion and sediment suspension due to wave breaking and a three dimensional numerical model, PhD Dissertation Yokohama National University, Japan (in Japanese).

Suzuki, T. and Kuriyama, Y., 2007. Medium-term shoreline changes at Hasaki, Japan. In *Coastal Engineering 2006: (In 5 Volumes)* (pp. 3241-3253).

Suzuki, T., Inami, Y., Banno, M. and Kuriyama, Y., 2017. Observation of sediment particle movements during a storm. *Coastal Dynamics 2017*.

Thielicke, W. and Stamhuis, E., 2014. PIVlab–towards user-friendly, affordable and accurate digital particle image velocimetry in MATLAB. *Journal of Open Research Software*, *2*(1).

Thornton, E.B. and Guza, R.T., 1986. Surf zone longshore currents and random waves: Field data and models. *Journal of Physical Oceanography*, *16*(7), pp.1165-1178.

Trask, P.D., Hammar, H.E. and Wu, Z., 1932. *Origin and environment of source sediments of petroleum*. Gulf Publishing Company.

UDA, T., KUMADA, T. and SERIZAWA, M., 2005. Predictive model of change in longitudinal profile in beach nourishment using sand of mixed grain size. In *Coastal Engineering 2004: (In 4 Volumes)* (pp. 3378-3390).

van Rijn, L.C., 2007. Unified view of sediment transport by currents and waves. II: Suspended transport. *Journal of Hydraulic Engineering*, *133*(6), pp.668-689.

Vanoni, V.A., 1975. Sedimentation engineering, ASCE manuals and reports on engineering practice—No. 54. *American Society of Civil Engineers, New York, NY*.

Vousdoukas, M.I., Almeida, L.P. and Ferreira, Ó., 2011. Modelling storm-induced beach morphological change in a meso-tidal, reflective beach using XBeach. *Journal of coastal research*, (64), p.1916.

Vousdoukas, M.I., Ferreira, Ó., Almeida, L.P. and Pacheco, A., 2012. Toward reliable storm-hazard forecasts: XBeach calibration and its potential application in an operational early-warning system. *Ocean Dynamics*, *62*(7), pp.1001-1015.

Warner, J.C., Sherwood, C.R., Signell, R.P., Harris, C.K. and Arango, H.G., 2008. Development of a three-dimensional, regional, coupled wave, current, and sediment-transport model. *Computers & Geosciences*, *34*(10), pp.1284-1306.

Wijayaratna, T. M. N., 2000. Numerical simulation of wave breaking on slopes and its applications, PhD Dissertation Yokohama National University, Japan.

Williams, A.T., 1971. An analysis of some factors involved in the depth of disturbance of beach sand by waves. *Marine Geology*, *11*(3), pp.145-158.

Wright, L.D., 1980. Beach cut in relation to surf zone morphodynamics. In *Coastal Engineering 1980* (pp. 978-996).

Yanagishima, S., 2016. Characteristic of grain size change at the Hasaki coast : Technical Note 1317 Port and Airport Research Institute, Japan. URL: http://www.pari.go.jp/search-pdf/No1317.pdf (accessed 11Sept2017).

APPENDIX A

The following shows some of the important trials of XBeach calibration process and the BSS values for each trial case.

Trials	Variable Parameter	Varied Value	Other Parameters	BSS Value	
				Erosion	Deposition
default	none	dryslp =1 wetslp = 0.3 wci = 0 facua = 0.1		-0.263	-0.674
1	wci	0	dryslp = 1 wetslp = 0.3	-0.263	-0.674
2		1	facua = 0.1	-0.163	-0.450
3	dryslp	0.1	wci = 1	0.759	-0.342
4		0.2	wetslp = 0.3	0.459	-0.450
5		0.5	facua = 0.1	-0.163	-0.450
6		0.8		-0.163	-0.450
7		1.5		-0.163	-0.450
8		2		-0.163	-0.450
9	wetslp	0.1	wci = 1	0.735	-0.355
10		0.2	dryslp = 0.1	0.759	-0.342
11		0.5	facua = 0.1	0.759	-0.342
12		0.8		0.759	-0.342
13		1		0.759	-0.342
14	facua	0	wci = 1	0.724	-0.382
15		0.2	dryslp = 0.1	0.788	-0.311
16		0.5	wetslp = 0.2	**0.842**	-0.223
17		0.8		0.824	-0.140
18		1		0.807	-0.082

The most reasonable calibration BSS values have been highlighted in red. Almost all the calibration trials of Accretive wave conditions stands equal to or less than zero in BSS value.

APPENDIX B

The following figures show the wave gauge records along the flume test experiment under four wave cases.

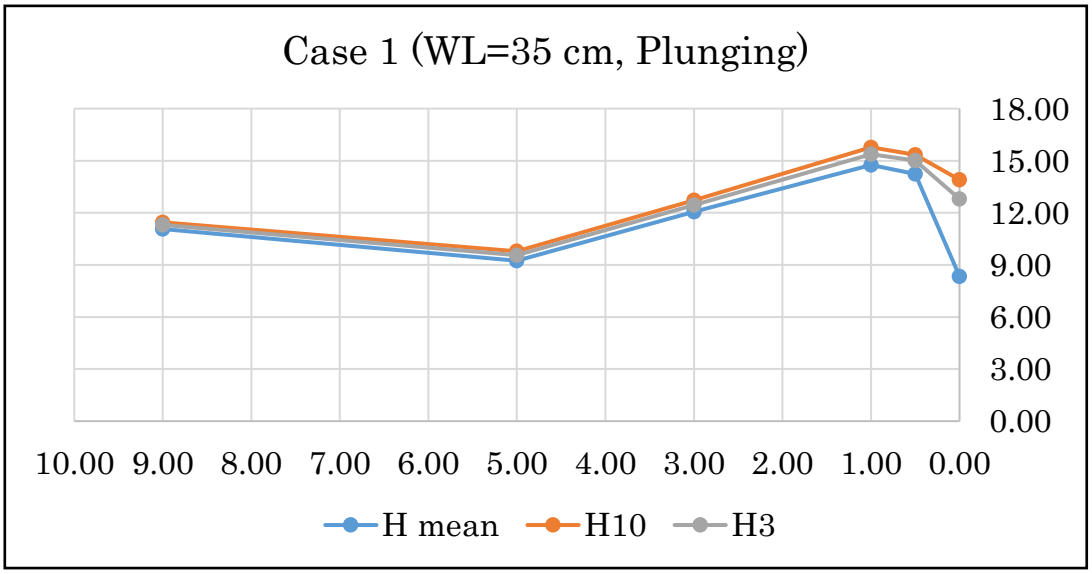

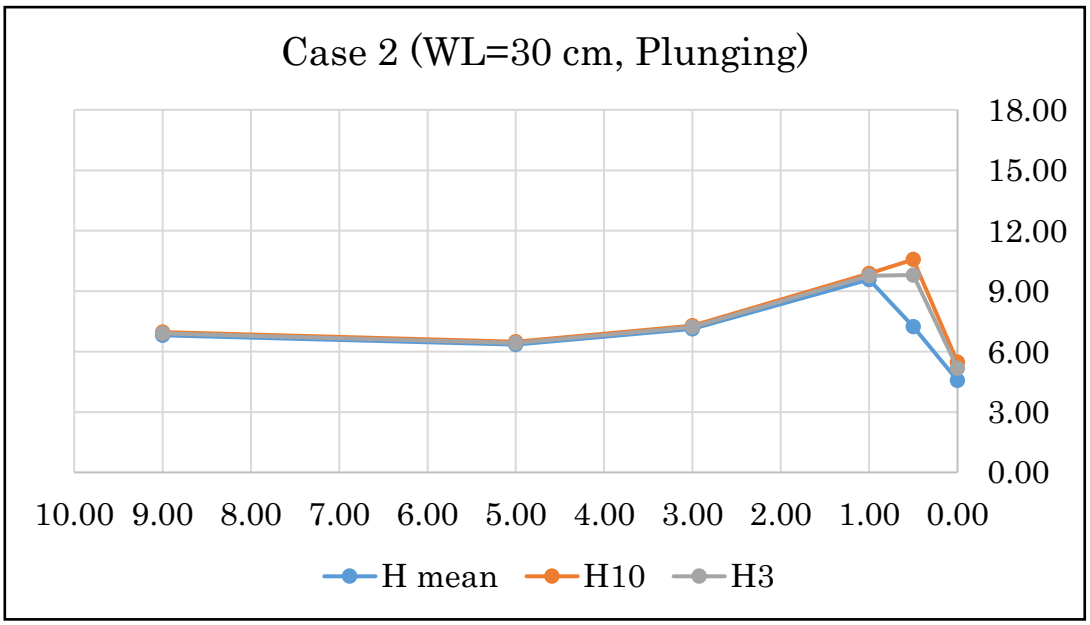

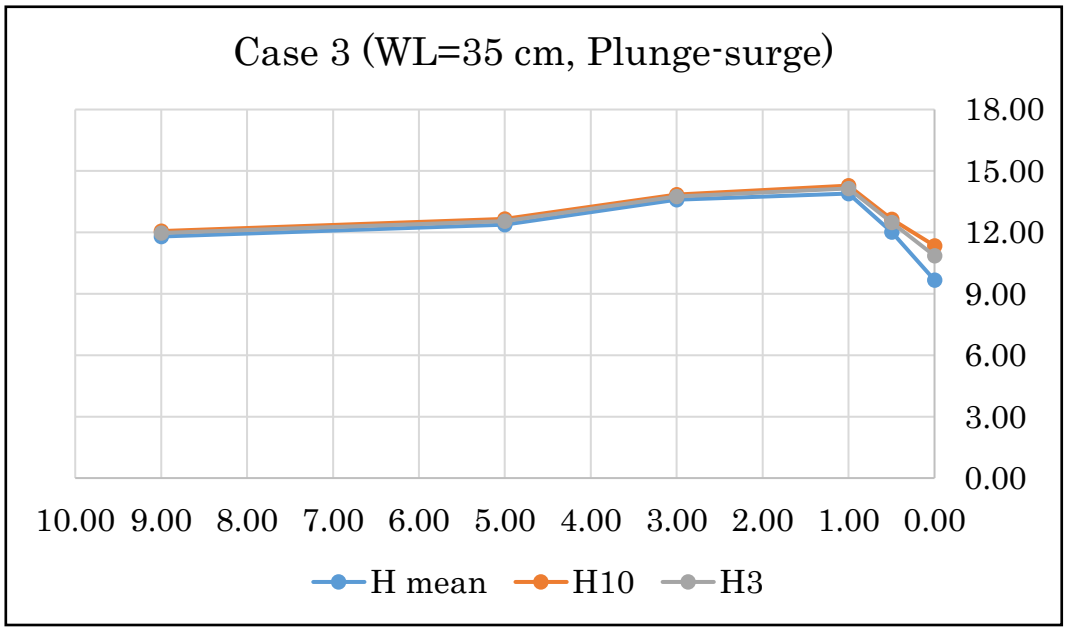
Case 3 (WL=35 cm, Plunge-surge)
18.00
15.00
12.00
9.00
6.00
3.00
0.00
10.00 9.00 8.00 7.00 6.00 5.00 4.00 3.00 2.00 1.00 0.00
H mean
H10
H3

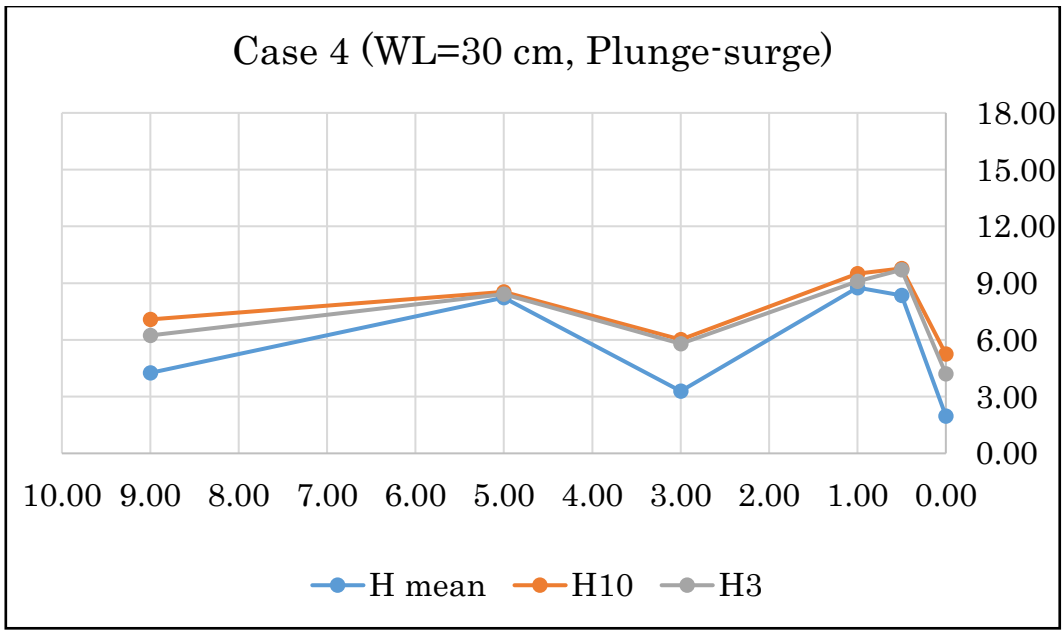
Case 4 (WL=30 cm, Plunge-surge)
18.00
15.00
12.00
9.00
6.00
3.00
0.00
10.00 9.00 8.00 7.00 6.00 5.00 4.00 3.00 2.00 1.00 0.00
H mean
H10
H3

APPENDIX C

The following figures are the comparisons of wave heights recorded and wave height simulated by LES for each wave cases during the experiments. The wave gauge location in the flume location could be given as WG0 – offshore, WG5,6,7,8,9 at x = 400, 430, 450, 470, 500 accordingly.

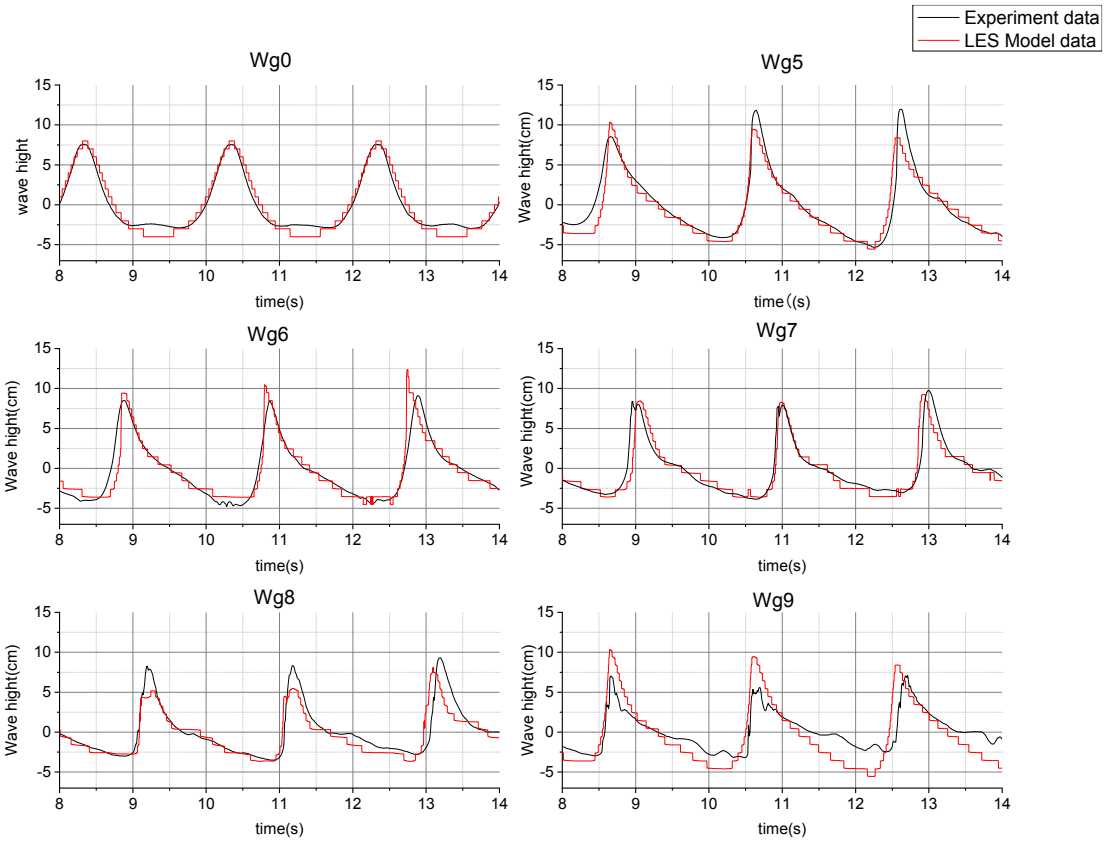

Fig C-1 Case 1

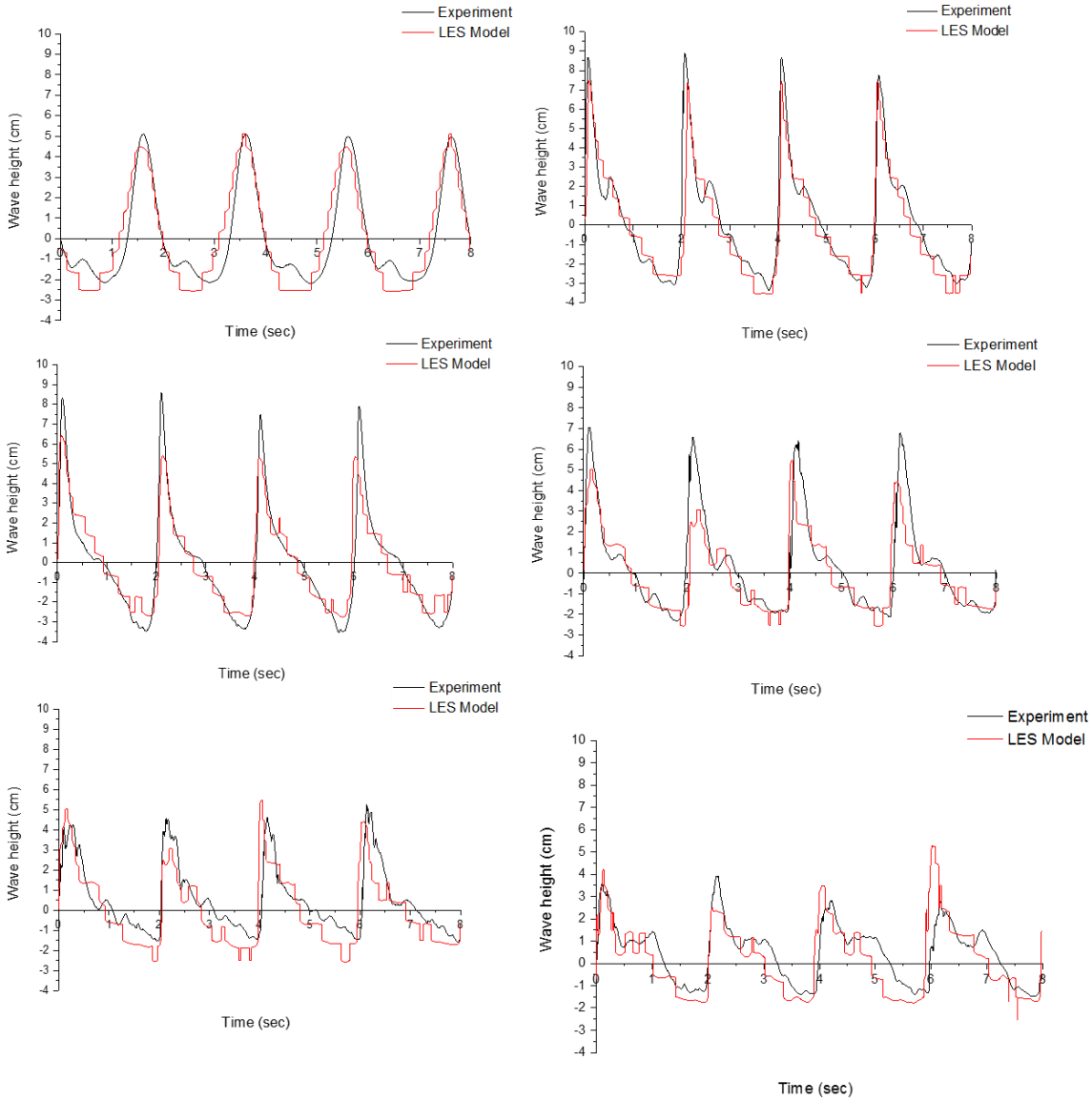

Fig C-2 Case 2

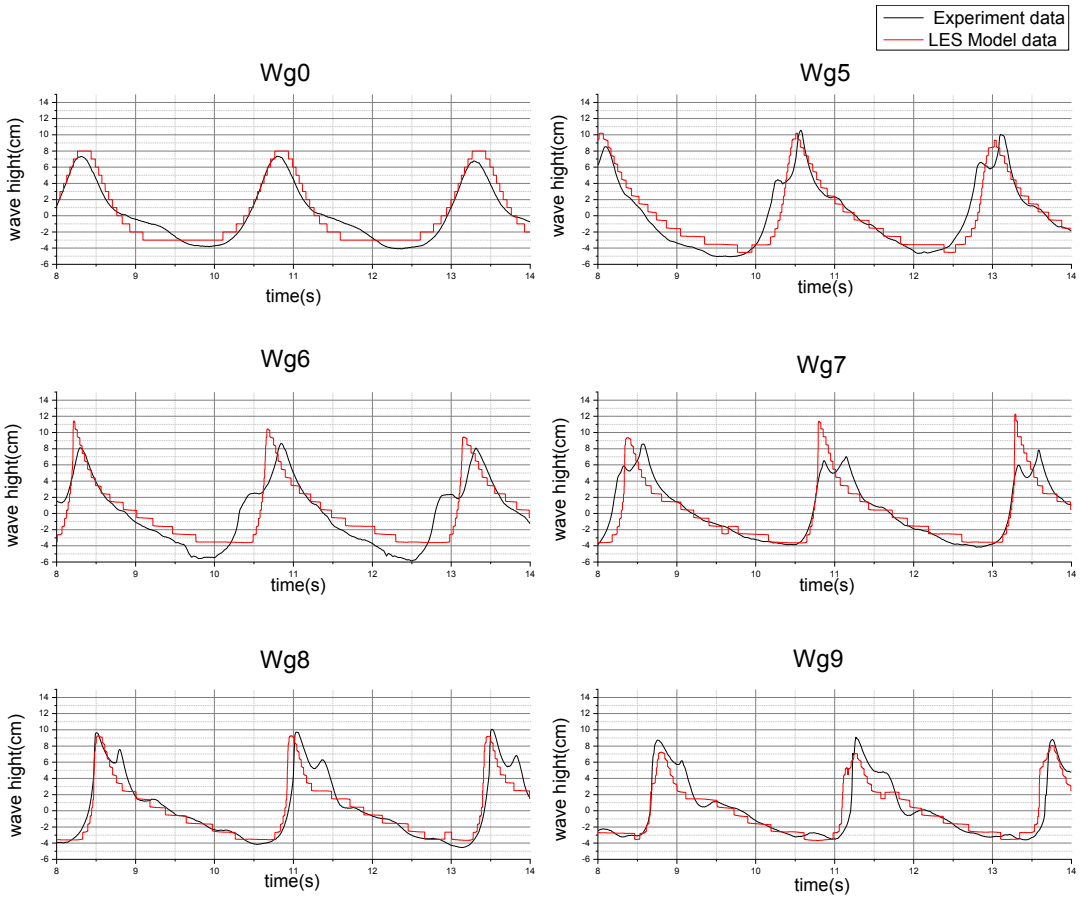
Experiment data
LES Model data
Wg0
Wg5
Wg6
Wg7
Wg8
Wg9
wave hight(cm)
time(s)

Fig C-3 Case 3

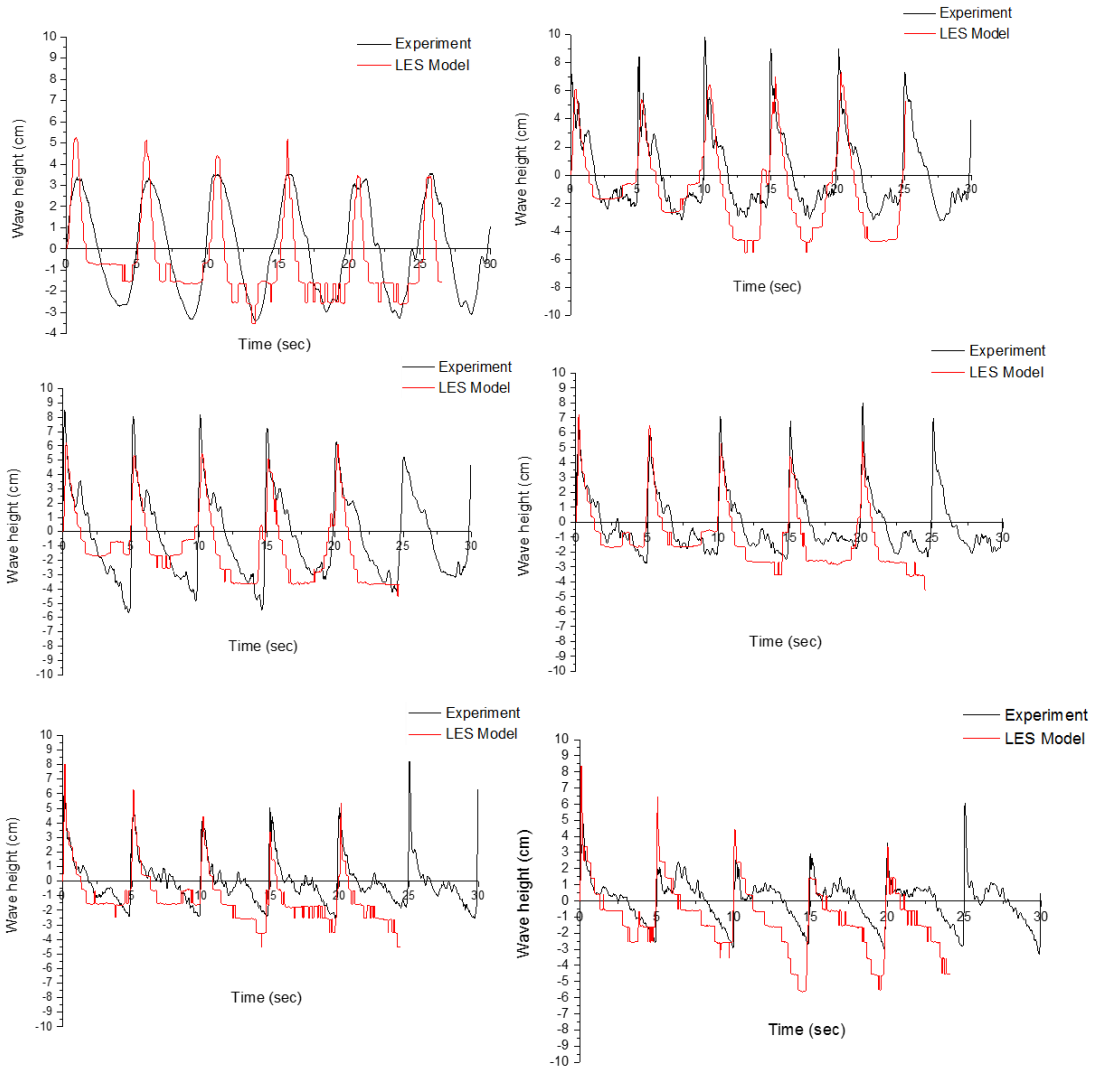

Fig C-4 Case 4

APPENDIX D

The following figures in this section includes detailed counts of fluorescent tracer amounts with respect to the absolute depths of HORS. The experiment results of year 2014, 2015 and 2016 are given.

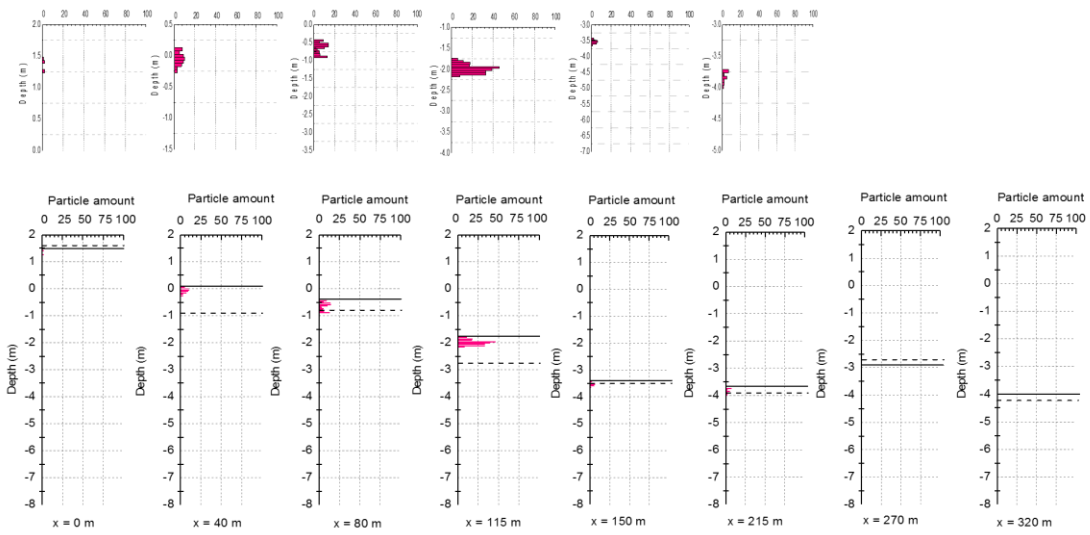

Fig D-1 Experiment results for 2014 pink tracer

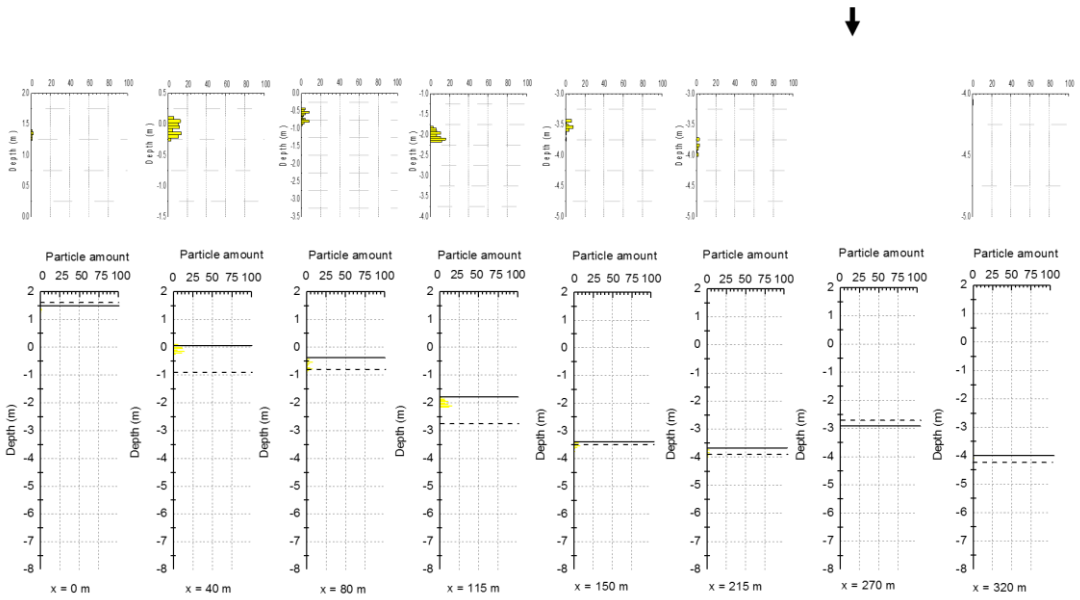

Fig D-2 Experiment results for 2014 yellow tracer

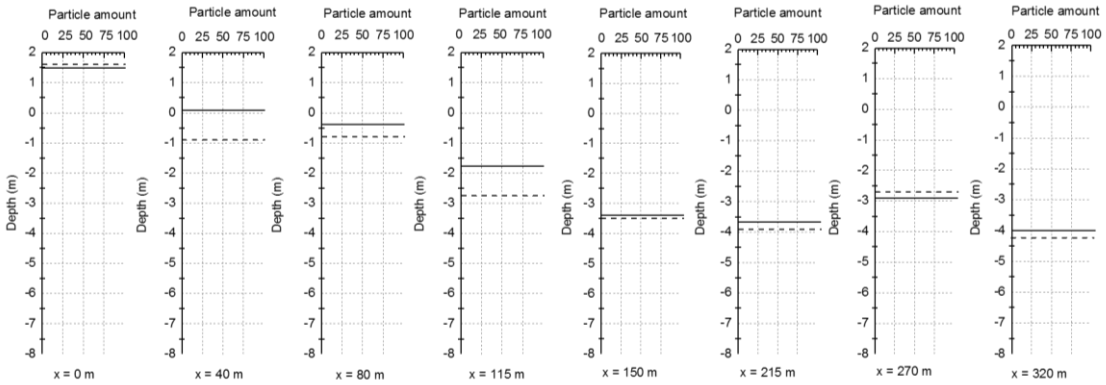

Fig D-3 Experiment results for 2014 blue tracer

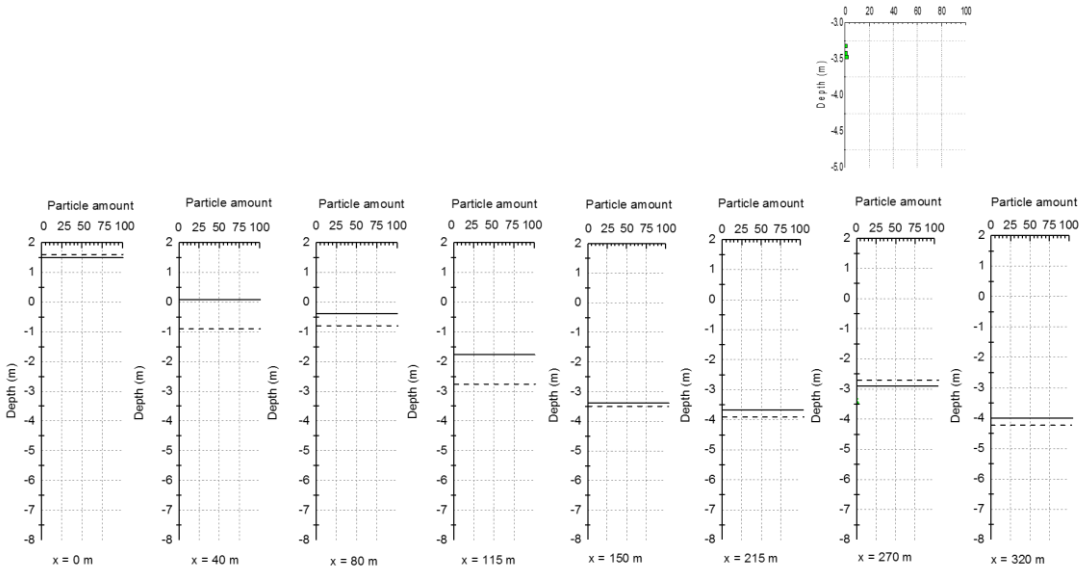

Fig D-4 Experiment results for 2014 green tracer

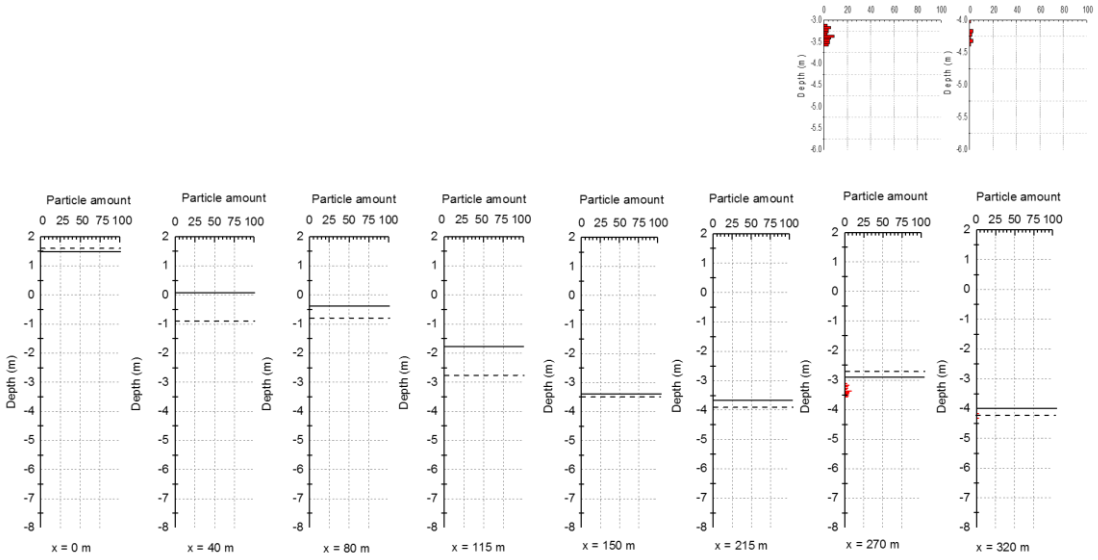

Fig D-5 Experiment results for 2014 red tracer

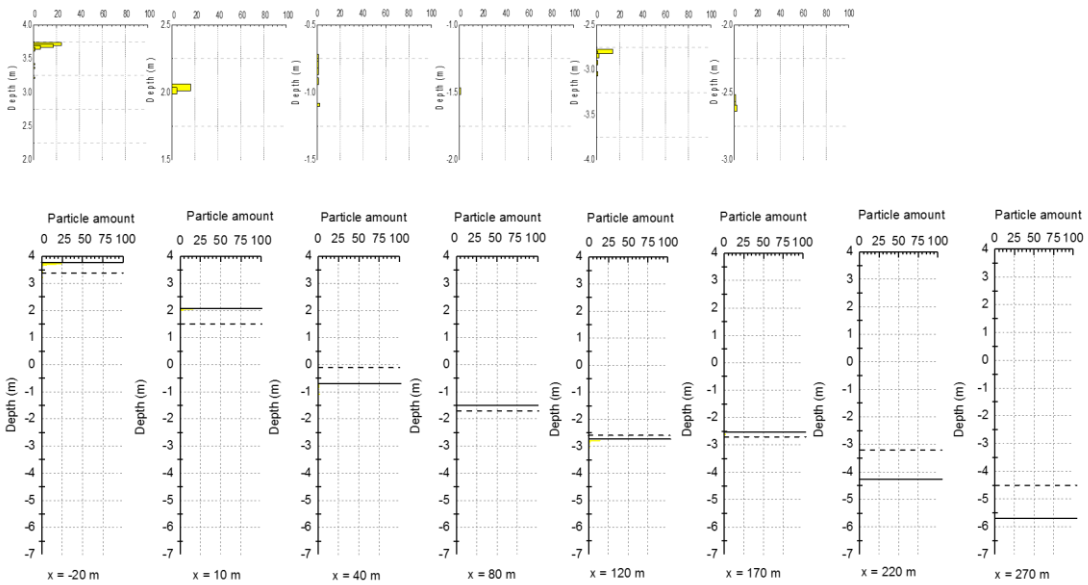

Fig D-6 Experiment results for 2015 yellow tracer

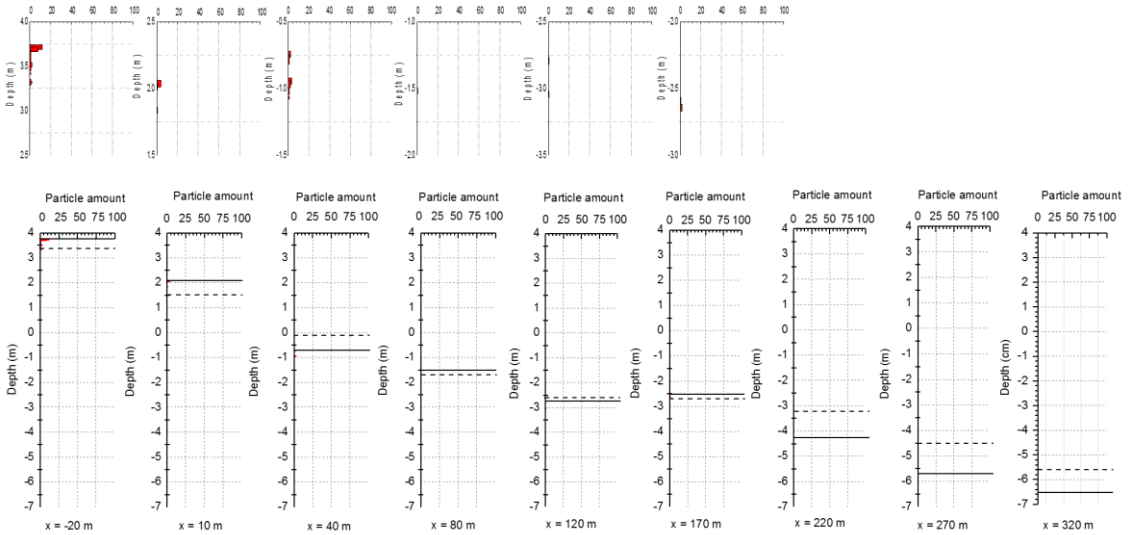

Fig D-7 Experiment results for 2015 red tracer

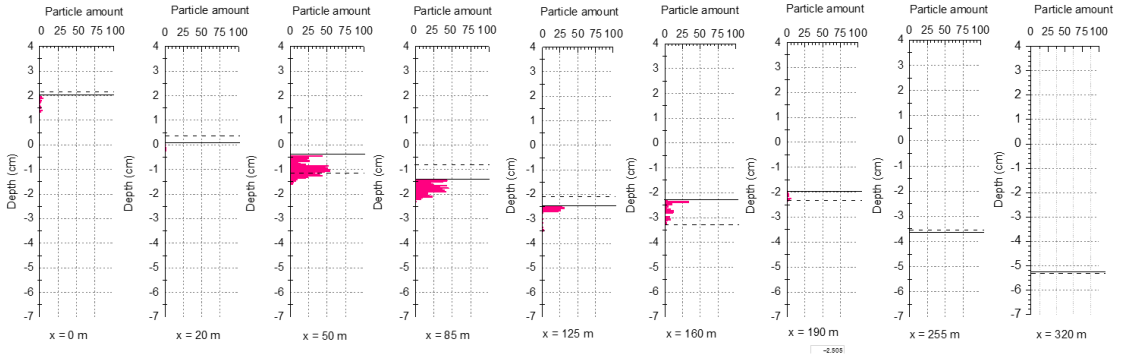

Fig D-8 Experiment results for 2016-1 pink tracer

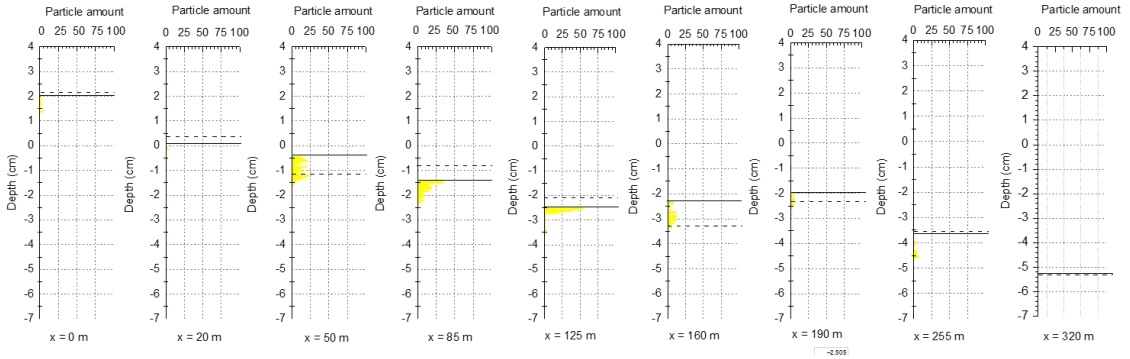

Fig D-9 Experiment results for 2016-1 yellow tracer

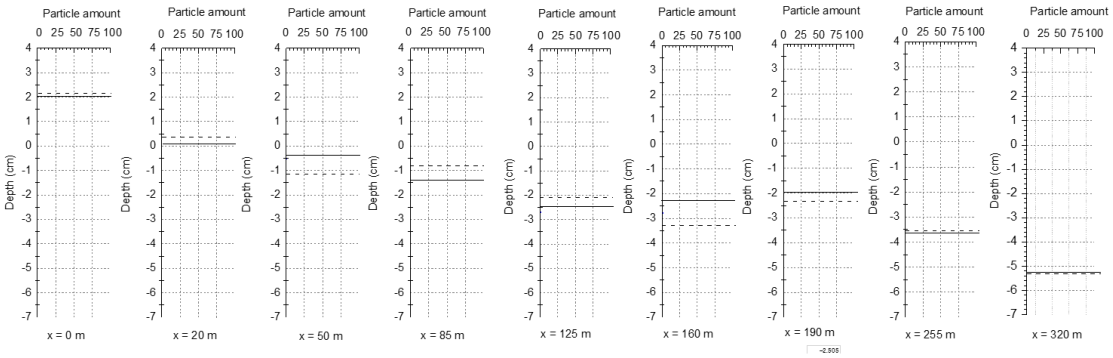

Fig D-10 Experiment results for 2016-1 blue tracer

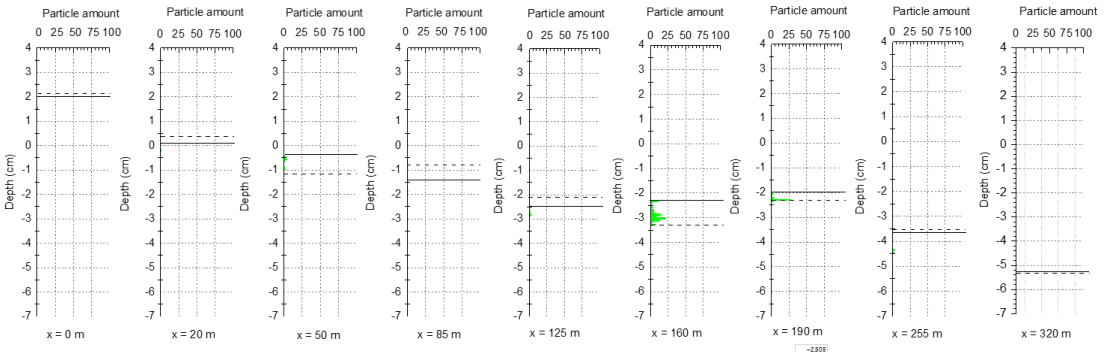

Fig D-11 Experiment results for 2016-1 green tracer

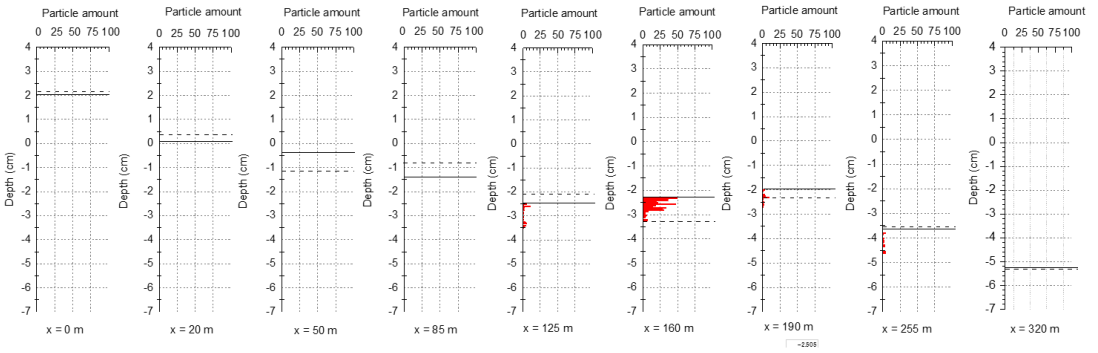

Fig D-12 Experiment results for 2016-1 red tracer

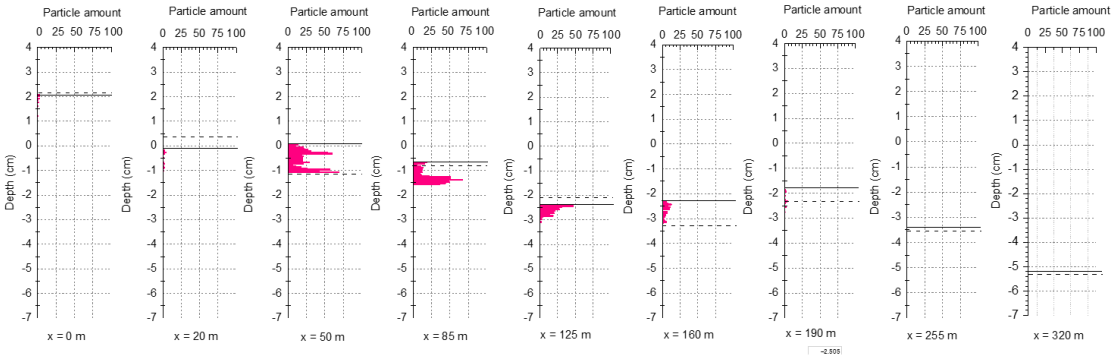

Fig D-13 Experiment results for 2016-2 pink tracer

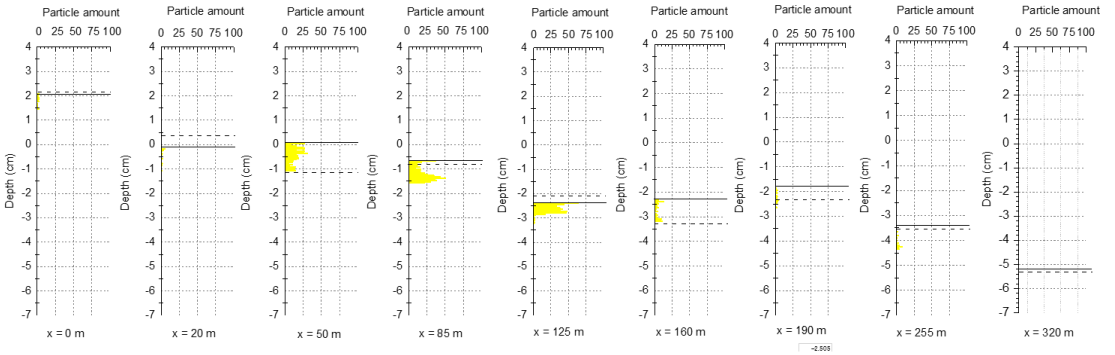

Fig D-14 Experiment results for 2016-2 yellow tracer

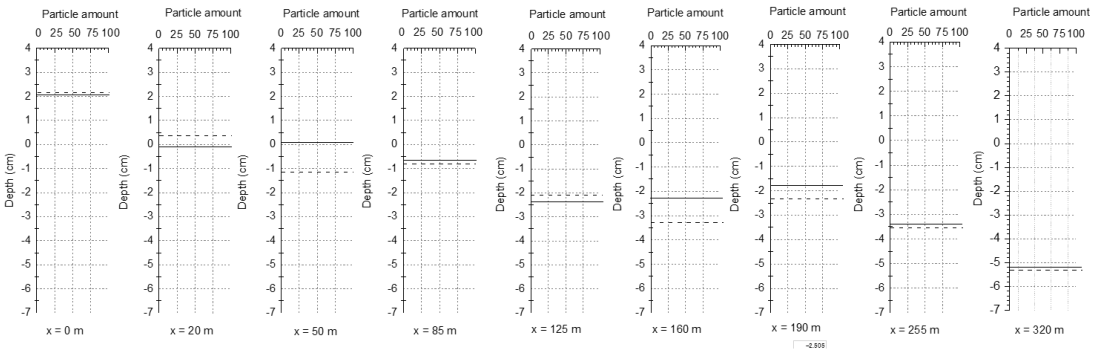

Fig D-15 Experiment results for 2016-2 blue tracer

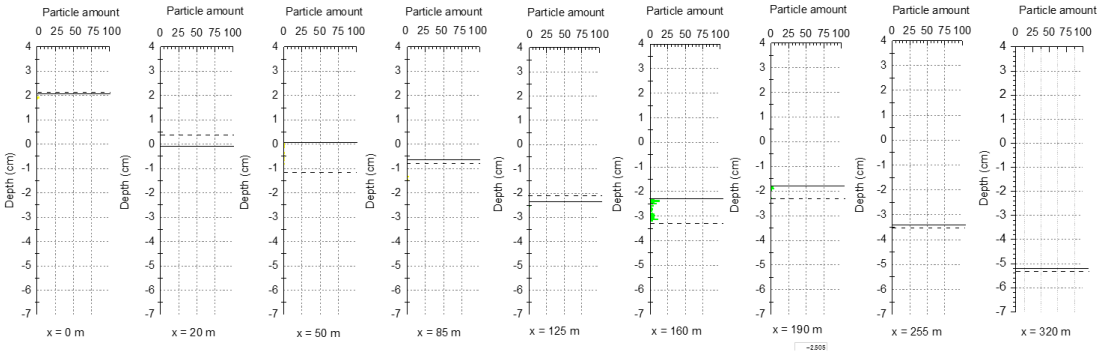

Fig D-16 Experiment results for 2016-2 green tracer

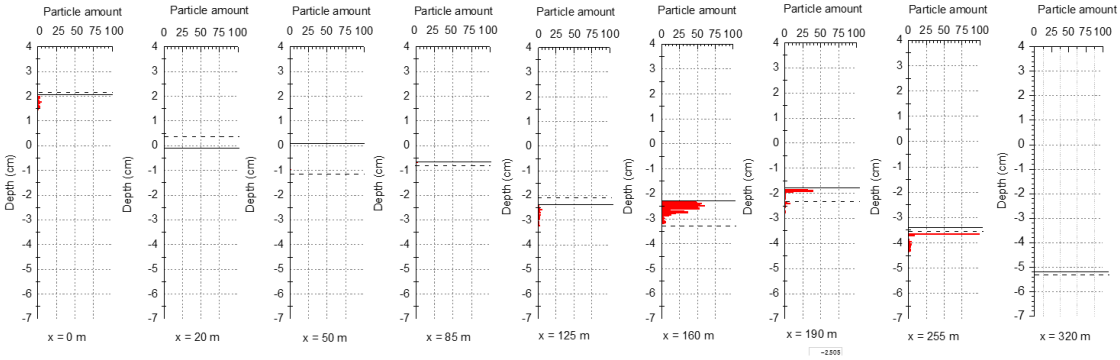

Fig D-17 Experiment results for 2016-2 red tracer

APPENDIX E

In this section, all the waves transformed in 2014, 2015 and 2016 Hasaki coast nearshore area comparison to the wave gauge records are given. The figures were created to calibrate wave transformation parameters.

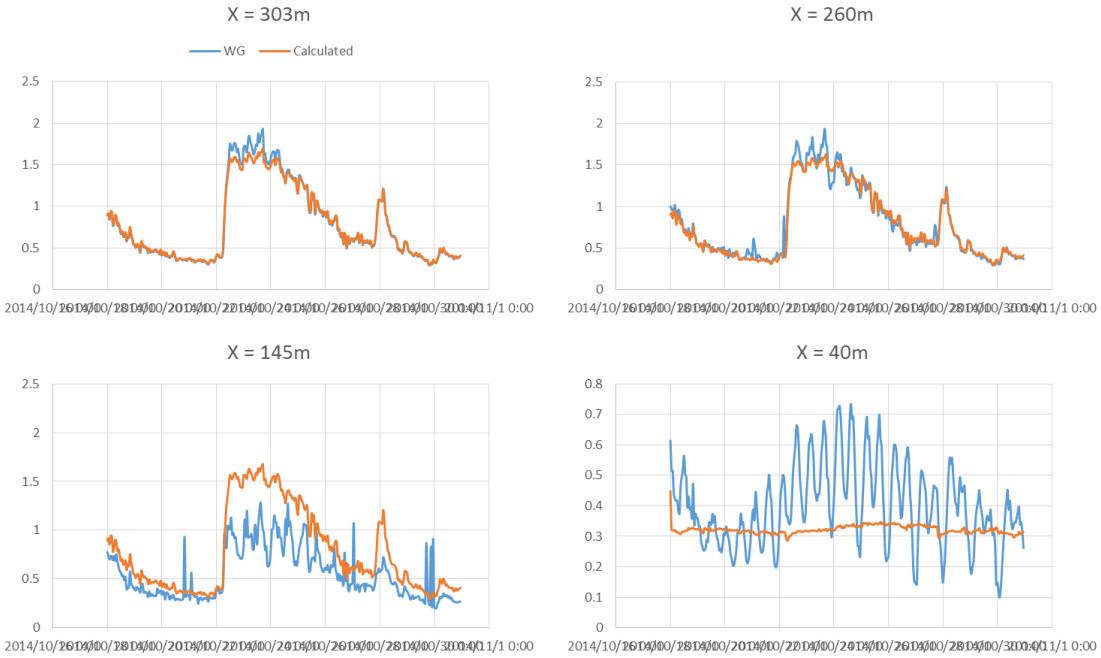

Fig E-1 Wave gauge and wave transformed Hrms comparison for the experiment year 2014 from Oct 19-30

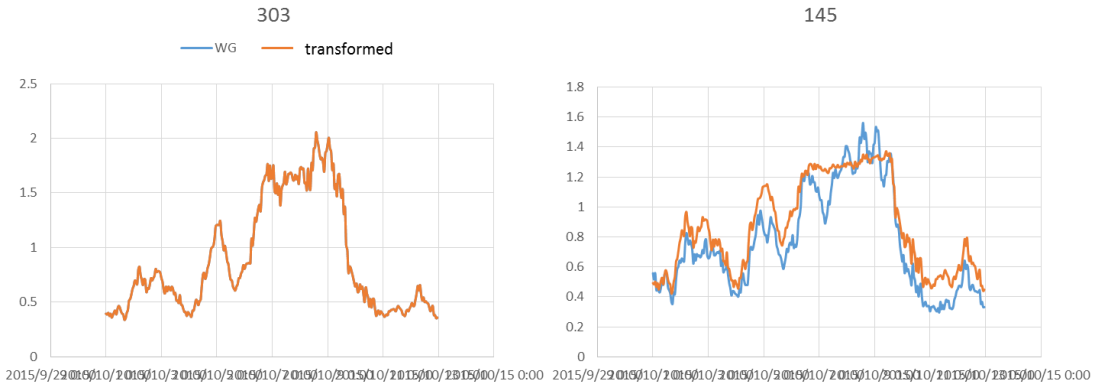

Fig E-2 Wave gauge and wave transformed Hrms comparison for the experiment year 2015 from Oct 1-12

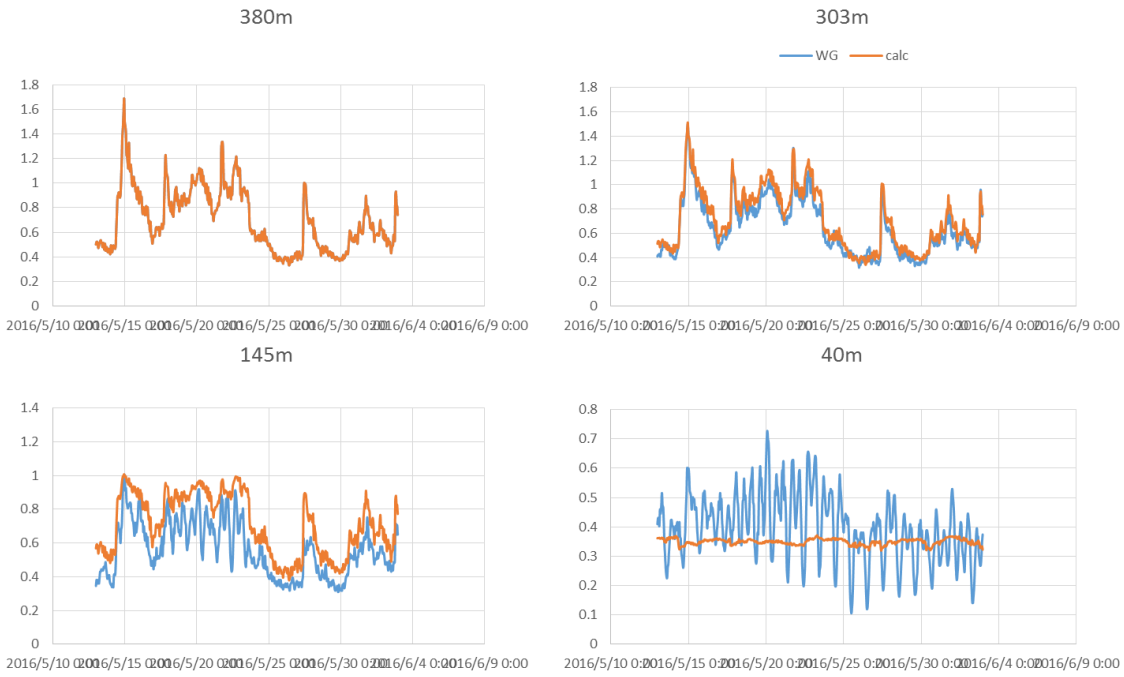

Fig E-3 Wave gauge and wave transformed Hrms comparison for the experiment year 2016 from May 13- Jun 2